



University of Twente
The Netherlands

Cesium-Telluride and Magnesium for high quality photocathodes

Preparation and diagnostics

Master thesis

R.A. Loch

June 2005

Cesium-Telluride and Magnesium for high quality photocathodes

Preparation and diagnostics

R.A. Loch

Enschede, June 2005

Laser Physics and non-linear Optics
Faculty of Science and Technology
University of Twente

Graduation committee:

Prof. Dr. K.J. Boller

Dr. J.W.J. Verschuur

Dr. Ir. H. Wormeester

Summary

Photocathodes are the key devices for generation of high quality electron bunches in various applications, for example: electron accelerators for free electron lasers and electron-positron colliders; or laser wakefield accelerators. Each application sets its own requirements on various particular properties of the used photocathodes.

The properties and suitability of two materials, namely Cesium-Telluride (Cs-Te) and Magnesium, as a high quality photocathode are described in this report for the purpose of the mentioned applications. A detailed survey is given on the work on Cs-Te photocathodes. We conclude that Cs-Te, if properly prepared, is the most appropriate photocathode for use in standard (RF driven) electrons accelerators. The performance of this photocathode largely depends on the preparation process. When the conditions are such that the preparation time is short, the resulting photocathode has a high initial QE but a short lifetime. A long preparation time results in improved photocathodes, having longer lifetimes (in the order of months) and also higher damage thresholds. Initial QE's are lower though still acceptable, above 10%. Combining our own experience with the experiences from predecessors in our group and the detailed survey, made it possible to explain for the first time the difference in performance at altered preparation conditions by the formation of dissimilar Cs-Te stoichiometry. XPS measurements are promising to get a better understanding on the preparation. However, not enough data on the various structures is available yet. A diagnostic setup based on single wavelength ellipsometry is for the moment the best in-situ diagnostic method to control the preparation of Cs-Te photocathodes. The proposed cathode formation process has to be confirmed with this diagnostic tool.

For the second application envisioned, photocathodes for laser wakefield accelerators, we conclude that magnesium is the best photocathode, because of its short time response and a relatively high QE. A preparation chamber is designed to perform test measurements on preparation and performances of this photocathode.

Table of contents

Preface.....	4
1. Introduction.....	5
1.1. Aim of research.....	6
2. Photoemission and photocathodes.....	7
2.1. Photoemission in photocathodes.....	7
2.2. Overview of photocathodes	9
2.2.1. <i>Metallic photocathodes</i>	9
2.2.2. <i>PEA semiconductor photocathodes</i>	10
2.2.3. <i>NEA semiconductor photocathodes</i>	12
2.2.4. <i>Miscellaneous photocathodes</i>	12
2.3. Conclusions.....	13
3. Cs₂Te photocathodes.....	14
3.1. Spectral response	14
3.2. Composition.....	16
3.3. Parameters that influence the performance.....	18
3.3.1. <i>Optical properties and layer thickness</i>	18
3.3.2. <i>Substratum properties</i>	19
3.3.3. <i>Contamination, rejuvenation and protection</i>	21
3.4. Performances of Cs ₂ Te photocathodes	23
3.5. Preparation conditions of Cs ₂ Te photocathodes	24
3.5.1. <i>Stanford Electronics Laboratories</i>	25
3.5.2. <i>Istituto Nazionale di Fisica</i>	25
3.5.3. <i>Fermi National Accelerator Laboratory</i>	26
3.5.4. <i>Los Alamos National Laboratory</i>	26
3.5.5. <i>Centre Européen pour la Recherche Nucleaire</i>	27
3.5.6. <i>Research Center Rossendorf</i>	27
3.5.7. <i>University of Twente</i>	27
3.6. Conclusions and new model	30
3.6.1. <i>Propositions</i>	31
3.6.2. <i>Explanations</i>	32
4. Diagnostics.....	35
4.1. Introduction.....	35
4.2. X-ray Photoelectron Spectroscopy	36
4.3. Single Wavelength Ellipsometry	41
4.3.1. <i>Theoretical aspects</i>	41
4.3.2. <i>Delta/Psi trajectories</i>	44
4.4. Diagnostic setup.....	46
4.5. Conclusions.....	53

5.	Magnesium photocathodes.....	54
5.1.	Magnesium photocathodes overview.....	54
5.1.1.	<i>Photocathode structure</i>	54
5.1.2.	<i>Increasing the QE</i>	55
5.1.3.	<i>Response time, linear and non-linear QE response</i>	60
5.1.4.	<i>Conclusions</i>	62
5.2.	Magnesium photocathode test preparation chamber.....	63
5.2.1.	<i>Physical Vapour Deposition</i>	63
5.2.2.	<i>Evaporation source</i>	66
5.2.3.	<i>Cathode</i>	67
5.2.4.	<i>Thickness measurements</i>	67
5.2.5.	<i>Laser system and electron detection</i>	68
5.2.6.	<i>Additional components</i>	68
6.	Conclusions.....	71
	References.....	73
	Appendix 1: Overview of photocathodes.....	79
	Appendix 2: Model diagnostic setup.....	82
	Determination of the change in delta.....	82
	Rewriting the Fresnel coefficients for reflection.....	83
	Appendix 3: Overview of Mg photocathodes.....	86
	Overview of Cu cathodes at the same research groups.....	91
	Appendix 4: Inventory of risks and protocol of handling.....	94
	Appendix 5: Recommendations.....	96

Preface

During the eleven months of graduating at the Laser Physics and non-linear Optics group at the University of Twente, I greatly enjoyed working on the experimental and theoretical research about photocathodes. I learned a great deal more of physical subjects and performing experimental physics.

I would like to thank the people who contributed to the results presented in this report. First of all, my supervisors Jeroen Verschuur and Prof. Klaus Boller for their valuable advices and for correcting my thesis report. I also thank Jeroen for his motivation and the pleasant discussions. I also want to thank Herbert Wormeester for his advice concerning diagnostics and Andrei Zinine for the performed XPS measurement. I am grateful to Gerard Oude Meijers for his help with practical work and designing the preparation chamber for magnesium photocathodes. I also thank the other members of the group for given suggestions and the pleasant working atmosphere. Thanks to my friends for the moments of laughter. Special thanks go to my family who supported me through all these years.

1. Introduction

New ground breaking research possibilities are expected for condensed matter physics, chemistry, materials science, and structural biology with the use of the X-ray Free Electron Laser (XFEL)¹. With the expected high-intensity, ultra short X-ray laser pulses it could be possible, for example, to literally monitor molecular binding and folding processes with atomic spatial resolution and with attosecond temporal resolution. It is believed that this will open up new perspectives for the future, for example new fundamental insights in many natural sciences and the development of new materials in the nano region needed in electronics or for the development of new and more effective medicines.

For the XFEL to operate successfully, a highly relativistic electron beam of extremely high quality is required, for which the generation of electron bunches by means of photocathodes has proven to be the key method. The basic principle of such photocathodes is that the cathode is illuminated with e.g. UV radiation, to excite electrons, which are subsequently emitted for further acceleration. The relevant properties of photocathodes are their quantum efficiency, spectral response, operational lifetime, temporal response, damage threshold, the transverse energy spread of the emitted electron beam, dark current and high average current density and operational conditions like the required quality of the surrounding vacuum and the maximum tolerable applied field for acceleration [1]. Depending on the application and the corresponding electron beam requirements, the proper photocathode has to be selected and prepared, which is a highly complicated task. In general, one can say that metallic photocathodes are fast, inefficient and have a long lifetime. Semiconductor photocathodes are slow, efficient and have a short lifetime. However, the diversity amongst especially semiconductor photocathodes is rather large.

As a first example, the realisation of Laser wakefield accelerators (LWFA) require sub-picosecond electron bunches [2]. To generate such short electron bunches a photocathode with a very short (femtosecond) response time is necessary. Metallic photocathodes fulfil this requirement. Within the Laser Physics and Non Linear Optics Group of the University of Twente an alternative injection scheme is used which is called the Khachatryan method². Extremely short relativistic electron bunches will be generated by inserting an electron bunch of picosecond duration or less.

Another example is electron accelerators for infrared or visible FELs and electron-positron colliders. These require rather a high quantum efficiency (QE) photocathode with a long operational lifetime, while a femtosecond long response time is not required. As part of the European project Coordinated Accelerator Research in Europe, a Joint Research Activity for Photoinjector (CARE-PHIN)³ we accurately study the preparation and performance of photocathodes that produce high charges for application in such electron accelerators.

¹ http://www.desy.de/html/aktuelles/xfel_mou_en.html

² <http://www.tn.utwente.nl/lf/project.php?projectid=8&submenu=16>

³ <http://www.infn.it/phin/>

1.1. *Aim of research*

This report describes the research performed on photocathodes for two different projects.

- The first is the CARE-PHIN project, the objective of which is to improve the characteristics of the electron sources for future electron-positron colliders. A part of that research is to improve semiconductor photocathodes, mainly focusing on lifetime and quantum efficiency (QE) under operational conditions of high average beam load. For being successful with this goal it turned out that the fabrication technology has to be improved and that additional basic knowledge on photocathodes and new materials has to be obtained. From the overview in chapter 2 it is concluded that nowadays the best semiconductor photocathode is Cs₂Te, as it seems to offer the best compromise between lifetime and QE. However, the general belief that Cs₂Te is the best choice is, actually, based on weak arguments. This can be seen from the fact that reports on the performance of this photocathode differ a lot between the various groups that use it. Furthermore, this lack of reproducibility seems to be related to problems in controlling the preparation process for these photocathodes. In this research we investigate the preparation processes of Cs₂Te photocathodes with the first goal to hand an enhanced insight in the process and show how a better reproducibility can be gained in the preparation and performance of Cs₂Te photocathodes. For this purpose a diagnostic setup has been designed.
- The second goal of this work is to investigate a suitable photocathode to produce fs electron bunches for injection in a plasma channel for laser wakefield accelerators, including the LWFA project at the Laser physics and Non Linear Optics Group of the University of Twente. A short electron bunch is needed to test the principle of wake field acceleration. As the latter is, worldwide, still not realised, it appears sufficient to first focus on a ‘high quality’ photocathode. This term means that for this application the photocathode must have a short response time and have a reasonably high QE so that the photocathode can be illuminated with low laser powers and still produces reasonably high charges. Based on a comprehensive review of observation of others, we decided to use a magnesium photocathode and have designed and build a test setup to prepare and study such photocathodes.

In chapter 2 the theory of photoemission is recalled and an overview of photocathodes in general is given. In the next chapter Cs₂Te photocathodes are discussed. Presuppositions are discussed for the formation of these photocathodes. Diagnostics are necessary to verify these assumptions, which will be discussed in chapter 4. In chapter 5 an overview on various properties of magnesium photocathodes is given and the design of a test preparation chamber is described. Conclusions and recommendations for further research are made in the last chapter.

2. Photoemission and photocathodes

In order to provide a basic understanding of the general differences between metallic and semiconductor photocathodes, we first describe the working principle of photocathodes and illustrate the fundamental differences between photocathodes made of metals and photocathodes made of semiconductors. To choose the best photocathode for a particular application, one needs to be aware of some detailed properties, especially their strong and weak points with respect to other photocathodes. Therefore, in the second section of this chapter we present an overview of previous work on photocathodes.

2.1. Photoemission in photocathodes

The photoemission of electrons can be explained with a three-step model [3], which also explains the difference in performance between metallic and semiconductor photocathodes. Figure 1 shows the typical band structure of metals and semiconductors. The first step of photoemission is optical excitation of electrons from the valence band into higher empty states in the conduction band. In the second step, a part of these electrons migrates to the solid surface, either directly or by experiencing scattering with the lattice or other electrons. The final step is the escape across the surface potential barrier into vacuum of those electrons that have sufficient energy left at the surface.

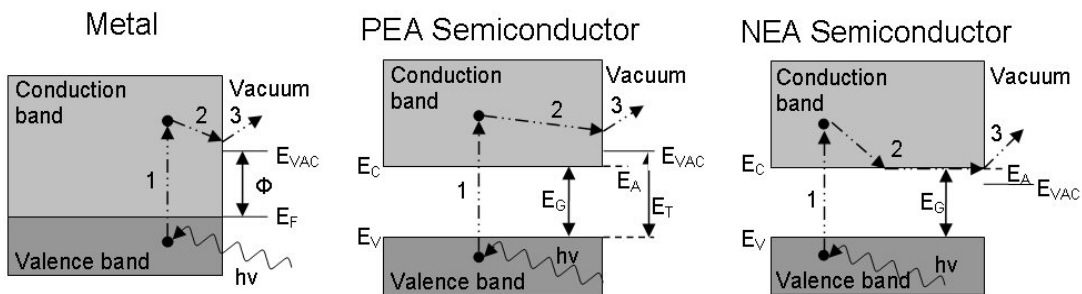


Figure 1: Photoemission in 3 steps for metallic and, respectively, PEA and NEA semiconductor photocathodes.

Usually, the first step (photo excitation) is more efficient for semiconductors compared to metals for two reasons: first, the surface reflectivity of semiconductors is lower than that of metals, and secondly, the absorption coefficient for photon energies above the band gap energy E_G of semiconductors is often very high (see [4], page 6). Because of the band gap, semiconductor photocathodes show a relatively sharp onset of photoemission as the frequency of the incident light is increased beyond a threshold value.

In metallic photocathodes the electrons are excited into the conduction band. However, in a metal there is an abundance of free electrons in the conduction band due to gradual transitions of thermally excited electrons from the valence band that is overlapping the conduction band. Thus when photoexcited electrons move to the vacuum interface, they encounter a high number of scattering events

with free electrons from the Fermi sea and thus thermal equilibrium is approached within a short distance. Only the small part of the electrons that are excited very close to the surface and which have not thermalized when reaching the surface, still possess sufficient energy to escape across the surface potential. This short distance (typically a few nm for metals) is called the escape depth. In contrast to metals, the conduction band in semiconductors is almost empty before photoexcitation, such that electron-phonon scattering is the dominant loss process. The corresponding losses are much smaller per collision compared to electron-electron scattering. Consequently, the photoelectron lifetime (time when thermal equilibrium is reached) is longer and electrons from deeper regions can reach the surface. Thus the escape depth, which is the average distance from where excited electrons have a $1/e$ probability to escape, in semiconductors may be several times larger than the mean free path, which is the average distance between two sequential collisions.

For the efficiency of the third step of photoemission, the surface potential is of high importance. The surface barrier of metals that the electrons have to overcome is the work function ϕ , which is the difference between the vacuum energy level and the Fermi level. For most metals, this value is high (a few eV) so that high-energy photons are required to excite electrons. For semiconductors a distinction can be made, namely between the positive and the negative electron affinity materials (respectively PEA, like Cs_2Te and Cs_3Sb , and NEA like GaAs). In PEA semiconductors, the electrons can escape if their energy is higher than the sum of the band gap energy and the electron affinity E_A . The vacuum level lies above the bottom of the conduction band such that thermal electrons cannot be emitted into vacuum but recombine back into the valence band, after typically a few ns. Contrary to this, in NEA photocathodes, the vacuum energy level lies below the bottom of the conduction band [5]. Electrons that thermalize through electron-phonon collisions to the bottom of the conduction band can still be emitted into vacuum. These electrons are in a metastable state, i.e. the time before they recombine back into the valence band is long, in the order of nanoseconds. Thus the escape length is rather long for NEA photocathodes, which results in a combination of high QE and long response time.

There are some additional factors that determine the QE and photoemission threshold from semiconductors ([4], see page 9). The first factor is the ratio $E_G:E_A$. An empirical ‘rule’ states that semiconductors with $E_G:E_A > 1$ have a higher QE than those with $E_G:E_A < 1$. The explanation for such rule is that excited electrons in the latter type have sufficient energy to raise a second electron from the valence band into the conduction band. Neither of the two free electrons has sufficient energy left to escape into vacuum. Such quenching of the photoemission is often dominating the process of direct escape into vacuum.

Another factor that has to be considered is bending of the band structure due to defect levels (impurities) close to the surface. Such band bending decreases (or increases) the electron affinity E_A to an effective value $E_{A\text{eff}}$ (Figure 2). The band bending distance must be smaller than the escape depth in order to result in a higher (or lower) QE [6].

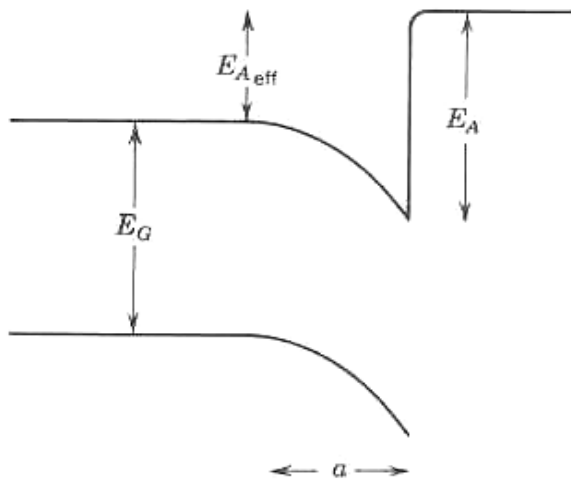


Figure 2: Band bending can decrease the effective electron affinity and thereby increase the probability of photoemission.

2.2. Overview of photocathodes

A comparison between several types of photocathodes with respect to QE, lifetime, vacuum condition and response time, is presented in Appendix 1, which was obtained after carefully analysing the observations found in a large number of previous publications. The comparison contains two main classes of photocathodes, namely metallic and semiconductor photocathodes. We paid limited attention to thermionic [1], [7] ferroelectric and ceramic photocathodes [1], [8], [9] because of their rather long response times and because there are no other important advantages over metallic or semiconductor photocathodes for application in electron accelerators for electron-positron colliders and FELs.

2.2.1. Metallic photocathodes

Metallic photocathodes offer several clear advantages over semiconductor photocathodes. First, they are the most robust photocathodes against degradation due to surface contamination and therefore do not require ultra high vacuum conditions⁴ [1]. Second, they are robust against damage resulting from conditioning or heating. Also they can withstand high electric surface fields, such as present at the cathode in RF accelerators, while other types of photocathodes materials may suffer from electric breakdown. Other advantages of metallic photocathodes are their very short response time (less than picoseconds) and their very long lifetime (years or longer), which is much longer than of other types of photocathodes (hours to months). However, the main problem with metallic photocathodes is the rather low quantum efficiency (QE), even for UV radiation. This is due to their high reflectivity, shallow escape depth because of electron scattering, and large barrier at the surface (high work function).

In Appendix 1, the properties of several metallic photocathodes are tabulated. Copper is the most robust photocathode, and is insensitive to air. However, it has

⁴ <http://ucq.home.cern.ch/ucq/Photocathodes.htm>

the lowest QE (10^{-5} to 10^{-4} at 266 nm) [1]. Barium has the best spectral response (highest QE at longer wavelength) but is less robust and cannot withstand high electric fields. Yttrium and samarium have low work functions and may be more robust than Ba. Magnesium has a respectable QE of $6 \cdot 10^{-4}$ at 266 nm. Furthermore, it seems to be possible to increase the QE by another order of magnitude when laser cleaning is applied [10]. Thus, so far the most promising metallic photocathode is magnesium. This photocathode will be discussed extensively in chapter 5 for the purpose of the LWFA project.

Another reported possibility to improve the QE of metallic photocathodes is ion-implantation, which combines the advantages of semiconductor (high QE) and metallic photocathodes (robustness) [11]-[13]. Cs or K ions are implanted to a depth of 30 nm in a metal substratum, e.g. Mg or W. It is qualitatively observed that the lifetime of these photocathodes is longer than that of semiconductor cathodes. The QE is a factor of 10 larger than that of pure metallic photocathodes, but still much lower than of semiconductor photocathodes. An additional advantage is its broader emission spectrum, which makes it possible to use a green laser that can be easily provided with second harmonic generation, and thus with high power and better power stability.

Yet another approach is to optimise the concentrations of the elements in binary metallic alloys A_xB_{1-x} , with the goal to lower the work function with respect to the work functions of the pure constituents A and B. An approximate equation for the work function of a binary alloy is given by [14], [15]

$$\phi = x\phi_A + (1-x)\phi_B + x(1-x) \left[\frac{(\phi_A - \phi_B)(\rho_A - \rho_B)}{x\rho_A + (1-x)\rho_B} \right]$$

where ρ is the effective total density of states of the pure elements. Of particular interest in this equation is that the last term can become negative. For instance, the Mg-Ba alloy with 2.1% Ba (optimum Ba coverage) possesses a lower work function than both the work functions of Mg and Ba, which leads to a QE of about 10^{-3} at 266 nm [16]. This value is larger than that of uncleaned magnesium photocathodes. A disadvantage of the Mg-Ba photocathode is its low lifetime that is most likely due to laser-induced Ba evaporation.

2.2.2. PEA semiconductor photocathodes

Semiconductor photocathodes have a much higher QE than metallic photocathodes, reaching values in the order of 10%. However, the lifetime is much shorter. The lifetime for semiconductor photocathodes is defined as the (operational) time over which the QE remains larger than 1% [1]. Another disadvantage is their high sensitivity to contamination by oxygen, CO_2 and water, which requires working in more stringent ultra-high vacuum conditions. Moreover, the response time is longer, typically in the range of tens of picoseconds, which makes them unsuitable for femtosecond electron bunch generation.

As mentioned before in paragraph 2.1, semiconductors can be distinguished between PEA and NEA semiconductors. There exist several types of PEA semiconductors: alkali-telluride, alkali-antimonide and alkali-halide.

Alkali-telluride photocathodes have larger QE's and longer operational lifetimes than alkali-antimonide photocathodes. In addition, they offer the possibility of partial rejuvenation by means of heating. A disadvantage is the requirement to use UV laser light. Such light is usually provided by means of quadrupling an infrared Nd solid-state laser, which suffers from a lower generation efficiency and which decreases the power stability of the UV [17]. Among the alkali-telluride photocathodes, Cs₂Te is the most widely used one because of its relatively long potential lifetime (up to months) and high QE compared to other semiconductor photocathodes [18]-[23]. A QE of 8 – 12% is consistently obtained at illumination with ~263 nm radiation under operational conditions (usually this means applying an RF field on the cathode while illuminating it with laser pulses, in about 10⁻⁸ Torr⁵ vacuum conditions). An even higher QE is obtained at about 254 nm (radiation from a mercury lamp used during preparation) when stored in the preparation chamber with improved vacuum conditions (10⁻⁹–10⁻¹⁰ Torr). Cs₂Te also has a good resistance to laser damage. Furthermore, it is less sensitive to contamination than alkali-antimonide photocathodes. In addition, it has a comparatively shorter response time (~ ps), a higher current density and a lower dark current than most other semiconductor photocathodes. However, especially when high currents are extracted from the photocathode, the operational lifetime decreases quickly. Actually, an operational lifetime of about a month is the utmost.

K-Te photocathodes are the most robust alkali semiconductor photocathodes and have the longest operating lifetimes. Degradation occurs only during operation, and no change in QE has been observed after storage in the preparation chamber. A drawback is the relatively low QE (a few percent), and the need for generation of the 5th harmonic of a Nd based laser because of a large work function [24]-[27]. CsKTe has the largest QE, initially 22.5%, but its performance under operating conditions is not as good as Cs₂Te: the QE drops rapidly (within hours) to a level lower than that of Cs₂Te. After 20 hours operation the QE degradation stabilises to a level of 2%. It was expected that the lifetime stability could be improved by optimising the layer thicknesses of Te, K and Cs [20], [28], [29], but no success is reported yet.

Alkali-antimonide photocathodes have the advantage of a good response to green laser light due to their small band gap. Their disadvantage is that operational lifetime is only a few hours because of their high sensitivity to contamination [1], [19], [29]. So far, the best alkali-antimonide photocathodes are K₂CsSb and Cs₃Sb. They have a QE of about 1 to 8 %. An interesting possibility might be the use of UV laser light, which can increase the QE significantly (30-35% for 300-360 nm) [30].

A record-high QE can in theory be obtained with Li₂CsSb photocathodes [31]. The photoelectron diffusion length is significantly larger than in all other semiconductor photocathodes because the photoelectron lifetime is prolonged by several orders of magnitude. Consequently, the emissive layer can be made significantly thicker and therefore more efficient. However, the response time is

⁵ 1 Torr = 1.333 mbar = 133.32 Pa

close to the nanosecond range, which excludes the generation of even ps electron bunch generation for accelerators.

Alkali-halide photocathodes like CsI are relatively robust and can be transported in air. However, the high work function requires deep UV radiation for electron photoemission [27] and still yields only small values of the QE (2%). A thin germanium coating improves the QE at 262 nm to about 0.13 %. Somewhat problematic is an unexpected behaviour in a RF gun where satellite bunches and saturation have been observed [1].

2.2.3. NEA semiconductor photocathodes

NEA photocathodes are prepared by adsorption of electropositive elements, like Cs or a combination of Cs and O, to reduce the work function such that the vacuum level lies below the lower edge of the conduction band. Typical NEA semiconductors are Si, GaAs, GaN and GaP. The QE is generally higher than that of other photocathodes (> 20 % at UV radiation), but the response time is longer (several hundred ps to ns) which, again limits their use for ultra-short electron bunch generation. Also, no high currents can be drawn from these cathodes without damaging the surface.

There are several carbon-based photocathodes [32], [33], like polycrystalline diamond, hydrogenated amorphous carbon and nanostructured fullerene films. Polycrystalline diamond photocathodes are chemically inert, have a high damage threshold but also a low QE of 10^{-6} . Hydrogenated diamond photocathodes have the highest QE's of $8 \cdot 10^{-4}$ for 213 nm wavelength, but have low damage threshold and become oxidised after irradiation. Similar to the other NEA photocathodes, the response time of these carbon-based photocathodes is expected to be long [1], which again excludes them for ultra short electron bunch generation.

2.2.4. Miscellaneous photocathodes

The Ag-O-Cs photocathode is the only photocathode that is sensitive to infrared light [4]. However, the QE is only about 10^{-3} . It was possible to increase the QE slightly (by about 16%) due to an internal assistant field [34], though this is still not sufficient for the production of high charged electron bunches, such as required in RF accelerator based FEL's.

All semiconductor photocathodes are sensitive to oxygen and other electro-negative atoms, which affects their lifetimes even when not in operation. In order to improve the lifetime of semiconductor photocathodes, they could be protected with a thin solid film, for example with LiF, CsF, SiO₂, Al₂O₃, CsI, CsBr [35]. In some cases, removable organic HTC (hexatriacontane) [36] is used if only protection during transport is needed. The investigation on the performances of protection layers was concentrated on the highly reactive Cs₃Sb and KCsSb photocathodes. It was found that KCsSb can be best protected with a thin film of CsBr [30]. For example, a KCsSb photocathode with a 280-300 Å CsBr film could withstand an exposure to 150 Torr of oxygen for half an hour and

maintained a QE of 5% at 312 nm laser light (the QE was 30-35% at 312 nm without a cover layer). Thicker layers can withstand higher exposures to oxygen, but the initial QE is lower by increasing layer thickness. A much thinner layer is sufficient if the maximum pressure is only 10^{-5} Torr. CsBr failed to protect the photocathode against moisture. No measurements on the lifetime were performed. A next best alternative for KCsSb photocathodes is CsI [37]. Cs₃Sb photocathodes were protected with 150 Å NaI, but had a lower resistance to oxygen and a lower QE than the protected KCsSb photocathodes [35].

It appeared that the protection capability of the cover layer is influenced by lattice constant matching between the photocathode itself and the protection material [30]. The only reported research on protection layers for Cs₂Te photocathodes is presented by LANL and CERN who have tested thin CsBr protective cover films on Cs₂Te photocathodes [38], [39]. At CERN a 2 nm CsBr layer was applied and obtained only a decrease in QE but not the expected improvement of storage lifetime. At LANL a 40 Å CsBr was applied. The initial QE decreased from 10% to 5-6% but remained indeed stable for more than two months of operation without any sign of degradation. However, it is not clear at which conditions the photocathode was tested. The lattice constant matching of CsBr and Cs₂Te is also unknown. As a conclusion of these experiments, CsBr is not necessarily the best protection layer for Cs₂Te photocathodes.

Boscolo et al. [40] tested thin (< 70 nm) nanostructured carbon films deposited on metallic photocathodes and proposed that this may be a good protective layer for alkali photocathodes since carbon is a very robust material. However, no further results were reported on this.

All the previously mentioned photocathodes use a common surface for illumination and electron emission. In addition, other configurations have been investigated such as back illumination of thin photocathode films [41] and secondary enhanced emission [42]. For the latter, a diamond window multiplies the number of (primary) electrons coming from a photocathode. In this way, less power is required for photocathodes with a lower QE while the cathode is protected from contamination from the gun. However, the preparation and construction are arduous in comparison with the standard photocathodes.

2.3. Conclusions

There are two main classes of photocathodes which have to a large extent contrary performances with respect to quantum efficiency, spectral response, operational lifetime, temporal response and damage threshold. This mainly can be attributed to the band structures of the materials and can be explained qualitatively by the three-step model for photoemission. Semiconductor photocathodes have high QE's but short lifetimes.

According to our extensive literature research and comparison, the best compromise for applications such as in the CARE-PHIN program is Cs₂Te. The most promising photocathode for laser wakefield accelerator application, requiring a response faster than a picosecond with still a maximum QE, is magnesium. Thus, to achieve the goals set in this research, we decided to focus on two types of photocathodes, namely Cs₂Te and magnesium.

3. Cs₂Te photocathodes

Cs₂Te appears to offer the best compromise between QE and lifetime for standard electron accelerator applications in FELs and electron-positron colliders. However, in the reports on this photocathode of the various groups that use it, the performances differ a lot. The inconsistent observations seem to be related to problems in controlling the preparation process for these photocathodes. To get an enhanced insight in the preparation process and to show how a better reproducibility can be gained in the preparation and performance of Cs₂Te photocathodes, in this chapter, we start with describing the spectral response of Cs₂Te. In particular, we observe that this is not a well-defined, unique curve, which clearly indicates the irreproducibility of Cs₂Te photocathode preparation. We inspect various shapes of the observed spectral response by discussing the current beliefs on the composition of Cs₂Te. After that, parameters that influence the QE and lifetime are discussed. Taking into account these parameters, the operational performances (discussed in the following paragraph) of Cs₂Te photocathodes prepared by various groups still differ to an extent that cannot be explained by available models. We concluded that not only these general parameters are important, but that the preparation conditions have a significant influence on the resulting performance of the photocathodes. A thorough comparison and discussion of the various preparation procedures of the several groups is presented in the second last section. In the last section we conclude with a model of the preparation process and compare the predictions with the measured spectral response.

3.1. Spectral response

In 1953, Taft and Apker discovered that Cs₂Te has a very strong photoemission when exposed to UV light [4]. Since then it has been used as a photocathode in photodiodes [43] and photomultiplier tubes. Such photocathodes are usually prepared by depositing tellurium (Te) and subsequently cesium (Cs) on a suitable substratum, mostly molybdenum (Mo). Actually, it should be noted that the term “Cs₂Te” merely describes the approximate chemical composition, or the ideal ratio of Cs and Te in a stoichiometric film, while not much is known about the actual composition.

The spectral response of Cs₂Te on a Mo substratum, as provided by measurements of various other groups, is summarised in Figure 3. Curves A and B correspond to extremes of Cs₂Te, respectively without and with excess Cs, as measured by Taft and Apker. In practice, the preparation process of Cs₂Te photocathodes is not sufficiently under control to fabricate precisely certain compositions in a reproducible way. Consequently, the spectral response of most cathodes will be in between these two curves ([4], see page 180). Exceptions on this non-reproducibility are highly controllable preparation processes like at INF Milano. Curves C (Cs₂Te) and D (evaporated Te before reaction with Cs) are measurements from Powell et al. [3]. Curve E is the spectral response of Cs₂Te measured at Los Alamos National Laboratory (LANL) [21], [44]. Indeed, curves C and E lie in between the extremes A and B.

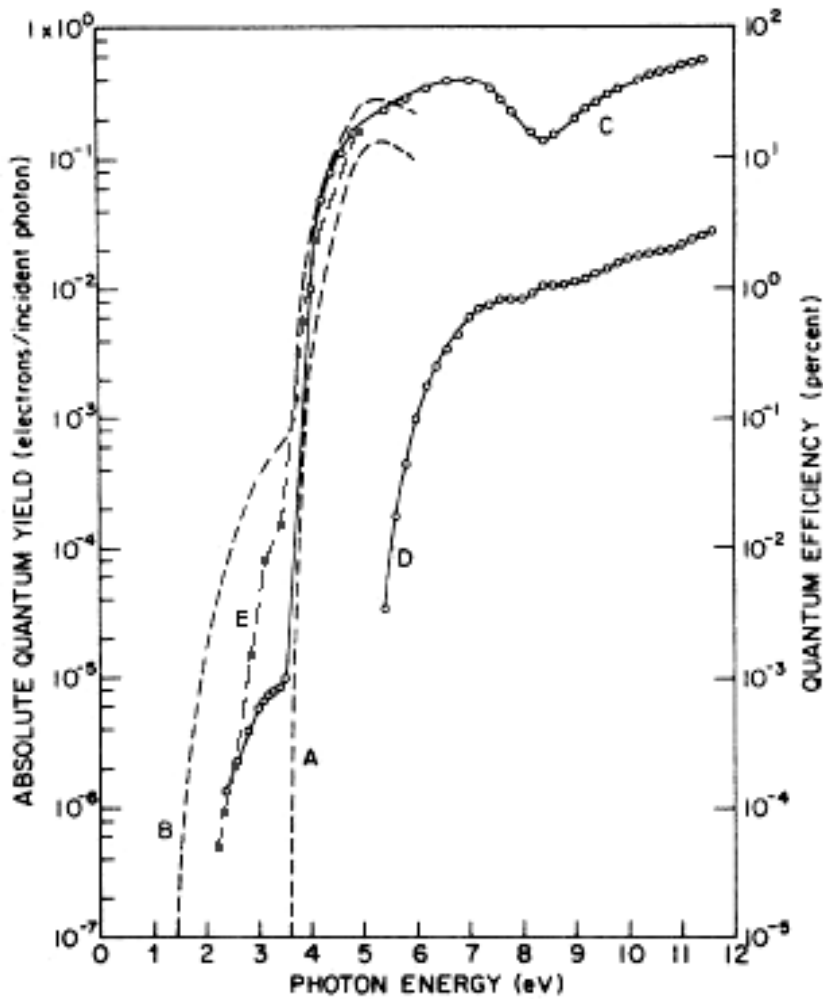


Figure 3: Spectral distribution of the quantum efficiency of Cs_2Te cathodes. Curve A and B are QE curves respectively without and with excess Cs (Taft and Apker). Curve C Curve D is the QE of evaporated Te before reaction with Cs. Curve E is data from Los Alamos [44].

Characteristic features are visible in the spectral response of Cs_2Te . Without excess Cs, it shows a sharp threshold at around 3.5 eV, while with excess Cs, there is a small typical shoulder noticeable starting from around 1.5 eV. It can be seen from Figure 3 that the QE at 4.88 eV (254 nm mercury-line) is about 16% and for 4.66 eV (266 nm) the QE is about 12%. The QE has a maximum of 40% for photons of 7 eV. At higher photon energies, the spectral curve shows a dip.

We explain these features by the three-step model of photo excitation discussed in chapter 2.1 and the schematic energy-level diagram for Cs_2Te given in Figure 4. The band gap E_G of Cs_2Te is 3.3 eV and the electron affinity E_A is 0.2 eV ([4], see page 220). So Cs_2Te is a p-type semiconductor photocathode with a large $E_G:E_A$ ratio, which is consistent with the previously stated 'rule' that such photocathodes have high quantum efficiencies. The threshold energy of 3.5 eV equals $E_G + E_A$. The sharp threshold is indicative of a small valence band (about 2 eV) [3]. For photon energies less than $2E_G$ the only losses are through electron-phonon scattering, which are extremely small. For higher photon energies, inelastic

electron-electron scattering (pair production) sets in with as result a decrease in QE, clearly visible in the graph. For even higher energies, the QE rises again due to secondary electron emission. This explains the appearance of the previously mentioned dip at around 8 eV.

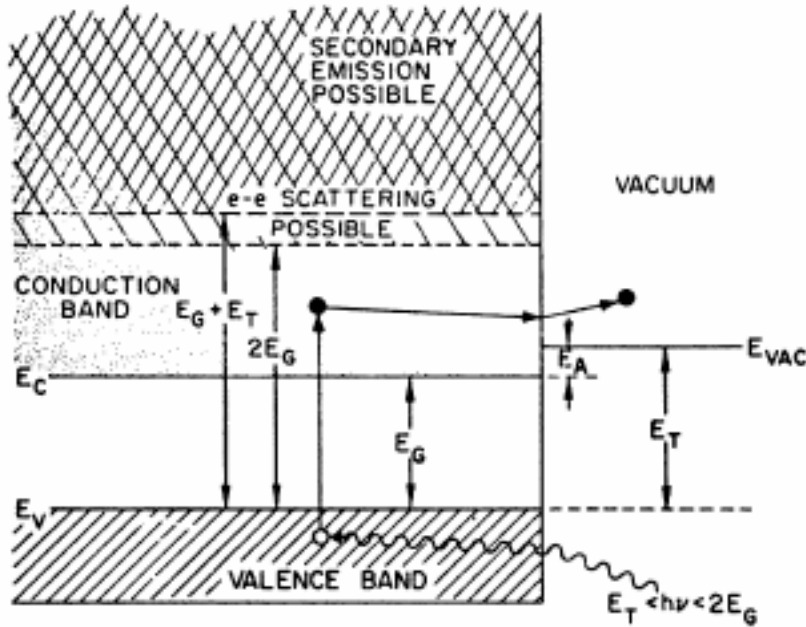


Figure 4: Schematic energy-level diagram of Cs₂Te. $E_G = 3.3$ eV, $E_A = 0.2$ eV. The minimum threshold for electron-electron scattering ($2E_G$) and for secondary electron emission ($E_G + E_T$) are also indicated.

3.2. Composition

For many years, the typical shoulders below 3.5 eV were ascribed to an excess of Cs at the surface of the cathode. For example, it was observed that the threshold wavelength could be made smaller in three ways: the first is to stop the exposure of Cs vapour before the photocurrent, created by a UV lamp and monitored during the preparation process, reaches its maximum. Secondly, if additional Te is evaporated on the cathode to compensate (to some extent) for excess Cs, the shoulder decreases. Another method was baking of the photocathode after the preparation. Neither this subsequent baking nor additional Te evaporation could, however, reduce the shoulder completely. From this it was believed that the excess Cs is bound in an energetically very stable configuration [4]. Contrary to this, Spicer proclaimed the effect to the existence of more than one phase of Cs₂Te, since a prolonged exposure to Cs and subsequent baking reduced the shoulder again to end up with the characteristics of bulk Cs. The presence of multiple phases was confirmed by Di Bona et al. [45], [46] who analysed the formation of Cs₂Te photocathodes with AES and XPS (methods that yield the atomic fractions in a sample). They observed the formation of different compounds before the assumed stoichiometric Cs₂Te is formed, noticeable in the stepped behaviour of the QE during Cs deposition (see Figure 5). The preparation of Cs₂Te was performed in the following way: first, a layer of 10 nm Te was

deposited onto a Mo substratum, before Cs was evaporated. When Cs was deposited, initially a two-phase system of pure Te and $\text{Cs}_{1.2}\text{Te}$ was formed. More Cs deposition resulted in a decrease of pure Te, an increase of $\text{Cs}_{1.2}\text{Te}$ and an extra Cs_xTe compound with $x > 2$ forming at the surface. This phase is the same as the before-mentioned bound Cs proclaimed by Sommer. At 70 nm Cs deposition, a maximum photocurrent was reached, and the formation of the photocathode seemed completed. It was assumed that then the composition is made of the two components $\text{Cs}_{1.2}\text{Te}$ and $\text{Cs}_{x>2}\text{Te}$, together forming an average of Cs_2Te . During this formation process, the QE increased for all wavelengths but more significant in the low-energy part of the spectrum, making the shoulder larger.

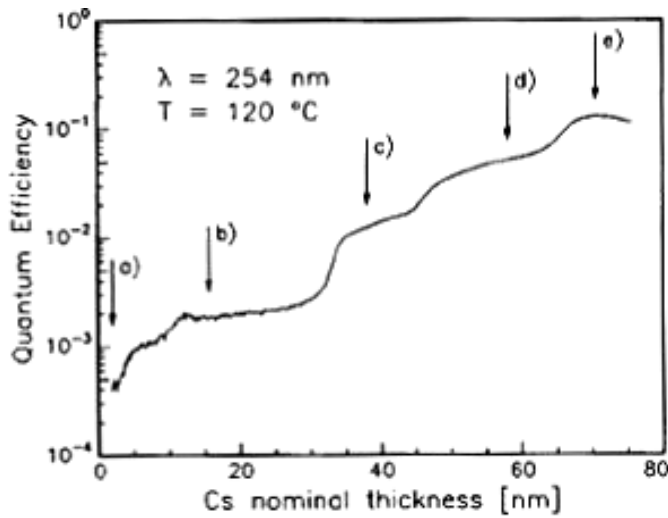


Figure 5: Quantum efficiency as a function of Cs nominal thickness at 254 nm during the formation of Cs_2Te on a Mo substratum. The stepped behaviour suggests that the formation takes place through different phases. At a) the deposition of Cs on pure Te starts and a $\text{Cs}_{1.2}\text{Te}$ starts to form at b). At c) a two-phase system of pure Te and $\text{Cs}_{1.2}\text{Te}$ is formed. At d) the Cs_xTe with $x > 2$ starts to form. The photocathode is completed at e).

The measured depth profile of these completed Cs_2Te photocathodes is given in Figure 6. It shows a uniform profile for 20 nm of the surface and an interfacial mixed-phase Mo-Cs-Te of about 5-10 nm thickness. The latter would probably be of no concern for the QE since it lies below the escape depth of the photoelectrons. Ferrini et al. [47] estimated the electron escape depth to be 8 nm (which appears to be rather small) and the mean free path to be 3 nm for a 30 nm Cs_2Te film on a Mo substratum, which supports this assumption.

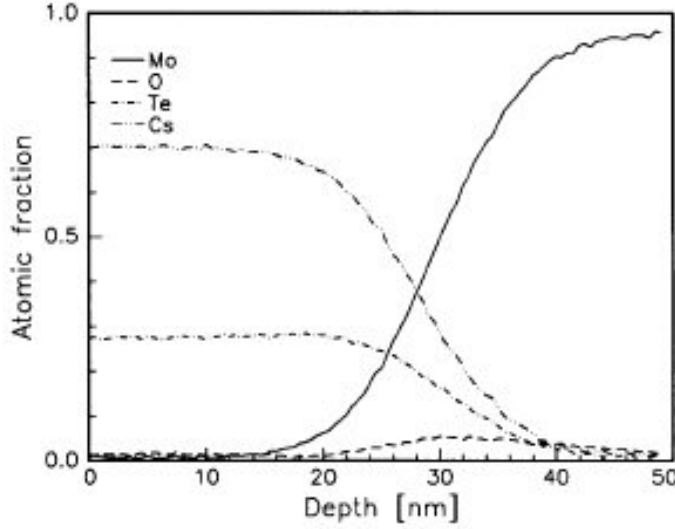


Figure 6: Auger depth profile of a Cs_2Te photocathode on a Mo substratum.

The actual Cs-to-Te ratio of the formed Cs_2Te was measured to be 2.5 as concluded from the ratio

$$\frac{N_{Cs}}{N_{Te}} = \frac{\rho_{Cs} t_{Cs} m_{Te}}{\rho_{Te} t_{Te} m_{Cs}},$$

where t is the evaporated thickness (or the nominal thickness if the sticking coefficient of Te and Cs are equal), $\rho_{Te} = 6.25 \text{ g/cm}^3$, $\rho_{Cs} = 1.90 \text{ g/cm}^3$, $m_{Te} = 127.6 \text{ u}$ and $m_{Cs} = 132.9 \text{ u}$ ([48], see page 67 and 79). This means that for 10 nm Te a layer of 68.5 nm Cs is required to obtain a ratio of 2, which is very close to the nominal thickness of 70 nm in Figure 5. From this it seems that on a Te layer of, for example 30 nm, a Cs layer of 205.6 nm is to be deposited to obtain the optimal stoichiometry.

3.3. Parameters that influence the performance

3.3.1. Optical properties and layer thickness

The QE depends, among other factors, on the optical absorption of the illuminated light that actually enters the photocathode. Important parameters are the index of refraction n , the extinction coefficient κ , the thickness of the film, the wavelength of the incoming light and the angle of incidence. Thus maximum optical absorption will be related to the proper stoichiometry of the deposited Cs_2Te photocathode, since that appoints the optical constants of the film. Michelato et al. [49] deduced that n is in the range of 0.8-1.8 and κ in the range of 0.3-0.7 for a wavelength of 254 nm. Johnson [50] determined the optical constants for Cs_2Te at 265.2 nm to be $n = 0.75 \pm 0.01$ and $\kappa = 0.75 \pm 0.01$. The optimal thickness appeared to be 68.5 nm and is approximately two third of the critical thickness (minimal thickness for which the optical properties of the film compares to that of bulk material). Van Oerle ([51], see page 52) calculated the optimal thickness to be 63 nm, using Monte Carlo simulations (see Figure 7). The number of absorbed photons increases with increasing thickness, so a monotonical increase of the QE

can be expected. However, in thick photocathodes the photo-excited electrons are generated deeper inside the layer and therefore the probability to escape into the vacuum decreases [51].

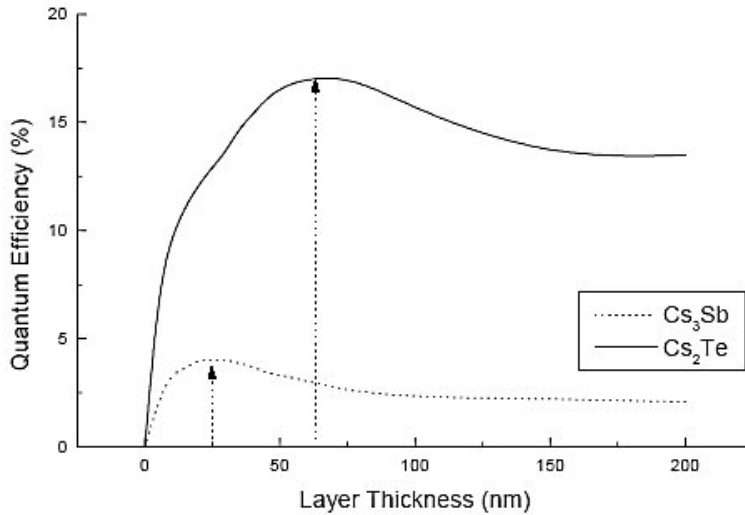


Figure 7: QE as function of layer thickness for Cs_2Te and Cs_3Sb photocathodes, calculated using the Monte Carlo method.

3.3.2. Substratum properties

The growth and hence the performance of Cs_2Te also depends on the substratum. For example, if a copper substratum is used, a lower QE is obtained due to the diffusion of Cu into the photoemissive layer [45]. In Figure 8 an AES scan is given of a Cs_2Te film on a Cu substratum. The figure shows that the film is indeed not uniform in depth and most of the Cs is confined to the first 10 nm. The QE is about 4% at 266 nm.

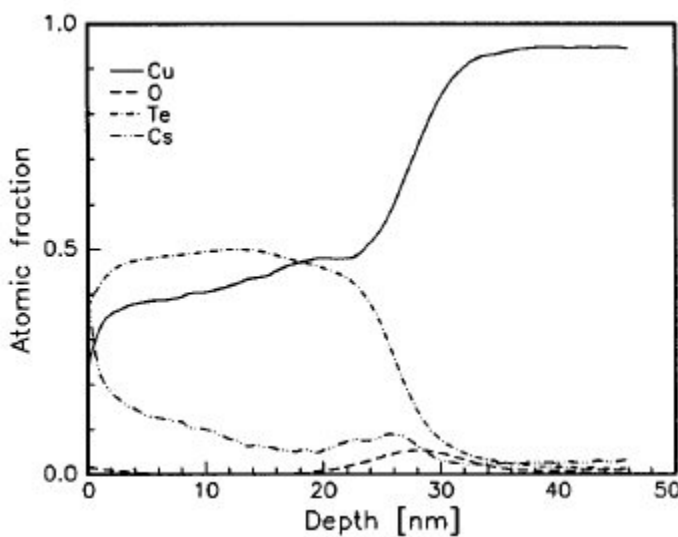


Figure 8: Auger depth profile of a Cs-Te photocathode on a Cu substratum.

A Mg substratum resulted in a high dark current [27] such that this substratum was not further pursued. Cs₂Te photocathodes on gold substrata had high initial QE's but the operational decrease was more rapid than with the other substratum materials [23], [52]. A molybdenum substratum results in a uniform Cs₂Te film of about 20 nm (see Figure 6). Typical QE's with Mo substrata are 8-13 % at 266 nm and even higher QE's are obtained at about 254 nm [1], [18]-[23]. Therefore, so far the best substratum for Cs₂Te photocathodes is Mo. Thus, we have chosen for our own experiments to work with Cs₂Te deposited on a Mo substratum.

Another example of the importance of the substratum is its influence on the growth of vapour-deposited Te. On a Mo substratum, this happens via the Stransky-Krastanov mechanism whereby islands cover an increasing fraction of the substratum [53]. The fractional coverage tend to saturate and leaving a significant fraction of the substratum covered by a very thin Te layer. This growth mode limits the quantum efficiency of the photocathode. The QE scales with the fractional coverage and not with exposure. For example, a nominal deposition of 10 nm Te leads to a fractional coverage of 50 % and islands of 20 nm thick and results in a QE for K₂Te of 4.1%. For 34 nm nominal Te deposition the fractional coverage is 70 % and the QE is 5.5%. In contrast to Mo, the growth of Cs₂Te on Cu substratum forms via islands where not all Cu is covered with Cs₂Te [48]. The deposition rate has no effect on morphology [53]. Thus again, Mo seems to be a better substratum than Cu. Though, a homogeneous distribution of the Te layer might result in higher QE's.

Other parameters that determine the performance of the Cs₂Te photocathode are the temperature of the substratum during deposition, cleaning method and substratum roughness.

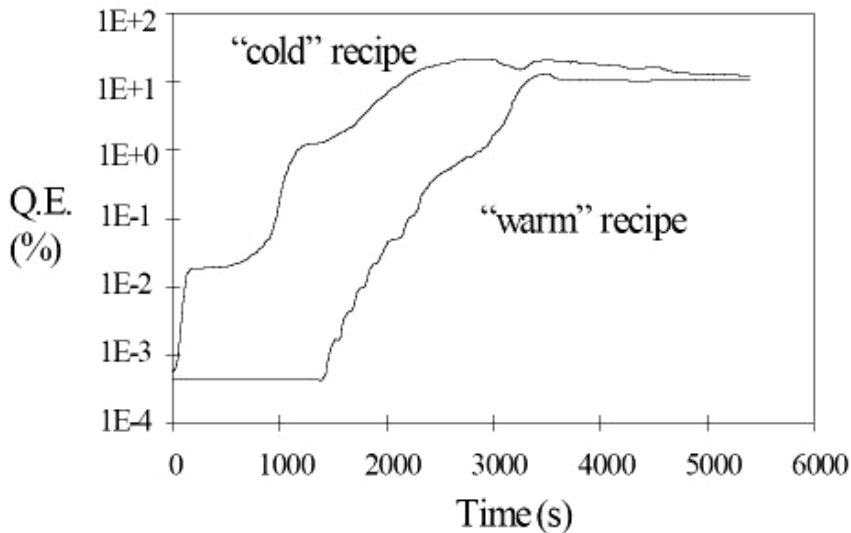


Figure 9: QE behaviour as function of time for different substratum temperature, respectively room temperature (cold) and 120 °C (warm).

If the substratum is kept at room temperature during cathode formation (cold recipe), the final QE of the photocathode turned out to be higher compared to cathodes grown on substrata that are kept at 120 °C (warm recipe), as can be seen

in Figure 9. However, the warm recipe resulted in a more stable QE in time [54]. Both spectral responses showed the typical shoulder. To prevent excess Cs and contaminants from condensing on the film and to facilitate the diffusion and reaction between Cs with Te, the cathode was kept above 100 °C [21].

If the substratum is mirror-like, by polishing with 50 nm diamond powder [18] instead of 1 µm diamond powder [45], the QE is higher and the dark current is significantly reduced. The relationship between QE and dark current is under investigation [18]. The effect of roughness on stoichiometry and thus QE and lifetime is unknown. However, it is plausible that a rough surface influences the growth, for example, the deposited atoms might prefer the “valleys” or the “hills” resulting in a surface that is not completely covered. The growth of thin layers on mirror like surfaces might result in a more homogeneous growth of Te and thus in a higher QE. Alternatively, a smoother surface might change the growth mode. Thus, the roughness of the Mo substratum seems to be an important parameter. No effects are reported on Cu substrata, though similar effects might be expected.

For a used substratum, additional complications arise. When a new photocathode has to be prepared, the remainder of the old photocathode must be removed from the substratum. This appeared to be quite difficult. There remained a residual QE of about 1% after heating the substratum to 600 °C for several hours [51]. Volokhine [55] found that the history of the photocathode influenced the cleaning process. After performing several cleaning procedures after operational use, no new photocathode could be deposited at all. This was not the case when the photocathodes have not been used for operation in the linac (linear accelerator). This indicates that under influence of the laser an alteration of the top layer takes place, for example Cs migrates further into the layer or that there forms some kind of Mo-CsTe phase at the boundary.

The most effective method known to clean the surface in situ is Ar⁺ ion bombardment.

3.3.3. Contamination, rejuvenation and protection

The sensitivity of semiconductor photocathodes to contamination by oxygen, CO₂ and H₂O is considered the main reason for the reduction of the QE and lifetime. To avoid this, ultra-high vacuum is required for preparation and storage of these photocathodes as well as in operating conditions. For the latter this is usually not the case. Another alternative is to use a robust photocathode. Until now, Cs₂Te seems to be the best compromise between high QE and long lifetime. It is much less sensitive to oxygen than alkali-antimonide photocathodes, barely sensitive to CO₂, and not affected by CO, N₂ and methane (see Figure 10). In spite of that, when Cs₂Te is exposed to oxygen, the QE decreases as two exponential decays depending on the pressure. First, the QE decreases very fast until the surface is passivated, and then a slower exponential decay sets in [21], [45]. For example, according to Michelato [46], an oxygen exposure of 1000 L (1 L = 10⁻⁶ Torr·s) decreases the QE by one order of magnitude. For comparison, alkali-antimonide photocathodes can only withstand 1 L before the QE has dropped by one order of magnitude.

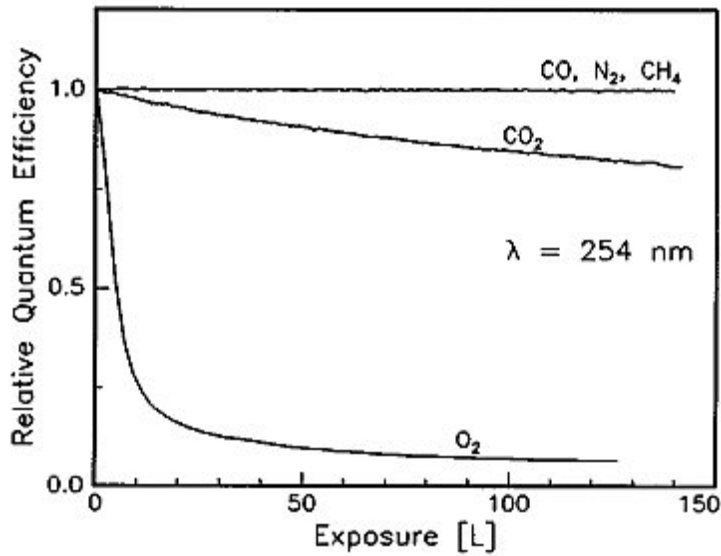


Figure 10: Normalised QE of Cs_2Te exposed to different gases. 1 L (langmuirs) is 10^{-6} Torr·s.

A solution to increase the lifetime is to protect the photocathode with a solid film against degradation from contamination. It was shown that K_2CsSb photocathodes could be protected with a CsBr layer. LANL [38] and CERN [39] have tested this protection layer on Cs_2Te . The former group applied a 4 nm film on a Cs_2Te photocathode and found that it became much more rugged. The initial QE decreased from 10% to 5-6%, but remained unchanged for more than 2 months of operation without any sign of degradation, which must be compared to the 100 hours operational lifetime of pure Cs_2Te photocathodes. A thicker film of CsBr should decrease the QE further but also making it more stable. At CERN a coating of 2 nm CsBr was evaporated upon a Cs_2Te photocathode having an initial QE of 4.3%. It decreased to 1.2%, though without improving the storage lifetime. It could be that the applied layer was still too thin. However, the preparation of an extra layer complicates the preparation process.

Another solution to overcome the reduced QE and lifetime of Cs_2Te photocathodes due to contamination is partial rejuvenation [21]. Furthermore, rejuvenated photocathodes are less affected by exposure to air. There seem to be two procedures of rejuvenation. First, at LANL Cs_2Te photocathodes have been rejuvenated by heating them to 150-200 °C, which restores the QE to about 60% of its initial value. Van Oerle et al. from UT-LF could also rejuvenate photocathodes to about 60% of its initial QE by heating them to 200 °C ([51], see page 49). These experiences indicate a redistribution of Cs by means of diffusion. Second, at INF Milano, irradiation with UV light during heating at 230 °C is necessary to rejuvenate contaminated photocathodes. No rejuvenation was observed without illumination. They could restore the QE to about 30% of the initial value. Di Bona et al. showed that only photocathodes that were prepared until a maximum photocurrent during Cs deposition was reached, could be rejuvenated. Also at the Fermi Lab the photocathode is simultaneously heated to 230 °C and irradiated with UV light [22], [45].

CERN also investigated the properties of Cs₂Te photocathodes when Cs and Te were co-evaporated. The QE and lifetime were improved in a DC gun, where the pressure was reasonably low, but these photocathodes seemed more sensitive to the vacuum quality [23]. Such cathodes showed no better behaviour in the RF gun [56].

3.4. Performances of Cs₂Te photocathodes

Taking into account the parameters mentioned before, the performances of Cs₂Te photocathodes at the several laboratories (SEL, INF, FERMI, LANL, CERN, UT-LF) where Cs₂Te is prepared and tested, differ to a larger extent than could be expected. To demonstrate this, the operational performances are reviewed in this paragraph. It shows that the lifetime depends on maximum field strength, vacuum and especially extracted charge [39]. The operational lifetime of the photocathodes is defined as the time that the QE remains larger than 1%. The average load on the photocathodes and its effect on lifetimes are difficult to determine since the total extracted charge is usually not reported.

The Cs₂Te photocathodes made at INF have been transported to DESY and tested in the TTF injector RF gun. The fourth harmonic of a Nd:YLF laser (263 nm) illuminated the photocathodes with 7 ps pulses. A maximum charge of 50 nC per electron bunch was extracted in a 50 MV/m RF field. The operational lifetime of these photocathodes was several months [18].

At FERMI, the lifetime of the photocathodes was in the order of a month in which the QE drops from initially 10 % at 263 nm to less than 1 %. The maximum extracted charge was 30 nC for a single bunch and 15 nC per bunch for a train of 9 bunches [22].

At LANL, Cs₂Te photocathodes have been used for the Advanced FEL and the RAFEL to lase at 5-6 μm and 16.3 μm respectively [17], [38], [44]. A Nd:YLF laser with a 263 nm wavelength and a pulse length of 7.7 ps was used to illuminate the photocathode, operating in a 20 MV/m RF field at pressures of 10⁻¹⁰ to 10⁻⁹ Torr. The QE, initially at 8-12 % for 263 nm, decreased and stabilised to a value of 3-5 % while operating in the linac. This value was maintained for 100 hours of operation without significant loss. The operational lifetime of these Cs₂Te photocathodes is therefore well beyond 100 hours. A 2 nC electron beam was extracted with a beam energy of 16 MeV, pulse lengths of 7 to 14 ps, a negligible dark current and an emittance comparable to that of K₂CsSb. For the RAFEL 4.5 nC was extracted from a Cs₂Te photocathode containing a CsBr protection layer.

At CERN the lifetime was 1-2 weeks⁶ [39], [48]. An electron beam of 48 bunches, each with a charge of 13.4 nC, could be extracted at a 100 MV/m RF field [27].

⁶ <http://ucq.home.cern.ch/ucq/Photocathodes.htm>

The operational lifetimes of Cs₂Te photocathodes in the setup at UT-LF are considerably shorter in comparison with other groups, and in comparison with their own storage lifetimes. The initial QE of 12 % at 263 nm decreases very fast resulting in operational lifetimes of about 11 hours [51].

Volokhine [55] found that there is a difference between photocathodes that have been operated under low peak current conditions (< 150 A) and high peak current conditions (> 150 A). In case of low current operation, the QE degrades gradually over several hours and no clear visual changes of the surface were observed. Adding a new Cs layer on top of the existing one restored the QE to almost the initial value. When high currents were extracted by applying higher laser intensities, the QE dropped to a level below 1% in a few tens of minutes. The contour of the drive laser spot was clearly ‘printed’ on the surface of the photocathode and the QE of this area was practically zero. It is unknown whether this effect is due to ablation or that structural changes have occurred induced by the laser. The QE outside the contour had not decreased so much, indicating that contamination is not the main reason for degradation of these photocathodes operating under high currents. Back bombardment of ions from the linac (linear accelerator) is also unlikely by the same arguments.

The photocathodes made by Volokhine showed different photocurrent behaviour during preparation than the photocathodes made by Van Oerle. The latter obtained photocathodes with QE of about 12% while Volokhine typically prepared photocathodes with initial QE’s of 4-8%. Our recently prepared photocathodes have higher QE’s of 16-21% (at 254 nm). The time of maximum photocurrent during Cs deposition is also different (usually a few minutes).

The latter results from the UT-LF group shows that even with the same setup, three different photocathodes have been prepared while most parameters are believed to be the same. Between the various research groups, the differences are even larger. Therefore, the parameters mentioned in paragraph 3.3 cannot account solely for these differences. We conclude that the preparation conditions are of main importance for the performances of the photocathodes. In the next paragraph, we consider the preparation processes in more detail.

3.5. Preparation conditions of Cs₂Te photocathodes

The general preparation procedure of Cs₂Te photocathodes is evaporation of subsequently Te and Cs, onto a metallic substratum at an elevated temperature ([4], see page 179). However, the preparation processes differ slightly from each other at the various laboratories to enable a detailed comparison. In the following paragraphs, a summary is given of the preparation of Cs₂Te at these laboratories. We have limited our survey to Mo substrata only, because this is the best and most used substratum. An overview of the preparation conditions is given in Table 1.

Laboratory	Te	Cs deposition stopped	T sub (°C)	P max (Torr)	QE	λ	Operational lifetime
SEL	120 nm	50% of maximum QE	150	10^{-7}	~12-17%	270-250	
INF	10 nm (1nm/min)	70-80 min (max QE) (1nm/min)	120	10^{-9}	8-13%	254	~ months
Fermi	10 min (1nm/min)	60-120 min (1nm/min)	120	$1-4 \cdot 10^{-9}$	12%	254	~ months
LANL	10-30 nm	80-90% of max QE	100-110	few 10^{-9}	15-18%	251	> 100 h
CERN	10 nm	15 nm (max QE) (80 min)	110		4-7%; 16%	262	1-2 weeks
UT-LF	25-30 min	2-15 min (max QE)	120	low 10^{-8}	12%; 4-8%; 16-21%	254	11 h; few minutes

Table 1: Preparation conditions of several laboratories

3.5.1. Stanford Electronics Laboratories

As discussed in paragraph 3.1 Powell et al. of SEL investigated the band structure and optical properties of Cs₂Te photocathodes [3], [43]. They first vapour deposited a 120 nm thick polycrystalline Te layer on a heat-cleaned polished Mo substratum, held at room temperature. (The pressure in the chamber stayed below 10^{-9} Torr). Next, the temperature of the substratum was set to 150 °C and the deposition of Cs started, which was controlled via heating of a side arm of the preparation chamber containing Cs vapour (99.98% pure). The Cs vapour pressure in the main chamber was maintained at 10^{-7} Torr. The photocurrent, monitored with an Hg arc lamp, increased from 0.1 nA to a maximum of 300 nA and decreased with further exposure to Cs. The cesiation was stopped when the photocurrent fell to half of the maximum value. Afterwards, the photocurrent rose gradually to its maximum value. Subsequent annealing at 150 °C for 1 hour and slow cooling completed the preparation process that results in a pale greenish yellow Cs₂Te film. The spectral response is given in Figure 3A.

3.5.2. Istituto Nazionale di Fisica

At INF, Cs₂Te photocathodes were prepared for transport to DESY, Hamburg to be tested under operational conditions in the TTF injector RF gun [18], [19], [45], [46], [54]. At FERMI the same preparation techniques were used in situ [22]. The preparation in Milano was performed on a Mo foil of 1 mm thickness, which was mechanically polished with 1 μ m diamond powder and then rinsed with acetone and ethanol [45] or with 50 nm diamond grinding powder [18]. The substratum was heated to 500 °C for 30 minutes for additional surface cleaning, whereby the pressure did not exceed $1 \cdot 10^{-9}$ Torr. A residual oxidised layer still remained. During evaporation of subsequently Te and Cs the substratum was kept at 120 °C. The Te and Cs sources were Ni boats filled with respectively 99.999% Te powder and a mixture of Cs₂CrO₄ and 84% Zr-16% Al, that were resistively heated by a current flow. First, 10 nm Te was deposited on the substratum. Then Cs was evaporated at a rate of 1 nm/min and monitored by measuring the photocurrent with an Hg lamp (254 nm). At maximum QE the deposition is stopped, which is usually after about 70-80 minutes. In Figure 5 and Figure 9, the QE behaviour

during evaporation of Cs is given. The substratum was cooled down to room temperature before use in the RF gun. The resulting QE was about 8 to 13 %.

3.5.3. Fermi National Accelerator Laboratory

At FERMI [22] the sources containing Te and Cs were degassed prior to coating. The Mo cathode is heated to 350 °C with a halogen lamp for 30 to 60 minutes to clean the surface from contaminants. During evaporation of Te and Cs the cathode was held at 120 °C and the photocurrent is monitored with a mercury lamp (254 nm line). Te was deposited for 10 minutes at a rate of 1 nm/min. Cs was deposited for 60 to 120 minutes at the same rate. The photocathode coloured orange when Cs is deposited for 63 minutes. 110 minutes of Cs deposition resulted in a blue photocathode. The photocurrent during deposition as a function of time for the latter photocathode is given in Figure 11. The maximum pressure was between 1 to $4 \cdot 10^{-9}$ Torr. After Cs deposition was stopped, the photocurrent increased. The QE is about 12 %.

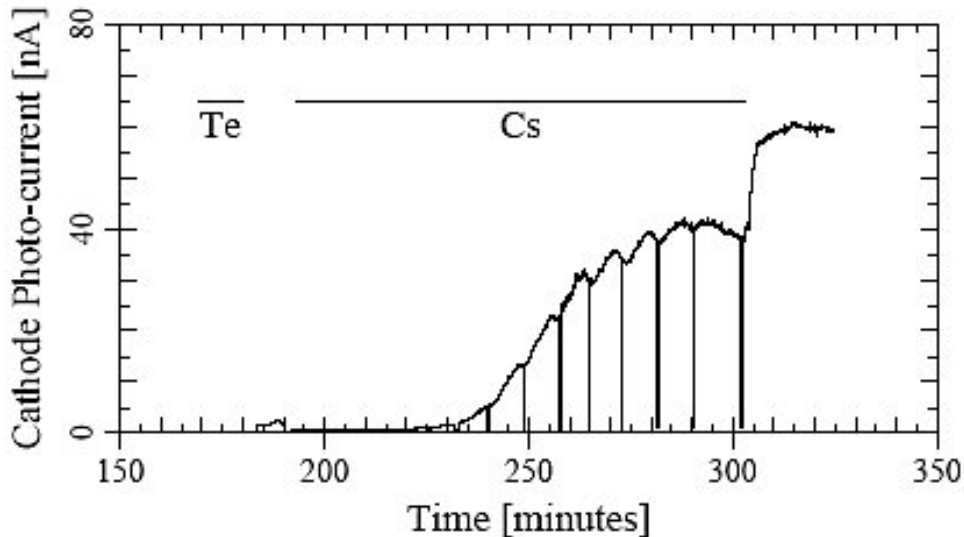


Figure 11: Typical progress of the measured photocurrent during a preparation procedure of Cs_2Te at Fermi. The downward spikes correspond to blocking of the UV light to measure the background current.

3.5.4. Los Alamos National Laboratory

LANL used a Mo plug as substratum which was cleaned by heating it to 300 °C before depositing Cs_2Te [21], [44]. The Te source consisted of a small Mo can of 99.9999% pure Te pieces and was heated by thermocoax heater wires wound around the can. The Cs source was a similar can with a powder mixture of Cs chromate and Ti. The sources were positioned at an angle of 10° from normal. First, a Te film of 10-30 nm was evaporated onto the Mo substratum that was maintained between 100-110 °C. The deposition of Cs was stopped after the QE has dropped to 80-90 % of its maximum, monitored at 251 nm. The pressure never went above a few 10^{-9} Torr. After the Cs deposition, the photocurrent rised to near its maximum value. The evaporation rate and the amount of evaporated Cs

are unknown. The total fabrication time was about one hour, so Cs was deposited in much less time compared to INF and FERMI. Typical QE's are 15-18%. Some photocathodes were heated to about 170 °C after the deposition was finished, to remove any free Cs from the surface. This was only necessary when fabricating near room temperature.

3.5.5. *Centre Européen pour la Recherche Nucleaire*

At CERN Cs₂Te photocathodes were prepared for the CLIC Test Facility (CTF) [23]. They used mainly Cu substrata for the CTF2 and Au-Cu for the CTF3 [52]. The cathode plug was cleaned by Ar⁺ bombardment. 10 nm Te was deposited on the substratum that was at room temperature [27]. The substratum was held at 110 °C during the deposition of Cs, which was stopped at maximum photoemission (about 15 nm Cs). A typical QE of 5-10% was obtained. The Cs-to-Te ratio is about 0.35, which is far less than the expected ratio of 2. Since Te interacts strongly with Cu, not all of the Te is available for the reaction with subsequently evaporated Cs. If the surface is rough, more Cu can react for the Cu-Te compound. Although INF showed that Cs₂Te on a Mo cathode has better performances than on a Cu, nevertheless, both substrata showed the same behaviour at CERN [48], and had almost the same Cs-to-Te ratio. Another proposed reason is that Cs₂Te₅ is catalytically formed instead of Cs₂Te [39].

3.5.6. *Research Center Rossendorf*

At Rossendorf, a Cs₂Te photocathode was used in a superconducting RF gun. The QE was only 0.25% [23].

3.5.7. *University of Twente*

The above-mentioned conditions at the other groups differ from our conditions at the University of Twente (UT-LF) [29], indicating that the formation of Cs₂Te proceeds on a different way. Generally, we have short preparation times (within one hour), just like LANL. At UT-LF, we use a Mo cathode that is cleaned from previous Cs₂Te films by heating it at 600 °C for several hours. During preparation of a new film, the temperature is kept at 120 °C. The Te and Cs sources are Mo cans with respectively 99.999% Te pieces and Cs chromate, which are resistively heated and can be positioned in front of the cathode separately with an actuator (Figure 12). It contains two similar Te and two similar Cs sources.

The pressure inside the preparation chamber is monitored during the whole deposition process and the photocurrent is measured during the evaporation of Cs on the Te layer, with aid of a mercury lamp and a 254 nm filter. The UV power is variable between 1.4 and 30 μW. The sources are first heated to the correct temperature before being placed in front of the cathode. The set temperature of the Te source is 305 °C and of the Cs chromate is 580 °C. The deposition of Te takes 25 to 30 minutes. Cs is deposited until a maximum photocurrent is observed, which is usually after a few up to fifteen minutes. The sources are removed to cool down away from the cathode.

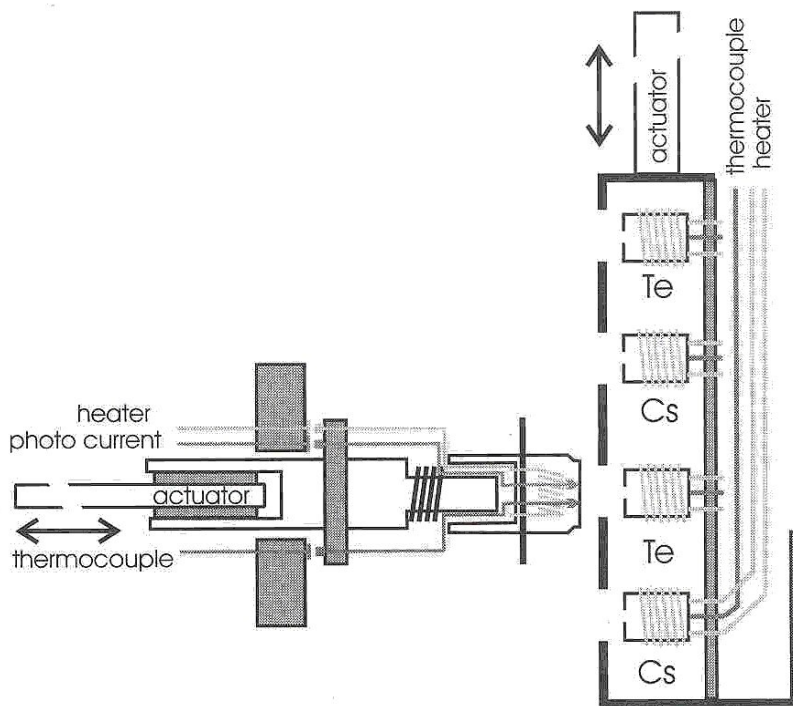


Figure 12: Mechanical layout of the photocathode preparation chamber.

Several curves of the typical photocurrent response as function of Cs evaporation time can be seen in Figure 13. In these cases the Cs deposition has been prolonged after the maximum photocurrent was reached for illustrating purposes. One can see that a general feature of the photocurrent is a gradual drop of the QE after some initial maximum, followed by a saturation to a slightly lower value. When the source is removed, the QE immediately rises (within a few seconds) to a level close to the maximum value. The final value is lower when the cathode is at a lower temperature. This sudden rise of photocurrent was seen at SEL, FERMI, LANL and UT-LF. When the Cs source is not removed but allowed to cool down in front of the cathode, the photocurrent rises gradually to the same value.

The most apparent observation from Figure 13 is that the temporal behaviour of the photocurrent follows a number of clearly different time scales, although the measurements and preparations were performed under seemingly identical conditions, which is 25 minutes of Te deposition at 305 °C and Cs deposition at 580 °C (except for the orange curve that had a Cs temperature of 550 °C). For an unknown reason, the red and orange curves (and other similar curves, which are not plotted) show small deposition times before the maximum photocurrent was reached, while the green, light blue and dark blue curves show larger deposition times. Furthermore, the time of saturation to a lower level also increases with deposition time. The preparation of the Cs-Te photocathodes of the former curves has been performed with the other Cs source than the latter curves. Most likely, the second Cs source has smaller deposition rates. As a possible reason for the observed irreproducibility in deposition times to a maximum QE, we suspect that the residual background pressure in the vacuum chamber might play a role. For example, we observed that the pressure is not constant (between $1 \cdot 10^{-9}$ and $1.5 \cdot 10^{-8}$ Torr).

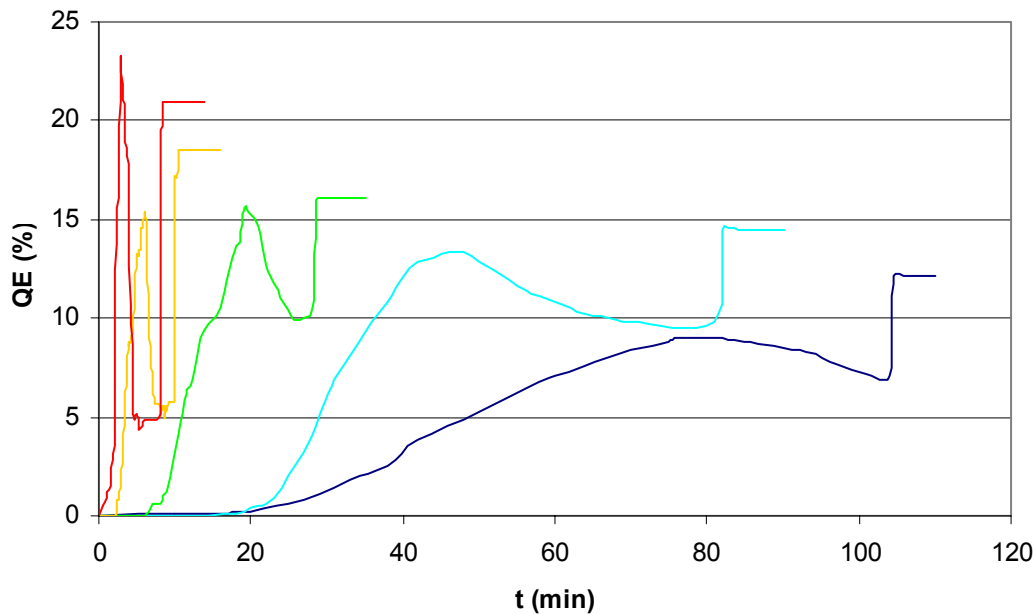


Figure 13: QE (photocurrent), measured by a 254 nm mercury lamp, as function of the Cs deposition time for several photocathodes. Small oscillations on the curves due to fluctuations in the power of the mercury lamp have been averaged out. The photocurrent starts to increase after a certain time of Cs evaporation. We prolonged the Cs deposition after the maximum has been reached for all curves, and the photocurrent decreases. When we removed the Cs source, the current rises immediately. The orange, light blue and dark blue curves were measured with a larger UV spot than the red and the green curves, which was partially blocked during deposition. Therefore, the measured QE values during deposition are smaller than that of the final QE values after the source is removed.

Yet, an interesting relation between the QE and the deposition time is observable for the produced photocathodes. The final QE is plotted in Figure 14 as a function of the time of maximum photocurrent. One can see that if this time is longer, the QE is lower. The photocathodes that are prepared with a few minutes of Cs deposition have QE's higher than 20 %. The photocathode with maximum photocurrent after 80 minutes has a QE of 12 %, which is the same value that was obtained at INF for photocathodes prepared with 70-80 minutes of Cs deposition. No correlation could be found between the QE and the total value of the measured background pressure. Nevertheless, it might be interesting to further analyse this background pressure, e.g. with a mass spectrometer, to search for correlations of the QE with the partial pressure of a particular gas.

We conclude that the deposition rate of Cs is smaller for a low QE photocathode, because the preparation time is longer. However, if the smaller deposition rate would only affect the preparation time, we would expect that the final QE does not change. Thus, it is suggested that in addition different stoichiometric compounds of Cs-Te are formed (different ratio between Cs and Te), with different properties.

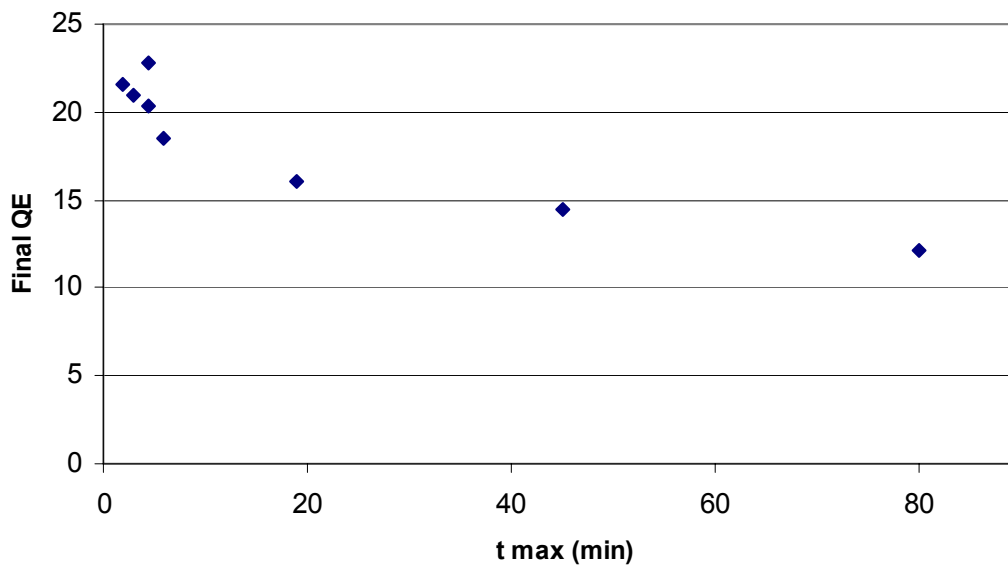


Figure 14: QE versus time of maximum photocurrent. A shorter time results in a higher QE.

3.6. Conclusions and new model

From the above-mentioned data we come to the conclusion that the spread in performances of Cs₂Te photocathodes is not only due to the substratum properties and contaminations but that it mainly can be ascribed to the stoichiometry which largely depends on the preparation process. The preparation procedures of Cs₂Te photocathodes and their photocurrent behaviour seem to differ a lot between the several groups, as well as their performances during operational conditions. Since the properties of the substratum determine to a great extent the properties of the deposited Cs₂Te photocathode, it is not possible to make direct comparisons between our photocathodes and the ones on a Cu substratum produced by CERN. A comparison has been made for photocathodes prepared on Mo substrata, since they result in the best photocathodes. From that, we can conclude that:

INF produces the most robust photocathodes with the longest lifetimes and the highest extracted electron current. FERMI has comparable photocathodes. INF and FERMI have the longest preparation procedures but also lower QE's compared to LANL and UT-LF. Although the QE is lower, higher charges can be extracted. The photocathodes prepared at LANL seem to be the most alike to our photocathodes. The preparation time is shorter, the QE is higher, but the lifetime is shorter and the extractable charge is less. There seems to be a discrepancy between optimal QE with shortest preparation time versus optimal lifetime and maximum extractable charge. This relation actually is observed for photocathodes at UT-LF. This supports the following assumption:

We believe that the formation of Cs-Te photocathodes is slightly more complicated than what is commonly reported: When Cs is deposited on Te, some Cs atoms diffuse into the Te layer and react with Te atoms to form a Cs-Te compound. The desired reaction is $\text{Te}_{(s)} + 2\text{Cs}_{(g)} \rightarrow \text{Cs}_2\text{Te}_{(s)}$. However, many stable Cs-Te compounds exist: Cs₃Te₂, Cs₂Te₃, Cs₂Te₅, CsTe₄, Cs₅Te₄ and CsTe

[48], which may form under dissimilar conditions. Which stoichiometric compound forms, may depend on the particular favoured energetic situation. The rate of chemical reactions and diffusion of atoms into a layer critically depends on the temperature of the substratum and the chemicals, the concentration of the reacting materials and the degree of distribution of a solid material (crystalline or amorphous, smooth or rough surface). The concentration is influenced by the thickness of the first layer, the evaporation rate and flow of the second material upon the sample and the pressure. The heat conductivity of the holder and the dispenser material for Cs determine the energy and temperature of the atoms (e.g. a mixture of Cs chromate with 84% Zr-16% Al requires a different temperature than a mixture of Cs chromate and Ti to obtain the same Cs evaporation rate).

3.6.1. Propositions

Our hypothetical perception of the preparation process is that one favourable stoichiometric Cs-Te compound (out of the various possible stoichiometric compounds) starts to form and grow when Cs atoms diffuse into the Te layer, depending on the preparation conditions. This stoichiometric Cs-Te can be Cs_2Te , $\text{Cs}_{1.2}\text{Te}$ in case of INF or even another Cs_xTe_y compound. This depends on the evaporation rate of Cs and the diffusion (related to the substratum temperature, roughness and the Te thickness and density).

The spectral response and the photocurrent behaviour can be explained in three steps as follows.

First, the amount of one favourable Cs_xTe_y compound grows and so after some time the photocurrent starts to rise, until a spectral response is obtained with a very sharp threshold like curve A in Figure 3. At this point, the most advantageous, possibly homogeneous, proportion of the Cs_xTe_y compound is formed throughout the layer. It can be expected that the maximum QE will be slightly different for the various types of stoichiometric compounds besides the influence of thickness and substratum parameters.

Secondly, if the Cs deposition is continued, Cs atoms can no longer diffuse far into the layer because of the bonds between the Cs and Te, but remain preferably at the surface. We suspect that from this a second compound forms with relatively more Cs atoms than the first phase. This second compound was entitled by Taft and Apker as 'excess' Cs, stated by Sommer as 'excess' Cs bound in an energetically very stable configuration and described by Spicer as being another phase of Cs-Te, which was noticed by Di Bona as being $\text{Cs}_{x>2}\text{Te}$ at the surface with a thickness of 0.5 nm. We believe as well that this compound may have a different stoichiometry. However, we believe these compounds are induced by different preparation conditions. Furthermore, with the growth of the second compound, the typical spectral shoulder starts to appear in the spectral response. With further Cs deposition, this new phase grows, while the photocurrent still increases (and thus the QE) until it reaches its maximum like curve B in Figure 3. At this point, the growth of the second phase is completed. The maximum QE will again attain a different value for yet a different stoichiometry. Until now, usually the preparation process was stopped and the resulting photocathode was called ' Cs_2Te '.

Thirdly, any prolonged Cs deposition (after the maximum QE) will result in undesirable abundant Cs that covers the Cs-Te photocathode with a resulting decrease in photocurrent. The QE and the shoulder reduce. This can be explained on the basis of the Cs deposition rate. We believe that after the maximum QE has been reached, abundant Cs will be deposited that cannot bind with other Cs or Te atoms and thus sticks weakly to the surface. There is now a flux of incoming Cs atoms by evaporation and a flux of Cs atoms coming loose from the surface because of the (high) temperature of the sample. Eventually, equilibrium sets in with a saturation of photocurrent as result, depending on the magnitude of these fluxes. The saturation is a passivation of the surface by Cs atoms. If now the Cs source is pulled away, the weakly sticking Cs atoms can easily be removed from the surface and the photocurrent rises rapidly. If the source is turned off and simply cools down in front of the photocathode, the incoming flux decreases gradually and the abundant Cs slowly disappears from the surface, resulting in a photocurrent that rises slowly, eventually to near its maximum. If however, the substratum has cooled down (rapidly) before the source is removed, not all the weakly sticking Cs atoms can be removed from the surface and a lower final photocurrent is obtained. This explains the rise of photocurrent after removing the Cs source, described on page 30.

The second hypothesis is that the stoichiometry that results in the highest QE has the worst (temporal) stability. This is a general trend seen for the Cs-Te photocathodes, even for photocathodes in general. Furthermore, we state that the most stable photocathode can be produced at the point when the first compound has formed with a sharp spectral response like curve A in Figure 3. The second compound at the surface with extra Cs atoms reduces the lifetime of photocathodes. Maximum QE occurs at maximum saturation of $Cs_{x>2}Te$. However, it is expected that because of the large amount of Cs, that is very sensitive to oxygen, more oxygen can be bound and a faster decrease in QE is the result. Usually, the preparation of Cs-Te photocathodes is stopped after step 2 or during step 3. Thus, the best photocathode would be achieved after step 1. We expect that this will result in the most stable photocathode, however, the QE is lower than after step 2.

3.6.2. Explanations

These hypotheses can explain some properties and behaviours of the Cs_2Te photocathodes that were not yet fully understood. These following examples further support the idea that stoichiometrically stable different Cs-Te photocathodes can coexist.

First, we give an explanation for the difference between the ‘cold’ and ‘warm’ approach, as discussed in paragraph 3.3.2. Assume a given Te layer thickness and a fixed Cs evaporation rate. There exists a substratum temperature for which the diffusion of Cs atoms into the Te layer is optimal and the desired reaction between Cs and Te takes place so that Cs_2Te is formed. Suppose now that during both the ‘cold’ and ‘warm’ approach, the same stoichiometric Cs_2Te is formed. In case of the ‘cold’ approach, the diffusion may be small(er) and only at the surface the desired Cs_2Te film is formed. The time needed for Cs deposition should be less,

which is also observed experimentally. However, the optimal thickness of Cs₂Te photocathodes was determined to be around 65 nm (see paragraph 3.3.1). Any thinner film will give a lower QE. This is in contradiction with the observed higher QE. Consequently, it is not plausible that the same stoichiometric compound forms in both approaches.

Alternatively, because of the lower temperature in the ‘cold’ approach, the diffusion is smaller, so the amount of Te that can react is less. With the same Cs evaporation rate, an abundance of Cs atoms evolves, and so the reacting concentrations are different compared to the warm approach. Both the altered temperature and concentration will alter the reaction speed and the energetic equilibrium. Therefore, it is most likely that another stoichiometric Cs-Te compound starts to form than in the ‘warm’ approach. The initially favoured stoichiometry results in a higher QE photocathode, but may also have a higher affinity to contaminations. In addition, the very thin layer may further decrease the temporal stability and lifetime. The lower stability of the ‘cold’ preparation process is also explained by this mechanism. For example, during operation, the laser may stimulate the diffusion process of Cs from the top layer to deeper layers, lowering the QE in a short time. We suspect that in the cold preparation process, metastable states form due to sticking of atoms in local potential minima. This is not the case in the warm process, where their additional kinetic energy overcomes the settling of the atoms. From the fact that a substratum temperature of 120 °C is enough to induce a distinction between the two processes, indicates that the local energy minima are small (less than $\frac{1}{2}kT = 17$ meV), and that the bonds between Cs and Te atoms in the cold approach are weak.

Another incomprehensible property of Cs-Te photocathodes is the observed variety of different rejuvenation processes. As said before, the preparation, performances and behaviour of Cs-Te photocathodes from INF and FERMI are comparable with each other and that of LANL seems comparable with UT-LF. This distinction is also seen in the rejuvenation processes. Contaminated photocathodes from INF and FERMI require simultaneously heating and irradiating with UV light to recover the QE. At LANL and UT-LF only heating is necessary and the restored QE is even higher (60% instead of 30%).

A possible explanation of this difference is as follows: the photocathodes with higher initial QE are more sensitive to contamination, but the bonds may be weaker than in the more robust Cs-Te photocathodes, with the result that it is easier to remove the contaminants (only heating is sufficient). Indeed, the recovered photocathode was found to be more rugged. It could even be that the contaminated upper layer is completely removed resulting in a photocathode that is comparable with the one completed after the above-mentioned first step (curve A in Figure 3). However, once a more robust photocathode is polluted, the contamination is more severe and thus more difficult to remove. UV light may have a kind of catalytic effect on the desorption and is only required for the more rugged stoichiometric compounds. In conclusion, we claim that the stoichiometry resulting in higher QE photocathodes are more sensitive to contaminations but can easier be rejuvenated, and that the more rugged photocathodes are more difficult to recover. Further, we assume that photocathodes with a sharp threshold, which we claimed before to be the most stable ones, may be even impossible to

rejuvenate after they have been contaminated. This assumption is supported by the observation of Di Bona, who found that no rejuvenation was possible on prepared photocathodes, where the Cs deposition was stopped before the maximum photocurrent was reached. They could only rejuvenate photocathodes that are prepared to maximum photocurrent. Apparently, the excess Cs acts as a kind of buffer to fill vacancies that resulted from diffusion or from Cs that was bound by contaminants.

Another example is the co-evaporated Cs-Te photocathodes of CERN, which apparently results in a single stoichiometric Cs-Te compound that has a high initial QE, but again is more sensitive to contamination.

In summary we conclude that the preparation procedure strongly determines the performances of Cs-Te photocathodes. In particular, a smaller Cs deposition rate results in photocathodes with a longer lifetime, because they are more robust against degradation due to contamination or due to high average beam load (extracted current), but with a slightly smaller QE. In addition, we conclude that different stoichiometric compounds form when the preparation conditions are altered.

Some means of diagnostics has to be considered in order to inspect which stoichiometric compound forms under what preparation conditions and at what time to what thickness. Having such means would, finally, enable to adjust the preparation conditions such that any desirable Cs-Te compound can be obtained. This monitoring needs to be more specific than just measuring the total photocurrent and be non-destructive and compatible with the existing preparation chamber. Therefore, we have to compare different diagnostic techniques and select the most suitable method that fulfills these requirements. This will be discussed in the next chapter.

4. Diagnostics

4.1. Introduction

In the previous chapter, we gave an overview on what data several other groups have reported on Cs₂Te like quantum efficiency, lifetime and deposition method. We suggested the coexistence of different stoichiometries. Therefore, we require more information about the Cs₂Te films, to understand the deposition process of Cs₂Te, to verify the proposed model, and to have a better control during the preparation process. Until now, the only feedback is monitoring the QE during evaporation of cesium.

There exist various analysing techniques to characterise thin films by their physical properties like the refractive index, thickness, roughness, morphology, chemical composition or electrical and magnetic properties [57], [58]. These techniques can be differentiated between destructive and non-destructive, in-situ or ex-situ, and real-time or post-growth monitoring and characterising techniques. Since one needs a properly working photocathode after deposition and analysis, non-destructive methods are of main interest. These are optical methods, scanning probe techniques and various types of electron spectroscopy. A relatively low cost, real-time and in-situ analysis method is preferred.

Scanning probe techniques and techniques that use electrons or other particles as incoming or outgoing beams for analysis are impractical to implement in the present preparation chamber as these particles are mostly charged and this requires a well defined electric field distribution in the chamber. Furthermore, it is no option to remove the photocathode out of the vacuum chamber to analyse it after growth with an external setup, because it takes several weeks to get the system to UHV conditions after opening the chamber. Above all, the photocathode will be contaminated immediately due to exposure to air. So only an optical setup meets the requirements.

Several optical techniques exist like ellipsometry, X-ray reflectometry, infrared spectroscopy and Raman spectroscopy. With infrared spectroscopy, it is possible to determine optical properties, microstructure, chemical elements and morphology. However, this technique is quite expensive and cumbersome to operate. The same holds for X-ray-based analysing techniques like X-ray Photoelectron Spectroscopy (XPS), although it is very useful to obtain chemical information of the film like stoichiometry and contamination. Raman spectroscopy can be used to determine morphology, but not to obtain information about optical properties and thickness or roughness.

We have decided to apply ellipsometry for its conceptual simplicity and its ease of implementation. Ellipsometry measures the change of amplitude and phase of the polarisation states of polarised light when reflected at non-normal incidence from a film surface [59]. This technique has a very high depth resolution since it does not rely on interference effects (and thus by the wavelength). Usually, thicknesses of less than 0.1 nm to several tens or hundreds of nm are measurable. Spectroscopic Ellipsometry is the most powerful optical technique to determine the layer thickness and optical properties, but is also a very expensive method because it requires a widely tunable light source. For these practical reasons we choose to use Single Wavelength Ellipsometry (SWE), which should give us more

information about relative changes in layer thickness and refractive index during growth. The method can also be used to measure the homogeneity. Since the refractive index depends on the stoichiometry, it should be possible with SWE to discriminate between the growth of different stoichiometric compounds by varying the preparation process.

Although systematic XPS measurements are not practical since to be performed in the existing the preparation chamber, we performed one XPS measurement on a photocathode at the group Material Science of our in order to get some additional information about the structure of the photocathode.

In this chapter, we first present the results of that XPS measurement. Then we describe the basic principle of SWE and the steps we have taken to implement SWE into our existing photocathode preparation chamber.

4.2. X-ray Photoelectron Spectroscopy

For obtaining a Cs-Te photocathode sample for XPS measurements, we inserted a dummy molybdenum substratum in our preparation chamber, on which we deposited a Cs-Te photocathode. The Cs deposition time to maximum photocurrent was 4½ minutes. This photocathode was then removed, transported in nitrogen, and built into the XPS spectrometer⁷ in the group Material Science. In Figure 15 the wide range XPS spectrum is shown. The XPS measurement of Di Bona et al. from INF [45], which shows a part of the spectrum, is given as a reference (Figure 16).

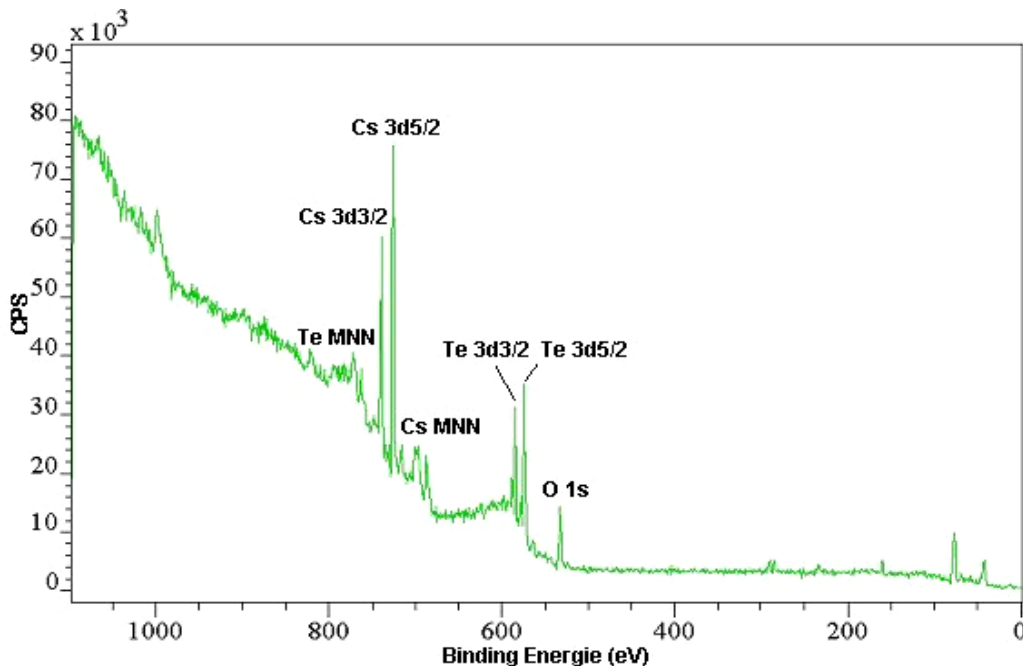


Figure 15: Wide range XPS spectrum of an oxidised Cs-Te photocathode prepared in our system.

⁷ Kratos XSAM-800 XPS system with Omicron E125 hemi-spherical analyzer.

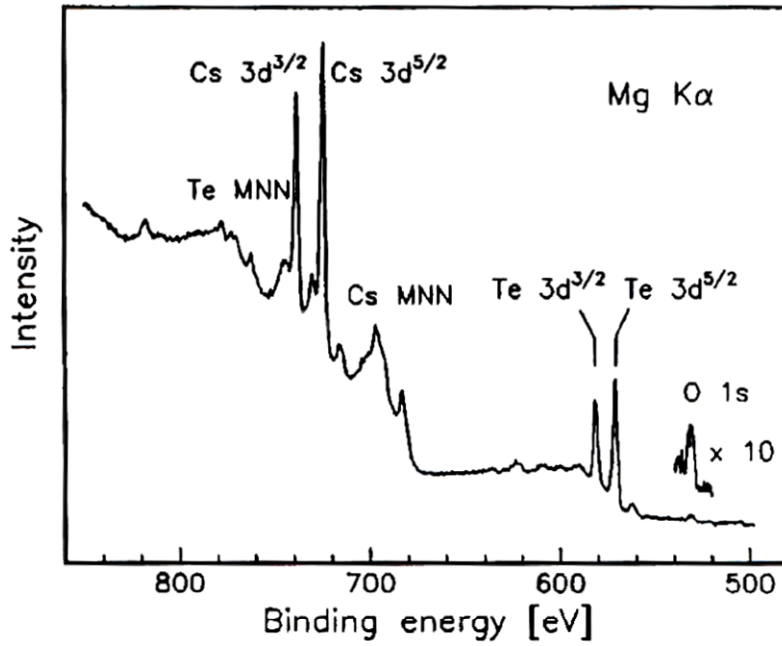


Figure 16: XPS spectrum from Di Bona et al.

In Figure 17 and Figure 18, the Cs 3d and Te 3d peaks of our spectrum are enlarged. As, for transport, the vacuum was broken and the photocathode was briefly exposed to air, one would expect that the photocathode was oxidised before the XPS measurement was performed. This is confirmed by the oxygen peak and small Te peak at around 576 eV, corresponding to Te oxide, which is also present in measurements from Di Bona Figure 19.

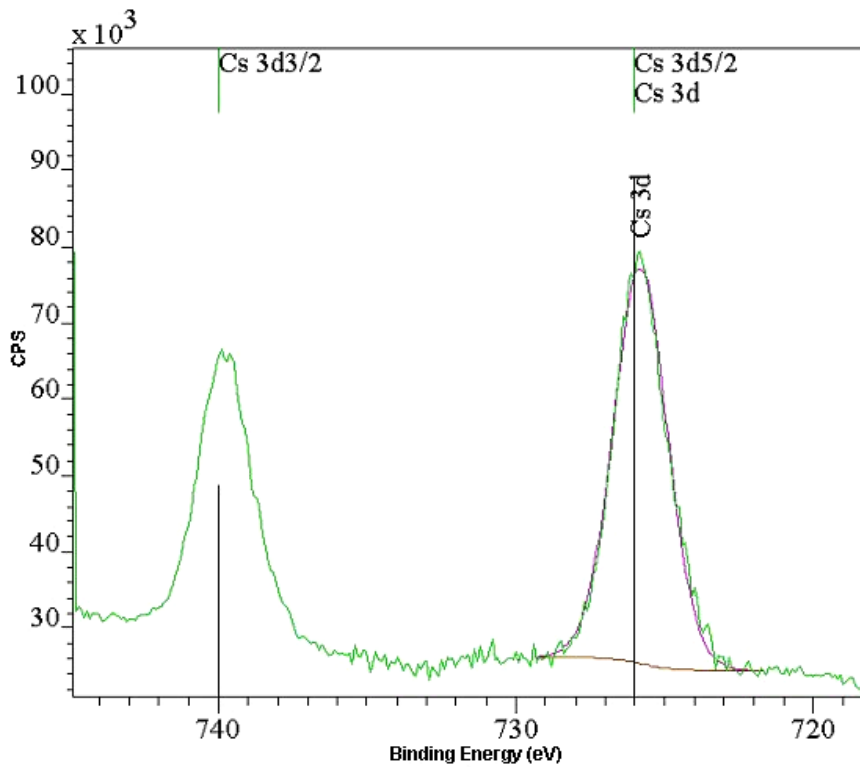


Figure 17: The Cs 3d photoemission line.

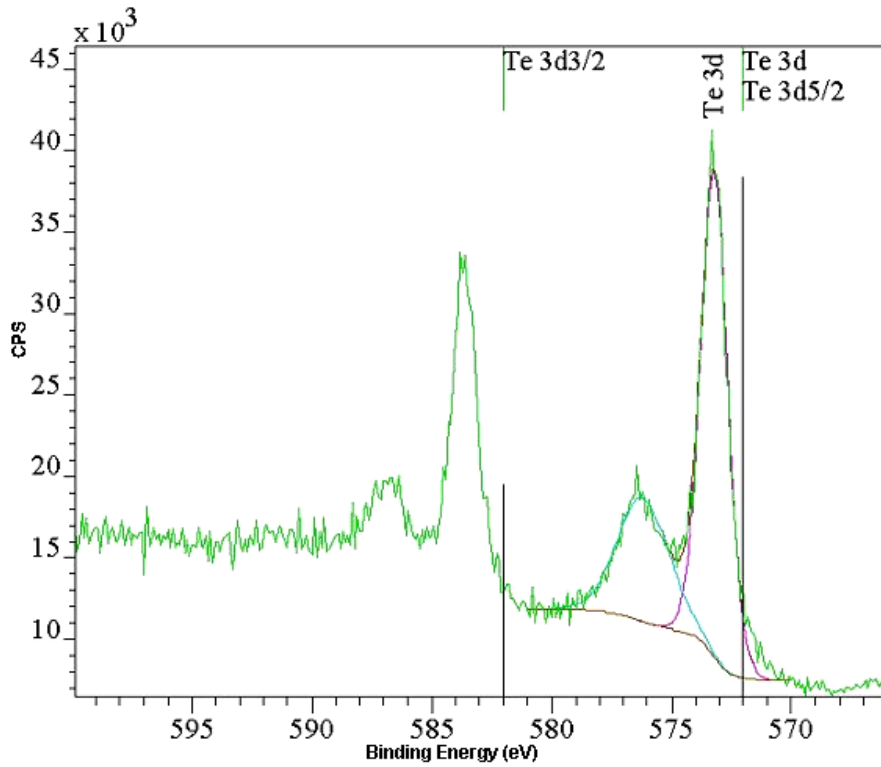


Figure 18: The Te 3d photoemission line.

To convert the signal intensities to atomic fractions, we use the sensitivity factors calculated by Di Bona, which are 4.4 for Cs and 3.8 for Te. Using these factors and the ratios of the areas under the Cs $3d^{5/2}$ and Te $3d^{5/2}$ peaks allows to determine a Cs to Te ratio of 1.6 (including the Te-oxide peak), and a ratio Cs:Te of 2.35 in case the Te-oxide peak is excluded. This latter value seems plausible for a high deposition rate of Cs.

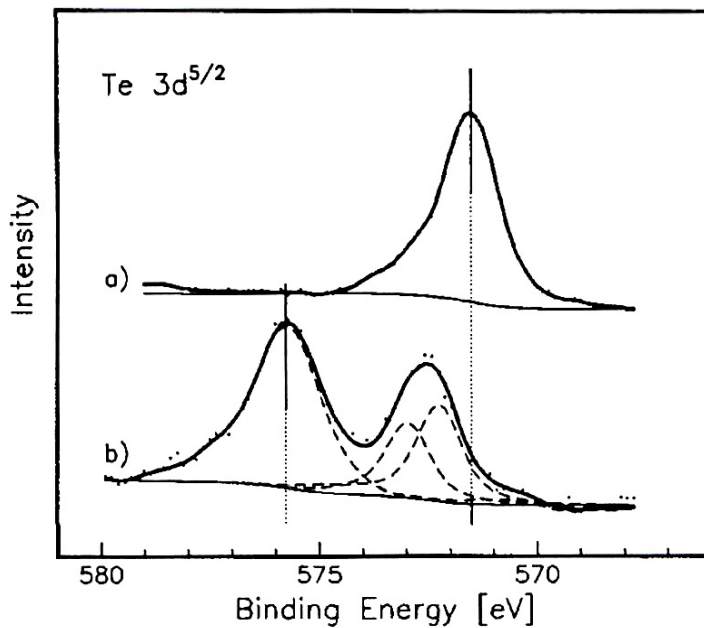


Figure 19: (a) Completed Cs_2Te photocathode. (b) Oxidised photocathode.

The intentionally oxidised photocathode of Di Bona in Figure 19b shows a Te peak at 575.7 eV and two peaks very close together at 572.9 eV and 572.2 eV. These peaks are, respectively, from Tellurium oxide, pure Te and $\text{Cs}_{1.2}\text{Te}$. The latter two are phases that have been observed during the formation of a Cs_2Te photocathode. A more strongly oxidised Cs-Te photocathode will have a higher Te-Ox peak. From our spectrum with a smaller oxidation peak than in Di Bona's spectrum, we can thus conclude that in our case the time of oxidation was shorter. In Figure 20 and Figure 21 Gaussian-Lorentz fits are made of the $\text{Te } 3d^{5/2}$ peak with respectively a single and a double peak.

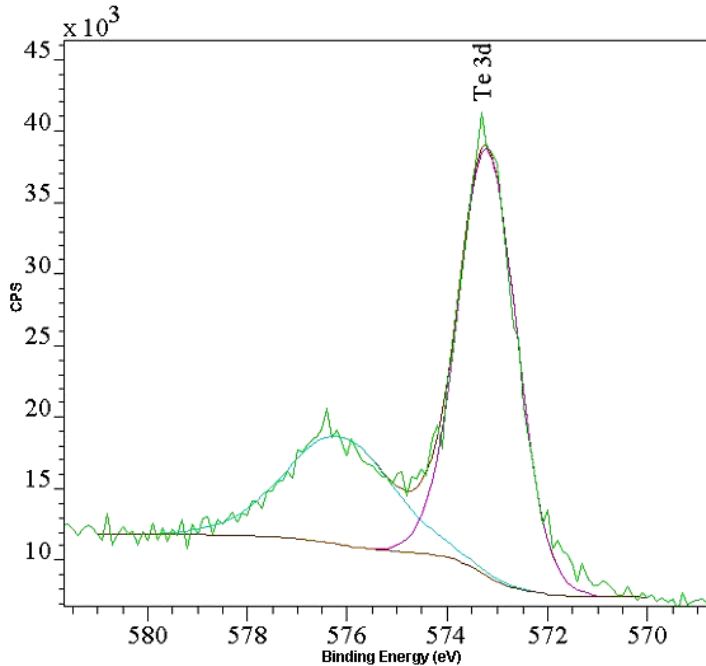


Figure 20: $\text{Te } 3d^{5/2}$ peak with single peak fit.

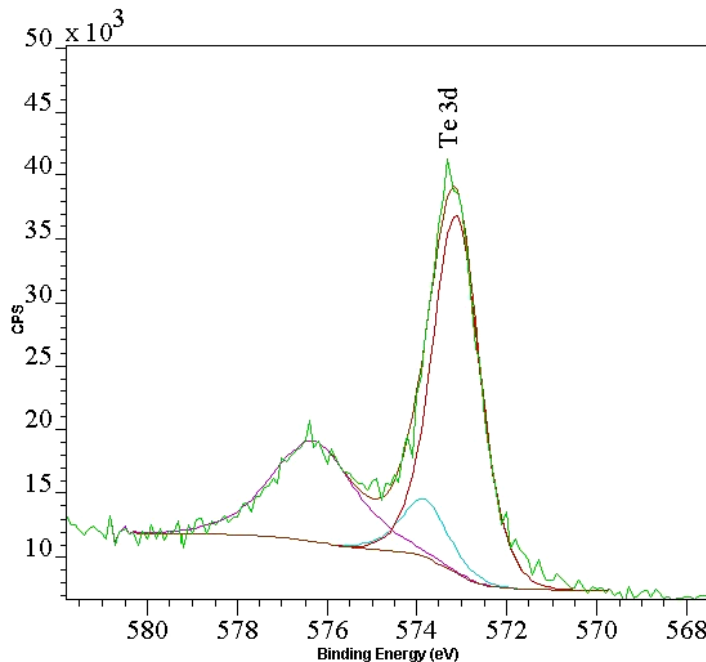


Figure 21: $\text{Te } 3d^{5/2}$ peak with double peak fit.

The distance between the peaks in the fitted curves are different from Di Bona, which could be an indication that a different stoichiometry has formed. It is not clear which one is formed, because more than one fit can be made. Figure 22 gives a schematic overview of the binding energies and corresponding compounds for respectively data from Di Bona (I) and the two fitted curves of Figure 20 (II) and Figure 21 (III). The latter two have been shifted such that the oxide peak coincides with that of Di Bona, assuming that the formed Te-Ox is the same. Values for the binding energies are obtained from a database⁸. For sputtered Te the binding energy is 572.9 eV, which is the same value Di Bona obtained. Vapour deposited Te has a binding energy of 573.1 eV. TeO₂ has a given binding energy of 575.8 eV, which is also close to that of Di Bona.

In case of the single peak (II), the shifted Te 3d^{5/2} peak has a value of 572.73 eV, which is close to the given values 572.72 eV of Cs_{2.4}Te and Cs_{2.69}Te. The former compound comes close to the calculated Cs to Te ratio of 2.35.

The second shifted fit (III) has two peaks at 573.2 and 572.5 eV. The first value can indicate the presence of a Cs_yTe compound or the presence of pure Te since this value is close to 573.1 eV, which is the value from pure vapour deposited Te. The second peak has a value close to that of Cs_{0.78}Te (572.53 eV), Cs_{0.90}Te (572.47 eV) or Cs_{2.6}Te (572.48 eV). None of these phases are the same as obtained by Di Bona, again suggesting that a different stoichiometry has been formed compared to our preparation process.

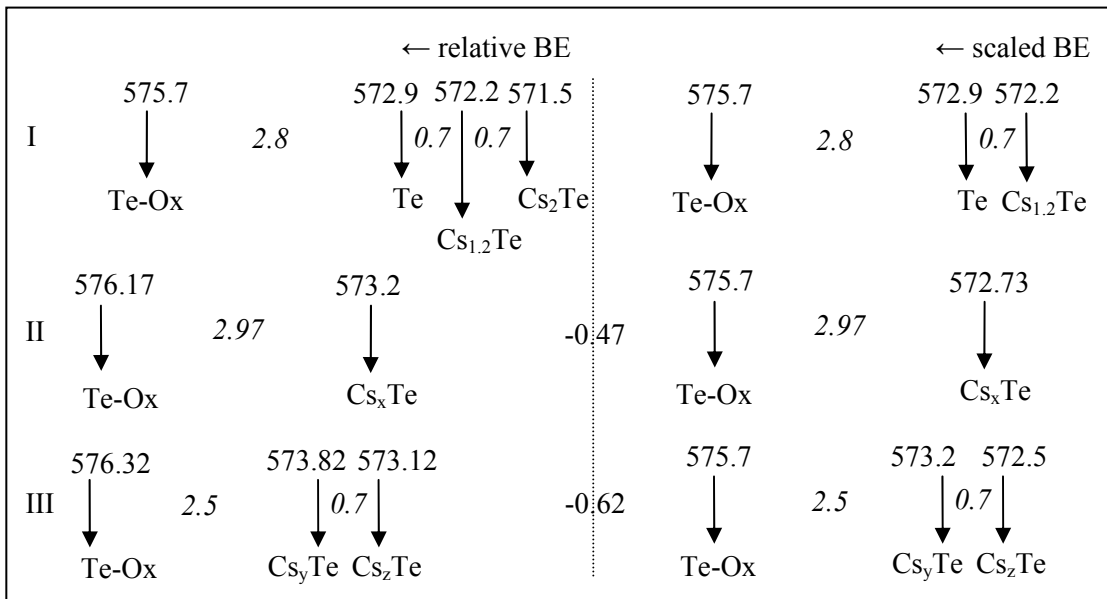


Figure 22: Scheme of binding energies and the difference energies (in eV) between the peaks. On the left-hand side I) data from Di Bona corresponding to figure w b, II) the fit with one peak corresponding to figure x and III) the fit with two peaks corresponding to figure y. On the right-hand side, the binding energies of the latter two are shifted to the first.

So the fitted curves show different values between the oxidised peak and the Te 3d^{5/2} peak; this suggests that a different stoichiometry of Cs-Te may have formed.

⁸ <http://srdata.nist.gov/xps/index.htm>

On the other hand, this XPS measurement has some shortcomings. It provides only an average value of the electron spectrum from near the surface (< 5 nm). In deeper regions, the ratio between Cs and Te most likely deviates from that of the surface layer. The spectrum may be shifted along the binding energy, but the exact shift is not known. We performed a shift assuming that the TeO₂ phase is the same as for the data from Di Bona. The resolution is not sufficient (around 0.7 eV) to distinguish between one or two compounds contributing to the Te 3d^{5/2} peak. Furthermore, there is not enough XPS data available about Cs and Te to successfully apply this technique and obtain definite conclusions, especially in case when the differences in binding energy between the various stoichiometric compounds are so small, for example, as estimated in the discussion about the cold and warm preparation approach (17 meV). It is therefore not surprising that not enough information is available to model the XPS data. A systematic investigation of XPS data for various types of Cs-Te photocathodes would unveil the possible stoichiometries. An in-situ XPS setup would allow getting information on the growth process.

4.3. Single Wavelength Ellipsometry

In order to properly apply SWE to our system and to correctly attain data, we describe the basic working principle and some details of SWE in this section.

4.3.1. Theoretical aspects

For understanding how quantitative measurements can be performed with ellipsometry, consider an incident polarised monochromatic light wave as indicated in Figure 23. The electric field can be described as a superposition of a wave polarised parallel to the plane of incidence (E^p) and a wave perpendicular to it (E^s), expressed mathematically as [60]

$$E_i^p(\mathbf{r}, t) = E_{i0}^p \cos(\mathbf{k}_i \cdot \mathbf{r}_i - \omega t + \varphi_i^p)$$

$$E_i^s(\mathbf{r}, t) = E_{i0}^s \cos(\mathbf{k}_i \cdot \mathbf{r}_i - \omega t + \varphi_i^s)$$

where \mathbf{k} is the propagation vector, ω is the angular frequency and φ is the phase of the wave. The same holds for the reflected E_r and refracted E_t waves. If the phases φ^p and φ^s are the same, the light is linear polarised. If the difference is 90°, the light is circular polarised. In general, the light is elliptically polarised. When light waves interact with matter, reflection, transmission and absorption can take place, and the amplitudes E_0 , the phases φ of both the p-state and the s-state and the direction of the waves are changed.

The film and substratum are characterised by their complex index of refraction $\tilde{N}_2 = n_2 - i\kappa_2$ and $\tilde{N}_3 = n_3 - i\kappa_3$ respectively, where n is the real index of refraction and κ is the extinction coefficient, which is related to the absorption coefficient α by $\kappa = \alpha\lambda/4\pi$. The extinction coefficient is a measure of how rapidly the light

intensity decreases over a distance z in the material, according to Beer's absorption law $I(z) = I_0 e^{-\alpha z}$.

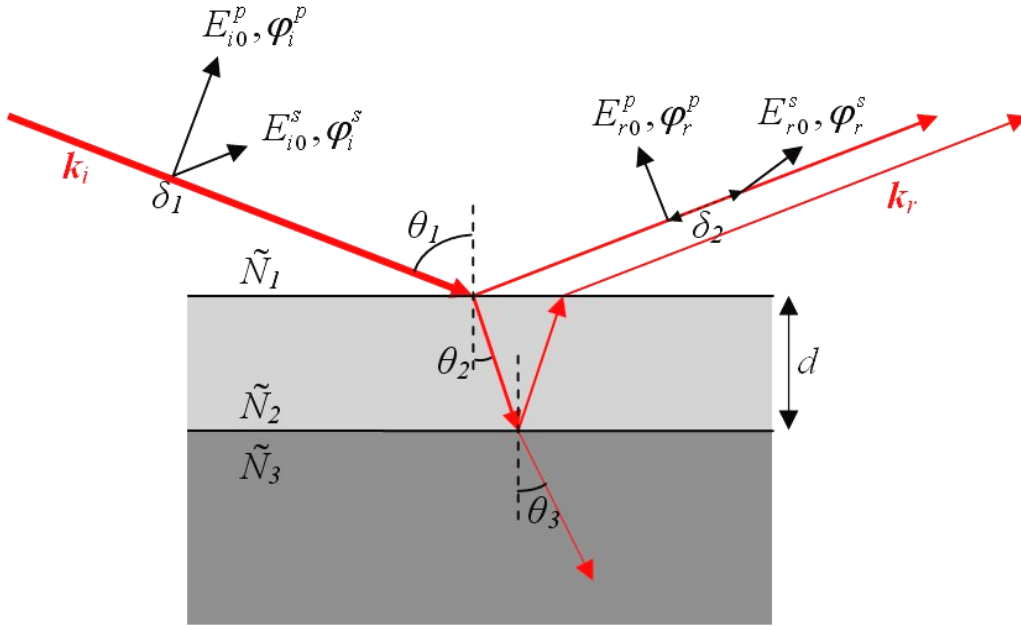


Figure 23: Schematic of the interaction of light with material, altering the amplitudes and phases of the p and s-waves. The resultant reflected beam is composed of the initially reflected beam and the infinite series of beams that traverse the film in and out (only the first one is shown).

Snell's law for refraction for the complex indices of refraction is given by $\tilde{N}_1 \sin \theta_1 = \tilde{N}_2 \sin \theta_2$, when a beam is incident from medium 1 onto medium 2. The Fresnel coefficients for reflection and transmission are given by [59], [60]

$$r_{12}^s = \frac{\tilde{N}_1 \cos \theta_1 - \tilde{N}_2 \cos \theta_2}{\tilde{N}_1 \cos \theta_1 + \tilde{N}_2 \cos \theta_2}; \quad r_{12}^p = \frac{\tilde{N}_2 \cos \theta_1 - \tilde{N}_1 \cos \theta_2}{\tilde{N}_2 \cos \theta_1 + \tilde{N}_1 \cos \theta_2};$$

$$t_{12}^s = \frac{2\tilde{N}_1 \cos \theta_1}{\tilde{N}_1 \cos \theta_1 + \tilde{N}_2 \cos \theta_2}; \quad t_{12}^p = \frac{2\tilde{N}_1 \cos \theta_1}{\tilde{N}_2 \cos \theta_1 + \tilde{N}_1 \cos \theta_2}.$$

The same applies for the coefficients when the beam is incident from medium 2 into medium 3.

The amplitude reflection coefficient R is defined as the ratio of the amplitude of the outgoing resultant wave to the amplitude of the incoming wave. For a single film-substratum sample as shown in Figure 23 the total reflection coefficients are given by

$$R^s = \frac{r_{12}^s + r_{23}^s e^{-i\beta}}{1 + r_{12}^s r_{23}^s e^{-i\beta}}$$

$$R^p = \frac{r_{12}^p + r_{23}^p e^{-i\beta}}{1 + r_{12}^p r_{23}^p e^{-i\beta}}$$

$$\text{with } \beta = 4\pi \left(\frac{d}{\lambda} \right) \tilde{N}_2 \cos \theta_2.$$

Here β is the phase difference between the part of the wave reflecting from the top surface and the part of the wave that traversed the film in and out; d is the thickness of the film medium 2.

The reflectance is the ratio of the intensities (not the amplitudes) of the reflected wave to the incoming wave, and is the square of the magnitude of the total amplitude reflection coefficient:

$$\mathfrak{R}^s = |R^s|^2 = I_r^s / I_i^s \text{ and } \mathfrak{R}^p = |R^p|^2 = I_r^p / I_i^p.$$

An example of typical graphs of the Fresnel coefficients and the reflectance of a single layer with $n = 2.2$ and $\kappa = 0$, are given in Figure 24.

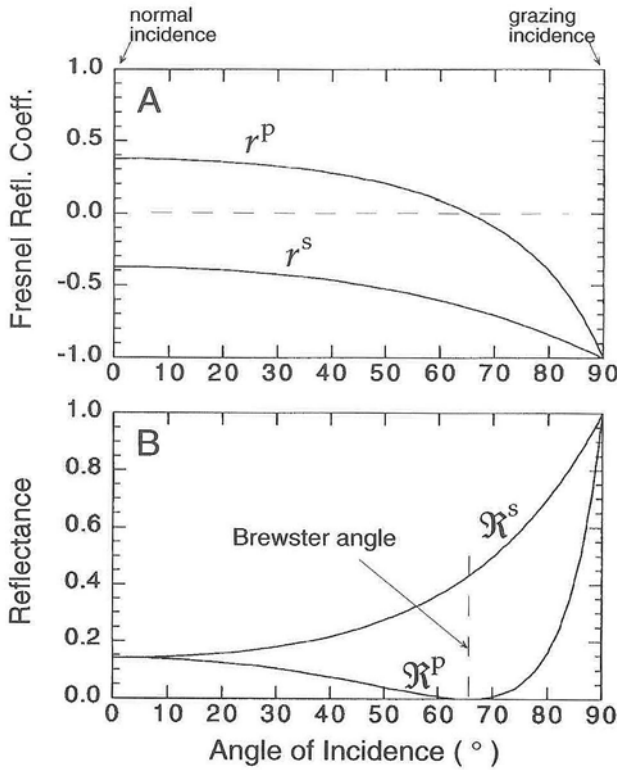


Figure 24: (A) The Fresnel reflection coefficients and (B) reflectance as function of the angle of incidence for a dielectric with $n = 2.2$ and $\kappa = 0$, at a wavelength of 632.8 nm. The reflectance of the p-polarised wave has its minimum at the Brewster angle, approaching zero for non-absorbing matter.

In ellipsometry, the ratio of the magnitudes of the total reflection coefficients is defined as an angle Ψ via

$$\tan \Psi = \frac{|R^p|}{|R^s|}.$$

Δ describes the phase shift induced by the reflection on the sample, where Δ is defined as $\Delta = \delta_1 - \delta_2$, with δ_1 the phase difference between the p-wave and the s-wave before reflection and δ_2 that phase difference after reflection. For example, a 1 nm change of layer thickness corresponds to a change in Δ of 2.5° when the index of refraction is 2.0 ([59], page 66).

The amplitude transfer and phase transfer is summarised in the fundamental equation of ellipsometry

$$\rho = \tan \Psi e^{i\Delta} = \frac{R^p}{R^s}.$$

The information about the film is contained in the total reflection coefficients and hence in ρ . The measured quantities are the angles Ψ and Δ , thereby determining the polarisation state of the reflected beam. The film thickness and its optical constants can be calculated by fitting parameters to the Delta/Psi trajectories obtained from measurements. This will be described in the following section.

4.3.2. Delta/Psi trajectories

When Ψ and Δ are continuously measured during deposition of a film onto a substratum, the development of the Ψ and Δ values can be plotted in the form of a Delta/Psi trajectory, such as shown in Figure 25.

The starting point of the trajectory depends on the refractive index of the film-free substratum. The Delta/Psi value directly corresponds to the complex refractive index \tilde{N}_3 of the substratum through the relation ([59], see page 63)

$$\tilde{N}_3 = \tilde{N}_1 \tan \theta_1 \sqrt{1 - \frac{4\rho \sin^2 \theta_1}{(\rho + 1)^2}}.$$

Different values for \tilde{N}_2 will give different trajectories. The position on the curve relates to the thickness of the film. To determine the values for n_2 and κ_2 from the measured parametric curve, fitting procedures are used, e.g. a code as provided by McCrakin in FORTRAN [61]. Transparent films have closed trajectories that correspond to periodically repeating positions of Ψ and Δ as a function of increasing film thickness. An example is given in Figure 25a. The Delta/Psi trajectory of an absorbing film (e.g. Figure 25 b) approaches the value of the bulk material in an ever tightening spiral. The point (Ψ, Δ) thus moves from an initial position (corresponding to the substratum) to the final position given only by the (bulk) film properties.

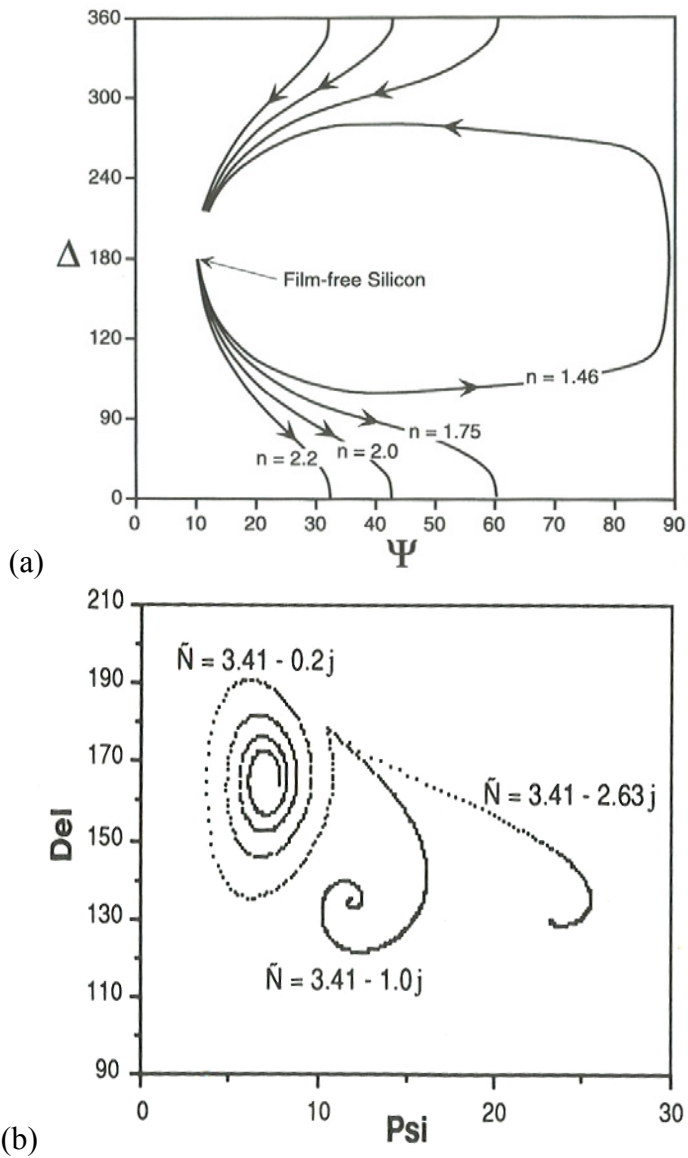


Figure 25: (a) Delta/Psi trajectories for transparent films on silicon. Dissimilar indices of refraction give different trajectories. (b) Delta/Psi trajectories for hypothetical materials with different absorption coefficients. Larger values of κ cause the spiral to close more rapidly.

For a two-layer system, the lower layer causes a shift of the trajectory for the upper layer from its single-layer location. In Figure 26 an example of this shift is shown as the region with dotted symbols for nitride on silicon and silicon dioxide. This illustrates what might be observed as well when layers Cs-Te with different stoichiometry are grown on each other, because two layers should possess different optical properties.

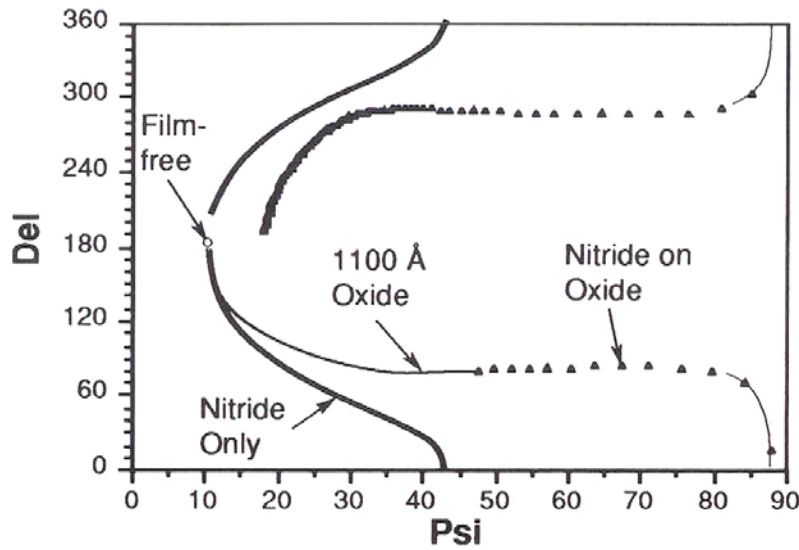


Figure 26: An example of a two-layer trajectory where nitride is deposited on top of 1100 Å silicon dioxide in 10 Å increments. The curve of the single film nitride on silicon is also plotted.

To more detail, the following scenario is expected when ellipsometrically monitoring the growth of Cs_2Te photocathodes: first a Te layer of a certain thickness is deposited onto the substratum, corresponding to a certain trajectory and initial Delta/Psi value for the deposition of Cs that is started thereafter. By altering the preparation conditions, for example, varying the evaporation rate of Cs, various stoichiometric compounds will be formed with different refractive indices \tilde{N}_2 . Therefore, one can expect that the formation of different stoichiometric compounds will produce different Delta/Psi trajectories.

4.4. Diagnostic setup

The basic setup for ellipsometry consists of a light source, a polarizer with or without a compensator (e.g. a quarter wave plate to make the incident light elliptically polarised), an analyser and a detector [59]. Typically, the angle of incidence on most instruments is fixed at 70° and a 632.8 nm He-Ne laser light source is used. The most basic ellipsometer configuration is the null ellipsometer, given in Figure 27a. With this setup, the polarizer and the analyser are rotated to extinguish (null) the signal from the detector to draw quantitative conclusions on the optical properties of the sample, from the found nulling-angle.

Alternatively, a rotating polarizer or rotating analyser ellipsometer can be used (Figure 27b), in which either the polarizer or analyser is rotated continuously and the intensity of the reflected light is measured as function of time and angle.

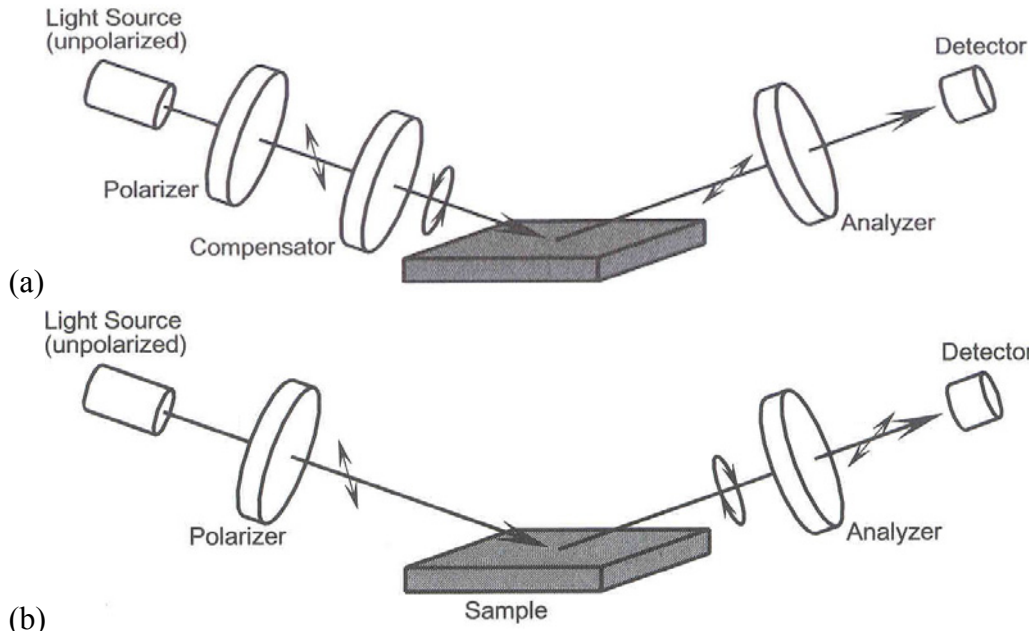


Figure 27: (a) Setup of null ellipsometry. The polarizer and the analyser are rotated to extinguish (null) the signal from the detector. (b) Setup of rotating element ellipsometry. The polarizer or analyser is rotated continuously and the intensity of the reflected light is measured as function of time and angle.

To implement an ellipsometric setup of Figure 27 in our existing preparation chamber the beam path has to be modified, which is (usually) required and possible when the incoming beam and the outgoing beam have to pass the same window. The outgoing beam is reflected from the sample onto a copper mirror and reflected back via the sample and shares the same path as the incoming beam. To prevent the light from going through the polarizer and an analyser twice, which would lead to incorrect interpretation of the signal, we modified the beam path. The setup will be discussed in the next paragraph. With this modification, we detect both polarisations separately, from which we can obtain Ψ , Δ , and additional information on the separate intensities of the polarised beams. The latter can provide an indication of the macro roughness, because that only affects the absolute values of the reflectances, but not the ratio.

We can determine Ψ by measuring the intensities of the p and s waves separately, because $\tan \Psi$ is the ratio of the magnitudes of the total reflection coefficients for the p and s waves, and thus the ratio of the square roots of the reflectances of the p and s waves. Taking into account that the beam is reflected twice on the sample and $I_r = \Re^2 I_i$, this results in

$$\tan \Psi = \frac{|R^p|}{|R^s|} = \frac{\sqrt{\Re^p}}{\sqrt{\Re^s}} = \frac{\sqrt[4]{I_r^p / I_i^p}}{\sqrt[4]{I_r^s / I_i^s}} = \sqrt[4]{\frac{I_r^p}{I_r^s}} / \sqrt[4]{\frac{I_i^p}{I_i^s}}$$

If we take the polarisation of the incoming wave exactly at 45° with respect to the plane of incidence then $I_i^p = I_i^s$, we only need to measure the intensities of the reflected wave and take the ratio. This approach with stationary polarizers is particularly useful because during monitoring the film growth, Ψ is will be a

function of time. Actually, the value of I_r , and thus the calculated reflectance, is smaller due to losses by the window of the preparation chamber, the copper mirror and the beam splitter cubes in the diagnostic setup itself. An estimation should be made for this loss factor.

To determine Δ as a function of time, the phase difference of the p and s component of the reflected light is determined individually with aid of reference beams. The signal interferes with the reference beam and from the change in intensity, the phase difference can be calculated (see Appendix 2).

Thus, Ψ and Δ can be measured separately as a function of thickness, since the thickness is a function of time. Ψ and Δ can be plotted parametrically as function of time as well, to obtain a Delta/Psi trajectory.

The scheme and the actual setup built, are shown in Figure 28. The details on the beam path and the detection are as follows: the 2 mW HeNe laser is linearly polarised. Two reference beams are split of by polarising beam splitter cubes. The initial polarisation is therefore slightly tilted. By changing the angle, the intensity of the beams can be varied. Half wave plates are used to rotate the polarisation again. The Faraday isolator rotates the polarisation by an angle of 45° resulting in a beam that contains both the s and the p-state. Reflection on the sample will change the polarisation to elliptical. A non-polarising beam splitter cube deflects the reflected beam. A Faraday isolator is used to prevent the remaining reflected beam to be coupled into the laser; to avoid feedback. A polarising beam splitter cube separates the two reflected polarisation states. From each state, the intensity is measured by splitting of a part of the beam with a non-polarising beam splitter cube. The remaining part interferes with the reference beam, to determine the phase change. Si photodiodes⁹ with a sensitivity of 0.43 A/W are used to detect the signals.

⁹ Hamamatsu S2386-5K

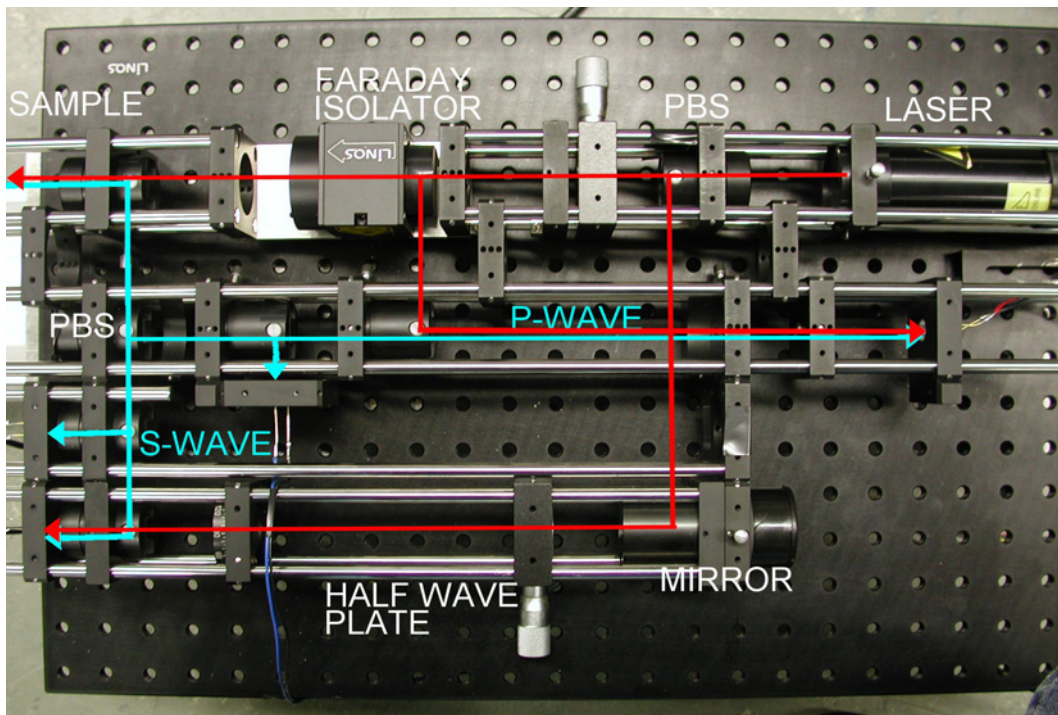
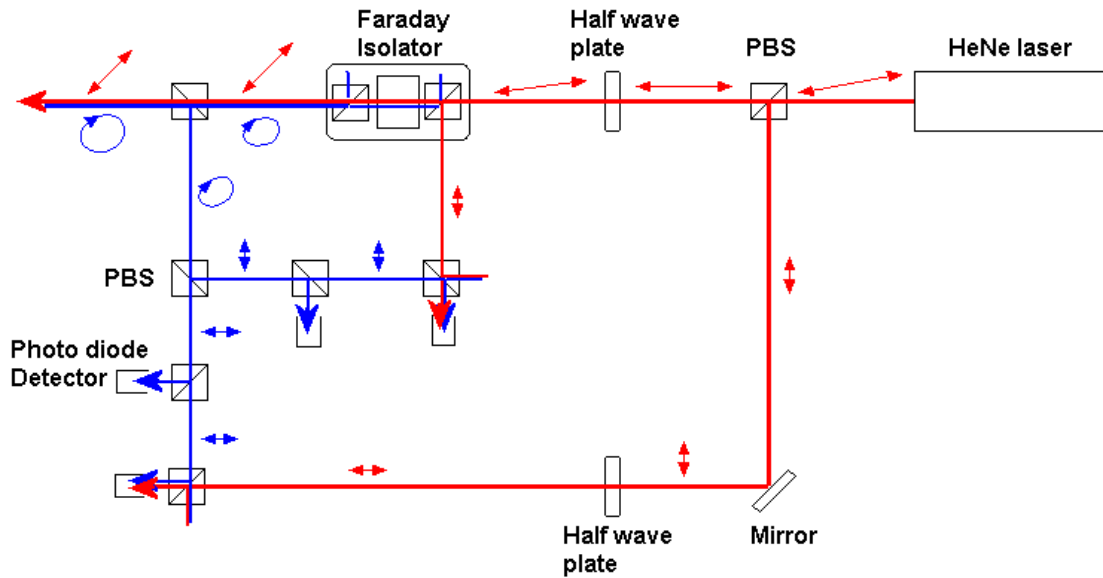


Figure 28: Schematic and actual diagnostic setup based on ellipsometry. The red line is the out going beam; the blue line is the beam reflected from the sample. The Faraday isolator consists of two polarising beam splitter cubes (PBS) and a magnet to rotate the polarisation. The other five cubes are non-polarising beam splitter cubes.

The setup is realised in a rugged, portable and mountable manner with using a microbench system in which all components are mounted on a base plate. This plate is connected to an X95 construction that is mounted under an angle of 15° with respect to the normal of the floor, as can be seen on the photo in Figure 29. The entire ellipsometer on its base plate can be rotated and translated accurately to align the system with respect to the photocathode and the mirror.

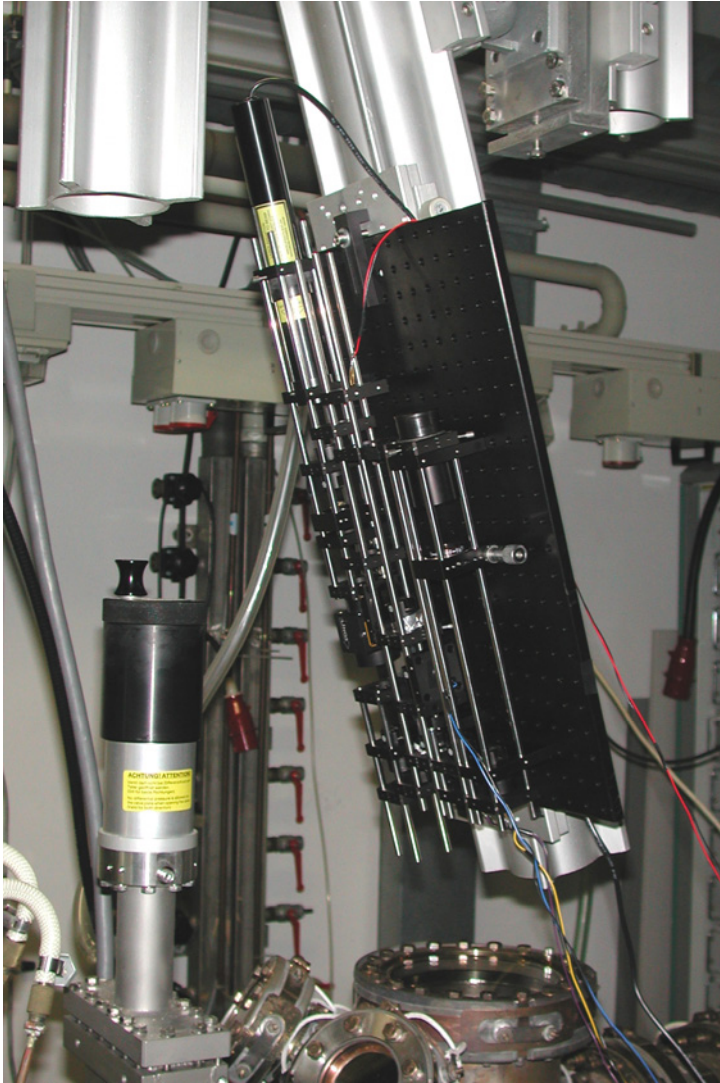


Figure 29: Diagnostic setup positioned above the preparation chamber. Inside the chamber, a mirror is mounted. X95 profiles are used to accurately align the whole setup.

The light coming back from the cathode can be very weak and noisy due to unexpected scattering on the mirror and the coating of the window. Therefore, the diode signals are amplified and filtered with a low-pass filter according to the scheme in Figure 30. A chopper is used to increase the S/N ratio.

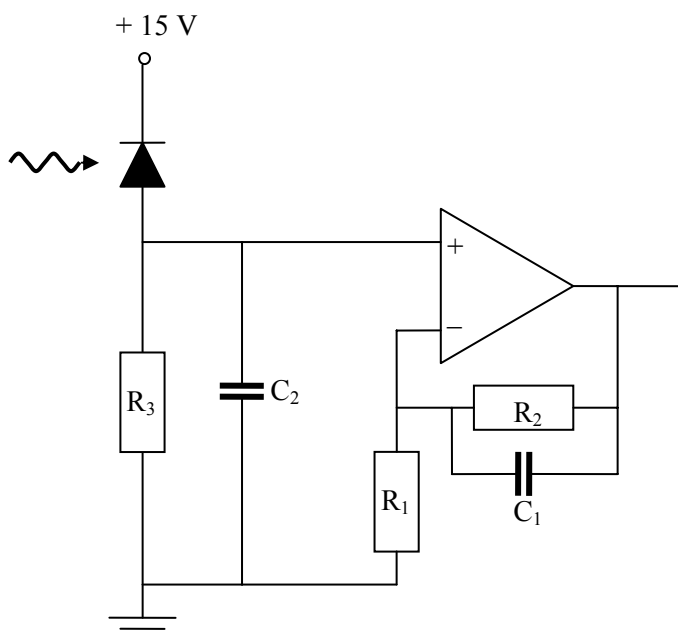
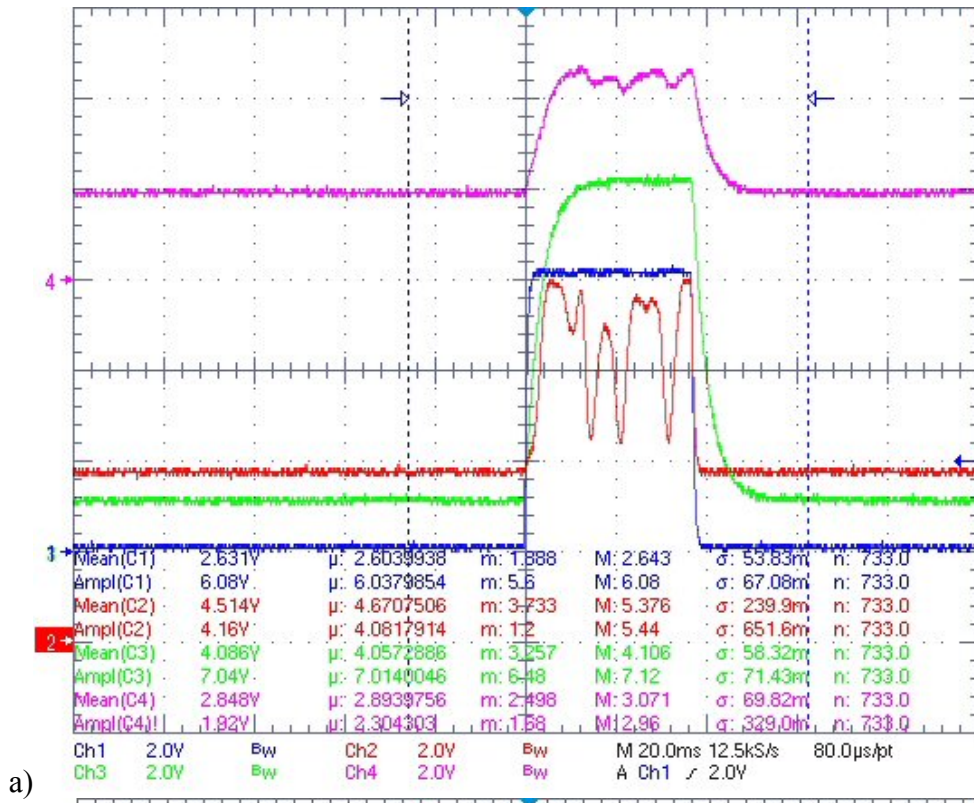


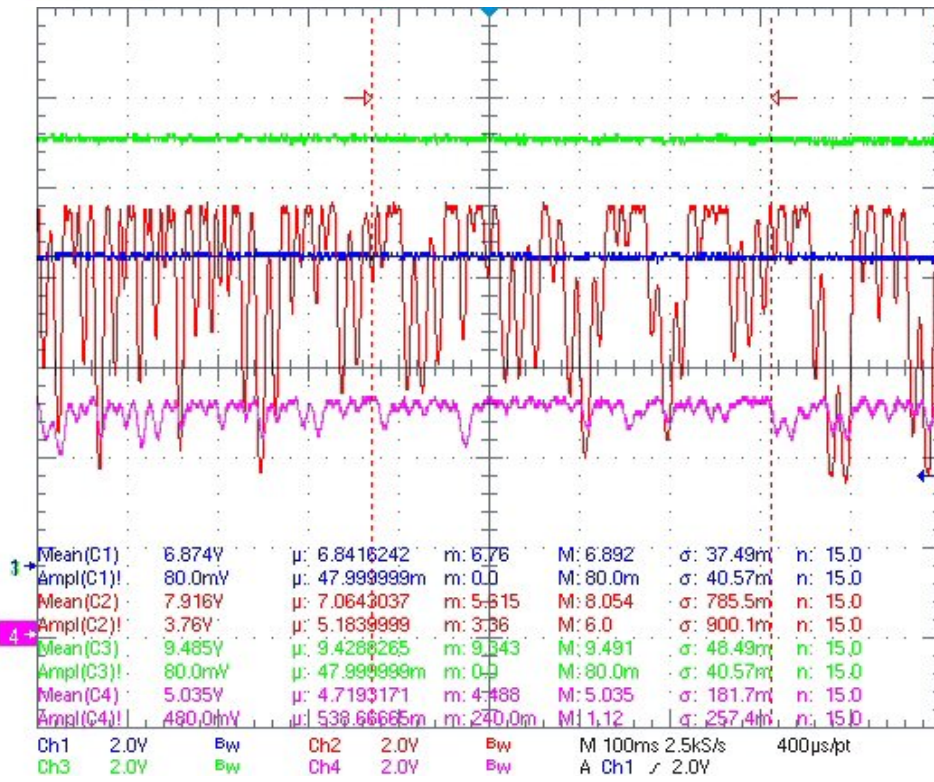
Figure 30: Schematic of detection system. A biased photodiode generates a current when illuminated. A non-inverting amplifier is used to amplify the current generated by the p-wave by a factor of 101 ($\text{gain} = 1 + R_2/R_1$) and by a factor of 11 for the current generated by the s-wave. Two low-pass filter with $f_{3dB} = 1/2\pi RC = 4.8 \text{ kHz}$ are used to filter out noise outside the frequency range of interest. Because of 50 Hz noise, the photodiode was isolated from the setup. $R_1 = 150 \text{ }\Omega$ or $1.5 \text{ k}\Omega$, $R_2 = 15 \text{ k}\Omega$, $R_3 = 1.2 \text{ M}\Omega$, $C_1 = 220 \text{ nF}$ or 22 nF , $C_2 = 27 \text{ pF}$.

Figure 31a shows an example of the typical signals coming from the setup recorded by an oscilloscope. The chopped signals from channel 1 (blue) and 2 (red) correspond to the s-wave, from which respectively the amplitude and the phase can be determined. The same holds for channel 3 (green) and 4 (purple) that correspond to the p-wave. The rise time of these signal is longer, because the light intensity of the p-wave and thus the generated current is so low, with as result a large internal impedance of the photodiode, which has trouble with charging the capacitor C_2 . Due to vibrations of the cathode, the interfering beams (signals from channel 2 and 4) show large oscillations, which vary in time. A peculiar aspect in those signals is the well-defined maximum that can be clearly seen if the time scale is increased (see Figure 31b). Apparently, it could be that the vibrations are random though confined to one direction from the vibration free reference point. For the signal, only the maximum value would be necessary. The interference pattern can be used to ensure that the beams are correctly aligned. Further test measurements have to point that out. A number of additional recommendations for improving the setup are given in Appendix 5.

The signals look promising so far and after additional optimisations they can be successfully used to measure the change in intensities, and thus the change in Ψ and Δ . Therefore, this diagnostic setup will be very suitable to investigate the coexistence of different stoichiometric compounds.



a)



b)

Figure 31: Signals from the diagnostic setup. a) The beam from the cathode is chopped. The amplitudes of the chopped signals contain the information about the intensities. Channel 1 (blue) and 2 (red) correspond to the *s*-wave, channel 3 (green) and 4 (purple) correspond to the *p*-wave. b) The time scale is larger. A well-defined maximum is visible for channel 2 and 4.

4.5. Conclusions

Diagnostic measurements have to prove the suggestion that different stoichiometric Cs-Te compounds form when the preparation conditions for growing Cs-Te photocathodes are changed. A first indication was obtained by comparing an XPS measurement on our photocathode with that of XPS measurements on photocathodes from INF. The spectra are different which might be due to the difference in photocathodes. Definite conclusions could be drawn when a systematic recording of XPS spectra (preferably in-situ) for various Cs-Te photocathodes would be performed.

As a second diagnostic tool, we designed and constructed a diagnostic setup based on single wavelength ellipsometry, which we implemented on our preparation chamber to perform non-destructive, in-situ, real-time measurements. Initial test measurements show that the setup is successfully implemented inside our existing preparation chamber. Herewith, we expect in the near future to detect changes in amplitude and phase of the p-wave and the s-wave separately as a function of time during deposition of Cs-Te photocathodes. To more detail, with the values of Ψ and Δ recorded as a function of time, one can obtain Delta/Psi trajectories, which enables, for the first time, to distinguish between various stoichiometric Cs-Te compounds. In particular, we expect that altered preparation conditions should result in different trajectories because of the correspondingly different values of the optical constants n_2 and κ_2 for the various compounds. Finally, this will lead to a better understanding of the preparation process and an improved control during deposition of the Cs-Te photocathodes.

5. Magnesium photocathodes

For the Laser wakefield accelerator project, the emphasis of the photocathode performance lies on the fast response time, rather than a maximum QE. Therefore, we have chosen to use a metallic photocathode, instead of Cs₂Te, to produce the required short fs electron bunches. From the overview in paragraph 2.2 it is apparent that the most commonly used metallic photocathode is copper, because it is very robust and easy to prepare. However, the QE is rather small (typically 10⁻⁵ to 1·10⁻⁴) and this still requires high drive laser power in the UV. We concluded that for moderate laser power, the most promising photocathode is Mg. The QE of Mg lies typically between 10⁻⁴ to 10⁻³. Also other research groups are meanwhile investigating this photocathode as well.

In the first section, we present an overview of the properties of Mg photocathodes to further illustrate our choice. Occasionally a comparison is made with Cu photocathodes. The overview also serves as a background for our particular design of a new preparation chamber in which the preparation and performances of the Mg photocathode can be tested. The construction of this chamber is described in the second section.

5.1. Magnesium photocathodes overview

Several groups have investigated the performances of magnesium photocathodes with respect to quantum efficiency, thermal emittance and robustness. The Schottky effect and the effect of laser cleaning have been studied as well. In the table in Appendix 3, a summary is given of the reported research on magnesium cathodes.

Magnesium has a work function of 3.66 eV [62]. Values for Cu vary from 4.3 eV to 4.7 eV depending on the crystal orientation¹⁰ [1], [62]. Therefore, the applied laser frequency must be such that the photon energy is higher than these values, e.g. by using the third harmonics of a Ti:Sapphire laser with a wavelength of 267 nm (4.64 eV). Laser pulse lengths used so far are in the order of tens picoseconds. Only Serafini et al. studied the possibility of generating subpicosecond electron bunches from a magnesium photocathode by using 166 fs laser pulses [63]. Endo et al. performed experiments with 100 fs UV laser pulses, but obtained relatively low efficiency [64]. Fischer et al. investigated the effect of high intensity laser pulses of 300 fs and 2 eV photon energy [65]. Actually, so far not much is known about the non-linear response of magnesium, the response to shorter pulse lengths or high intensity laser pulses of 267 nm, or the effect of ultra short, high intensity laser pulses of this frequency. Interesting research could be performed along these subjects on Mg.

5.1.1. Photocathode structure

Our first point of attention concerns the choice of a suitable type of magnesium photocathode, as each of them shows its own advantages and disadvantages: solid

¹⁰ <http://environmentalchemistry.com/yogi/periodic>

rods [66]; bulk magnesium disks that are press fitted [67]-[69], friction welded [70]-[75] or mounted by Hot Isostatic Pressure (HIP) technique [76]; and thin films deposited by ion sputtering [10], evaporation [77] or Pulsed Laser Deposition [78]. The solid rod is the simplest configuration. Press fitted magnesium showed RF breakdown at high electric surface fields at the Mg-Cu junction. This effect was not seen with sputtered Mg onto Cu [10], [71]. Another group of BNL (Wang et al.), however, asserts that sputtered magnesium also is damaged during RF breakdown and suggested frictional welded magnesium [71]. Though, at SLAC it was shown that frictional welding led to the same problem with high RF fields [74]. Subsequent laser scanning could restore the QE after RF breakdown [79]. In general, it was concluded that for magnesium photocathodes the maximum tolerable field is about 120 MV/m. At the setup at the University of Twente only moderate fields will be applied (< 28 MV/m), so that damaging by RF breakdown is not considered as a problem.

5.1.2. Increasing the QE

The QE of Mg photocathodes is high compared to other metallic photocathodes and can be increased even more by laser cleaning and applying an electric field at the surface (Schottky effect), which will be described in the next paragraphs. Increasing the QE has a (slightly) negative effect on the emittance. This will be discussed in the subsequent paragraph. In the last paragraph, an alternative approach to increase the QE is discussed.

5.1.2.1. Laser cleaning

It has been observed that the QE of Mg is very sensitive to preparation conditions like polishing, cleaning and baking the surface, and especially to laser cleaning. In general, the surface is polished with 1 μm diamond powder and then baked. Thereafter, the QE is in the order of 10^{-4} without laser cleaning. For laser cleaning, the surface is scanned with high intensity laser pulses near the damage threshold to ablate the top oxidised layer resulting in a pure magnesium surface. The various methods of laser cleaning used differ a lot as is reported in papers and summarised in Appendix 3 and in the following paragraphs. The result of laser cleaning is a significant increase of the QE by about one order of magnitude [10], [41], [69], [76], [78].

Srinivasan-Rao et al. from Brookhaven National Laboratory (BNL) showed that the QE was improved to $2 \cdot 10^{-3}$ after systematic laser cleaning. This QE was obtained with bulk magnesium [69] where a 2 cm diameter, 99.8% pure magnesium disc was press fitted onto a copper substratum; and with sputtered magnesium [10] where a 20 μm thick Mg layer was ion-sputtered onto a copper substratum. This indicates that the improvement of the QE seems independent of the deposition method. Sputtered magnesium has a damage threshold that is 6 times larger with respect to bulk magnesium. Thus, higher charge densities can be extracted from sputtered Mg since the maximum extractable peak charge density is proportional to the product of QE and peak laser power just below the damage threshold. BNL ascribes the enhancement of the damage threshold to sputtering, but more likely it is the effect of a thinner film of Mg placed on copper, which has

a very high thermal conductivity and allows the magnesium layer to cool down faster.

The effect of applying a high RF field during laser cleaning is ambiguous, because the same QE is obtained with sputtered magnesium apparently without applying an RF field. The laser cleaning was performed with $300 \mu\text{J}/\text{mm}^2$ pulses for 90 minutes for sputtered magnesium, and $160 \mu\text{J}/\text{mm}^2$ for bulk magnesium. The affected depth were estimated to be $1 \mu\text{m}$ and $< 12 \mu\text{m}$ respectively.

Nakajyo et al. from Sumitomo Heavy Industries Japan (SHI), performed laser cleaning on HIP magnesium with comparable laser energy of $120 \mu\text{J}/\text{mm}^2$, without applying an RF field [76]. A comparable QE of $1 \cdot 10^{-3}$ was obtained. The QE before laser cleaning was $8.5 \cdot 10^{-5}$. So, again, the preparation technique seems of no significance.

Brogie et al. from the University of California have laser cleaned magnesium cathodes above damage threshold at a DC field test gun under 10^{-6} Torr vacuum conditions [41]. The QE initially increased by a factor of 220. However, since magnesium is rather reactive with oxygen, the QE quickly decreased afterwards. The stabilised QE was still a factor of 65-70 higher than before laser cleaning. Laser cleaning on copper photocathodes merely resulted in a doubling of the QE. Additionally, polished cathodes showed less variation of the QE over the surface than unpolished cathodes.

A somewhat different laser cleaning method was used by Cultrera et al. from INFN Italy [78]. A 20 nm protective oxide layer was deposited on a 200 nm pure magnesium film. The oxide layer was subsequently ablated with a much higher laser intensity of $90 \text{ mJ}/\text{mm}^2$. With this method the QE increased by one order of magnitude as well.

Schmerge et al. from Stanford Linear Accelerator Centre (SLAC) tried to perform laser cleaning with $800 \mu\text{J}/\text{mm}^2$ without a RF field, but no increase of the QE was obtained [74]. However, a much smaller spot size was used during scanning compared to the other groups, which could mean that they did not succeed to clean a significant fraction of the surface.

The lifetime of magnesium photocathodes and in general metallic photocathodes is very long: magnesium has an operational lifetime of more than 5000 hours [67]. Laser cleaned magnesium has a lifetime in the order of months before a new cleaning procedure is necessary [69], [71].

The QE can also be increased by a moderate amount when irradiating the photocathode near the Brewster's angle and orient the electric field of the laser in the plane of incidence [65], [71], [75], [82]. The QE increased by a factor of 3 if p-polarized light was used at 72° , which is around the Brewster's angle (65°) of magnesium [68]. Graves et al. [80] showed that the polarisation had no effect on the emittance.

5.1.2.2. Schottky effect

Another approach to increase the QE is by operating the photocathode in high electric fields, which reduces the work function. This is called the Schottky effect, and follows from the definition of the QE, which can be described by

$$QE = A(h\nu - \phi)^2 .$$

Here A is a constant depending on material properties like the absorption coefficient, density of states and the polarisation and angle of incidence of the laser light [62]; ϕ is the work function of the material, which is lowered with increasing applied electric field E [66], [76] according to

$$\phi = \phi_0 - b\sqrt{\beta E}$$

where ϕ_0 is the work function at zero field. For magnesium ϕ_0 is 3.66 eV. $b = \sqrt{e/4\pi\epsilon_0} \approx 3.79 \cdot 10^{-5}$ (in MKS units) and β is an empirical field enhancement factor that depends on the cathode surface properties. For example, a perfectly flat, clean surface has a value β equal to 1 [80], while a rough surface has a higher value for β . Contaminations influence β as well, so that values of β can vary significantly from one setup to another. For magnesium, values between 6 and 8, between 20 and 48 and unexpectedly 0.1 were obtained at BNL [69], [72], and between 6 to 7 at ANL [66]. For copper β -values of 3.1 and 90-100 were found [80], [81]. In the view of these findings, researchers have tried to modify the surface properties in order to increase the QE. Srinivasan-Rao showed that polishing the surface with 1 μm diamond powder increased the Schottky effect and therefore the QE at high fields [10]. It could be that in this way, the β -value increased because the surface had been roughened up. A side-advantage of applying a higher field, in order to make use of the Schottky effect, is that in case of high charge production, space charge effects are reduced due to a faster electron extraction [62].

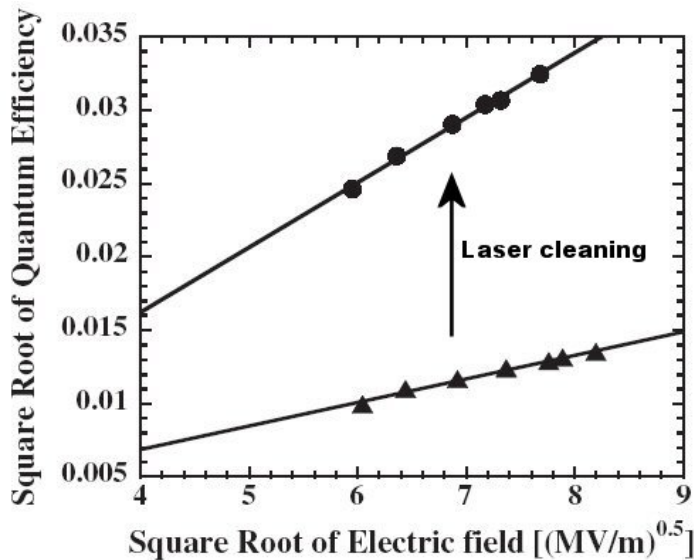


Figure 32: QE at 262 nm of a Mg photocathode as a function of peak electric field before (triangles) and after (dots) laser cleaning. The slope of the curve equals $b\sqrt{A\beta}$. The cut off with the y-axis equals $\sqrt{A}(h\nu - \phi_0)$. One can determine A , and with that the values for β and ϕ_0 , from the slope of a graph where the square root of the QE is plotted versus photon energy.

The QE increased typically by about a factor of 2 when applying an electric field. However, from the graph in Figure 32 [76] it becomes evident that the effect of

laser cleaning is larger than the effect of applying a higher field. Moreover, because of the moderate fields in our linac, we therefore focus our attention solely on laser cleaning to increase the QE of Mg photocathodes, instead of applying high electric fields.

5.1.2.3. Influence of QE on emittance

When considering increasing the QE of the photocathode in an accelerator one has to be aware that this may bring along also an undesired effect, which is an increase of the emittance. We will explain the cause for this effect and review possible countermeasures.

An electron bunch, as required in accelerator application, has a high current density and a low emittance. The emittance is a property that is related to the size and divergence of the electron beam and is mainly determined by the size of the laser spot on the cathode and the electron density¹¹ of the bunch. BNL and the University of Tokyo investigated the emittance for Mg photocathodes [67], [71]-[73]. After acceleration, the emittance of a beam is the sum of the intrinsic emittance from the photocathode (thermal emittance) and the emittance growth during acceleration¹². The growth during acceleration depends on the design of the accelerator that is used and the operational conditions. Therefore, the values of the emittance in Appendix 3 are difficult to compare since various groups use different accelerator designs. Correspondingly, both very low and high values for the emittance have been obtained for both Mg and Cu photocathodes. The thermal emittance ε_{th} , on the other hand, is a property of the photocathode itself. It is proportional to

$$\varepsilon_{th} \propto \sigma \sqrt{E_k / mc^2} \text{ where } E_k = h\nu - \phi_0 + b\sqrt{\beta E}$$

where σ is the rms laser spot size that defines the diameter of the electron bunch when leaving the cathode. [66], [71], [80]. From this formula and the before mentioned formula for the QE it follows that the QE depends on the same parameters as the thermal emittance, though the former, in addition, on the before mentioned material properties A . The relation between the QE and the emittance can be rewritten as

$$QE \propto A\varepsilon_{th}^4.$$

Therefore, a higher QE will intrinsically result in a larger emittance and vice versa. As expected from this, measurements on Cu and Mg photocathodes show a larger QE and emittance for the Mg compared to Cu cathode [74] at normal incidence. In other experiments, however, Wang et al. from BNL found that the thermal emittance of Mg photocathodes in an RF field was smaller than the theoretical value and even smaller than for Cu cathodes [71]. They explained this effect as a consequence of (Schottky dominated) surface emission in magnesium, whereby the mismatch between the photon energy and work function is of no importance. Conservation of energy and momentum would ensure that the electrons move perpendicular to the surface, which leads to high parallelism and thus a low emittance. They obtained a very low emittance of 0.6 mm mrad.

¹¹ www.fnal.gov/pub/now/definitions/emittance.html

¹² <http://www.fieldp.com/cpb/chap03.pdf>, page 91.

There are several possible methods to reduce the thermal emittance. The first approach is by decreasing the laser spot size (this follows directly from the equation for emittance). However, this approach is limited by space-charge effects. An alternative method was proposed by Yusof et al. from Argonne National Laboratory (ANL) to reduce the thermal emittance, by making use of the Schottky effect and applying laser pulses with a photon energy smaller than the work function ϕ_0 . The applied electric field would then deliver the missing energy of the photons to emit the electrons into vacuum. Another suggestion was to use a curved laser front or a curved photocathode surface to compensate for the curvature and emittance of the electron bunch [62], [82]. A fourth approach is to use ultra short laser pulses, because according to Graves et al. [80], the emittance grows as a function of the electron bunch length at constant charge, below the space charge limit. The graph in Figure 33 shows their calculations of the emittance as function of the produced electron bunch length (in ps pulsed duration of the drive laser), in which the shortest bunch length has the lowest emittance. We conclude that the use of fs laser pulses, as used in the LWFA project, should improve the emittance of the electron bunch.

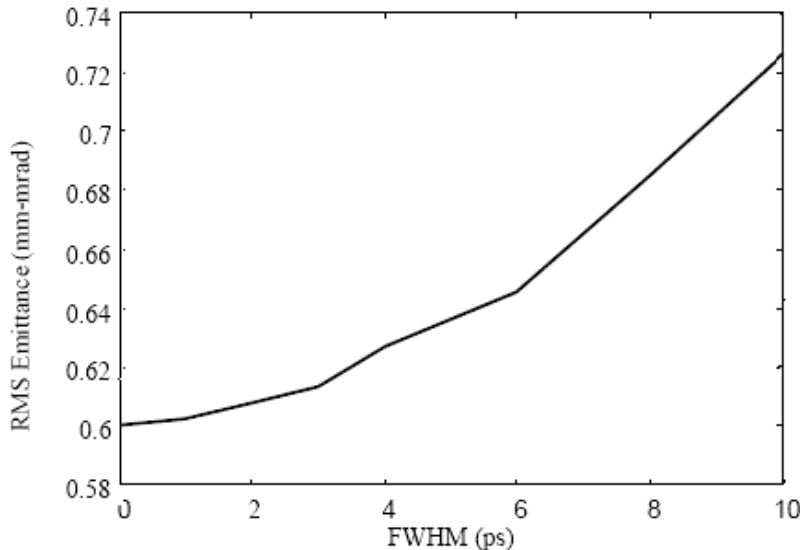


Figure 33: Simulation of emittance versus bunch length for a fixed charge of 2 pC and E field of 95 MV/m on a Cu cathode.

5.1.2.4. Oxygen adsorption

To finish this section with methods that increase the QE we name oxygen adsorption, as investigated by Yuan et al. from Stanford University [77]. A monolayer of ionised oxygen increased the QE by lowering the work function of the magnesium photocathode. Their obtained QE was the same as after laser cleaning, namely 0.2 %. However, further exposure to oxygen led to the growth of an oxide layer that resulted in a lowering of the QE and saturation of oxygen uptake. For over 24 hours, the maximum QE changed less than 1 % if the pressure was kept at 10^{-10} Torr. Lower oxygen pressures resulted in higher peak QE's as well as more oxygen uptake (see Figure 34). When the same amount of oxygen was adsorbed at a higher pressure, the resulting QE was lower. Thus, partial pressures play a critical role in the adsorption, which may be due to a difference in

oxide structure between higher and lower pressure. This indicates that magnesium photocathodes are best to be operated in ultra high vacuum conditions. This can also be concluded from [41] where the QE after laser cleaning decreased rapidly and saturated because of the relatively high background pressure of 10^{-6} Torr, which may have contained a substantial part of oxygen.

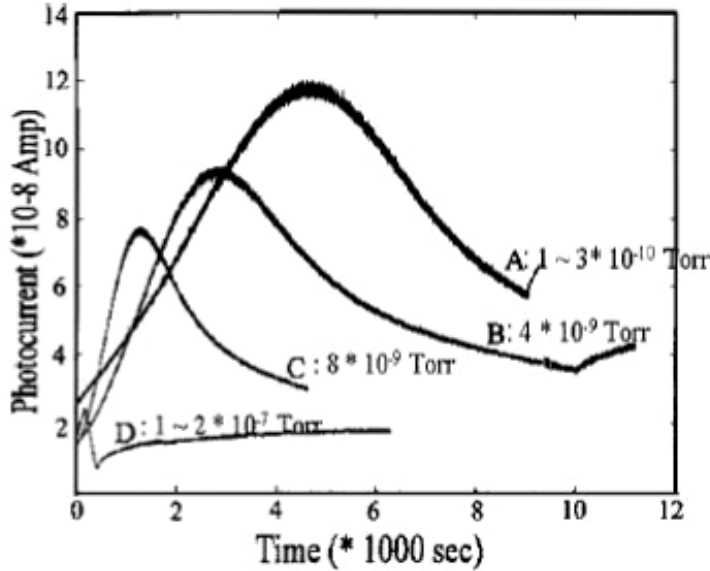


Figure 34: Photocurrent from magnesium versus time of oxygen uptake at different oxygen partial pressures. At lower pressures, the highest peak photocurrent value is obtained.

5.1.3. Response time, linear and non-linear QE response

To obtain higher QE's, in general one can exploit the non-linear response of photocathodes at high laser intensities. In this section, the relation between response time and QE response is discussed as function of intensity.

Excited electrons can lose their energy via collisions with electrons or phonons. In case of low intensities (or electron temperatures) for which the QE response is linear, the relaxation time of excited electrons in metals, which is the time until the hot electrons have returned to the Fermi level, mainly depends on the scattering time of electron-electron collisions. At high pulse intensities, electrons are in addition thermally excited. The relaxation time now also includes the cooling time, the time until the electron temperature is in equilibrium with the lattice temperature, that mainly depends on the electron-phonon collisions.

To more detail: at low laser intensities the excited electrons in metals lose on average half their energy per collision and thereby excite electrons from below the Fermi level to higher unoccupied states [83]. If the gained energy of the first electron is less than the work function, both this and the secondary electron have not enough energy left to escape into vacuum. Thus for photoemission at low intensities the scattering time (lifetime) is important. The lifetime of these electrons is given by Fermi Liquid Theory [84], [85]

$$\tau = \tau_0 \left[\frac{E_F}{E - E_F} \right]^2$$

where $E - E_F$ is equal to the photon energy $h\nu$ and E_F is the Fermi energy, which is 7 eV for copper and 7.08 eV for magnesium¹³. τ_0 is 2 fs for copper. For magnesium the value will most likely be smaller, since calculations of Campillo et al. showed smaller lifetimes for magnesium than for copper. From the FLT and other approximations [86], [87], it follows that the lifetime decreases with electron energy. At energies of 4.64 eV the lifetime of non-thermal electrons is only a few fs. Since τ is smaller for Mg compared to Cu, one could expect a reduced QE for Mg instead of Cu. However, the low work function compensates in favour of Mg.

Because the relaxation time of the excited electrons in metals at this energy is shorter than the laser pulse duration (at least few tens of fs), the length of the laser pulse will determine the response time of the photocathode, and the photocathode is not the limiting factor. If the relaxation time is larger, as is the case with semiconductors, the response time will be independent of the laser pulse length. Therefore, a metallic photocathode is a requisite for initially ultra short (tens fs) electron bunches.

The electron temperature is constant when applying this low laser intensity. Papadogiannis et al. investigated electron emission from several metallic photocathodes, including Cu, with high intensity 450 fs 248 nm laser pulses [85], [88]. They found a non-linear photoelectron current response at high intensity laser pulses (see Figure 35), which is the effect of non thermal-equilibrium between the electron gas and the lattice.

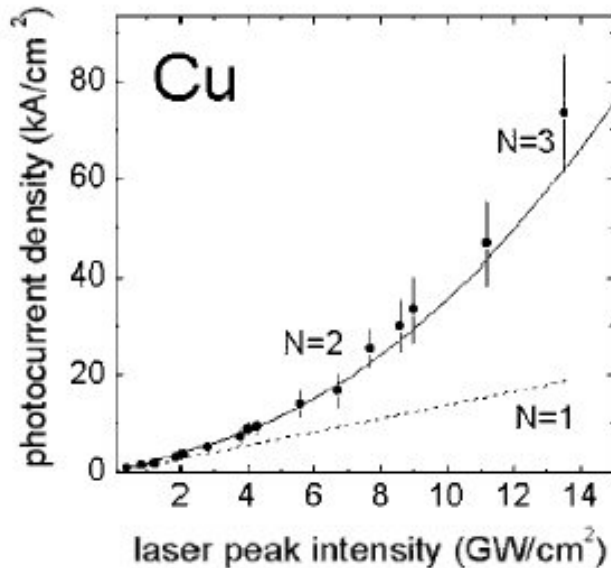


Figure 35: Non-linear QE response for Cu at high intensity laser pulses.

Electrons are excited and thermalize rapidly (typically to a few thousands Kelvin) due to the fast electron-electron scattering time. Heating of the Fermi electrons induces an increased occupancy at higher intensities and results in an enhancement of electron emission. Due to electron-phonon scattering the electron

¹³ <http://hyperphysics.phy-astr.gsu.edu/hbase/tables/fermi.html#c1>

temperature reaches the lattice temperature typically after a picosecond. The electron peak temperature increases with laser peak intensity. The electron-phonon scattering time decreases with the laser intensity and thus with the electron temperature, but the cooling time increases, because a greater amount of electron energy requires more collisions to be transferred to the lattice [85]. This affects the length of the electron bunch that as a result increases. Additionally, space charge effects may occur with consequently electron energies of several hundreds eV are detected [85], [89], [90].

The non-thermal electrons are of no significance compared to the thermal ones in the longer-pulse case. They are important in the case where the laser pulse duration is less than a few hundreds of fs [84], [91]. The effect of few tens fs high intensity pulses on the QE and response time of Mg is unknown. This would be an interesting item of research.

This thermally assisted nonlinearity of the metallic photocathodes investigated by Papadogiannis et al. sets in at intensities higher than $\sim 1 \text{ GW/cm}^2$. For Mg this value is unknown. Endo et al. performed experiments with high intensity 100 fs UV laser pulses [64] and found a non-linear increase in QE above intensities of 80 GW/cm^2 , which seems very high, but for that matter, they did not obtain the expected QE's.

With these high pulse intensities, one cannot exclude the effect of multi-photon photoemission. Multi-photon photoemission also results in a nonlinear response. We suggest two alternative methods to produce high charge electron bunches without the use of high power ultra short UV laser pulses, which are it is difficult to produce. The first method is to make use of the multi photon photoemission by illuminating the Mg photocathode a high intensity IR laser pulses directly from the Ti:Sapphire laser system (about 1.5 eV photons). The advantages are that it is reasonably simple to make these high intensity laser pulses, and the electron bunch length will be shorter than the laser pulse approximately by a factor of \sqrt{n} , in which n is the minimum number of photons required to overcome the work function [41], in this case n equals 3. The disadvantage is that it requires higher intensities to have equivalent QE compared to UV pulses.

The second alternative is to increase the photoelectron current by initially heating the photocathode with a long or relative high intensity IR laser pulse and subsequently irradiate the photocathode with UV laser pulses of reasonable intensity within the cooling time of the electrons.

5.1.4. Conclusions

We consider Mg photocathodes to be the best candidate for use in LWFA. In the linear response regime, Mg has a response time of a few fs at photon energies of 4.64 eV (the third harmonics of a Ti:Sapphire laser), and thus is capable for generation of ultra short electron bunches. In addition, it has the highest QE for metallic photocathodes that can be further increased with several methods. For example by using laser light with shorter wavelength, performing laser cleaning, applying a higher electric field, by making the field enhancement factor β higher (e.g. by roughening of the surface) or lowering the work function by adsorption of

oxides. The most effective method is laser cleaning, which increases the QE by one order of magnitude. However, all these actions in favour of the QE will slightly increase the thermal emittance of the electron bunch. The only factor that increases the QE but not the emittance is the factor A , which depends on the material properties, and the polarisation and angle of incidence of the laser light. A realisable method to decrease the emittance is to use fs pulses instead of ps pulses.

The QE can be non-linearly increased by applying high intensity laser pulses. This thermally assisted QE response also increases the response time and emittance of the photocathode, however the exact influence has to be studied.

The lifetime of laser cleaned Mg photocathodes is respectable in the order of months. An additional advantage of Mg over Cu is that with the former photocathodes lower intensity laser pulses are required to obtain the same charge or current, so that the total energy load on the cathode and the emittance are less. Because higher charges can be extracted, it offers better perspective for further research. Since sputtered Mg showed a high damage threshold than bulk Mg, we choose to deposit Mg on a substratum.

Thus, we conclude that Mg is the best photocathode for use in the LWFA project. To obtain the best QE we also want to perform laser cleaning. A test setup, which will be discussed in the next section, is designed in which we can prepare the photocathode, perform laser cleaning and illuminate it with UV laser pulses to extract electrons and measure the charge and kinetic energy.

5.2. Magnesium photocathode test preparation chamber

For practical reasons we choose to deposit magnesium on a substratum by the evaporation process. It is an easy and low cost preparation process. It is expected that with this Physical Vapour Deposition method no breakdown of the magnesium photocathodes occurs at high RF fields. The advantage is that new layers can easily be deposited after several laser-cleaning procedures without breaking the vacuum. In addition, the layer thickness can be varied easily. The thickness influences the thermal conduction of the photocathode and thus the non-linear thermally assisted photoemissive properties. These effects can be studied. The preparation conditions and performances of the new Mg photocathode will be tested in a test preparation chamber. A standard cross chamber with a connector flange and a turbo pump are used as a basis. New components are designed and integrated to obtain the test setup presented in Figure 36 and Figure 37. The essential components are discussed separately in the following paragraphs.

In order to safely use the magnesium powder an inventory of risks and a protocol of handling have been written, which can be found in Appendix 4.

5.2.1. Physical Vapour Deposition

Besides the many advantages of evaporation, a disadvantage is the non-uniform layer thickness distribution. This might have an effect on the emittance and the laser cleaning process. In general, this non-uniformity is reduced by rotating the substratum, which requires an extra rotational setup, or by putting multiple sources around the substratum. A more simple method is suggested here: multiple

‘point’ sources in a single container. The geometry of the sources depends on the application and the shape of the substratum. In our case, the substratum is a flat circular area of almost 1 cm radius that requires a uniform deposited photocathode layer.

The thickness distribution in 2D for a flat substratum perpendicular to a point source is given by the following formula¹⁴:

$$d = \frac{M_e \cos \theta}{\rho \cdot 4\pi r^2} = \frac{M_e h}{4\pi \rho (h^2 + l^2)^{3/2}}$$

where M_e is the evaporated mass, ρ is the density of the material, h the distance between the source and substratum and l is the position on the substratum with respect to the center. This formula is rearranged for 3D and thickness profiles have been calculated with Maple for several configurations. The thickness deviation is defined as the relative difference between the maximum and minimum value. The greatest effect on uniformity is obtained when the source with multiple holes is placed at a small distance (h is 1 cm) from the substratum. The smallest deviation is obtained for multiple holes positioned in a circle with radius r is 1 cm, without a centre hole.

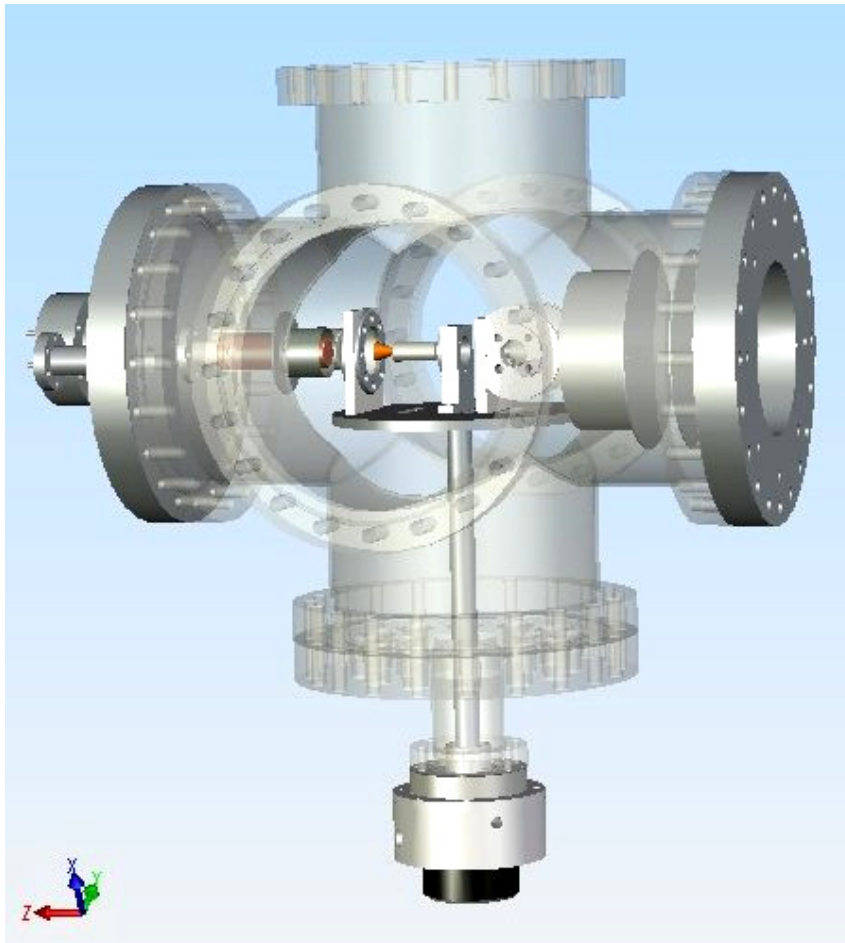


Figure 36: Magnesium photocathode test chamber.

¹⁴ <http://www.uccs.edu/~tchriste/courses/PHYS549/549lectures/evap.html>

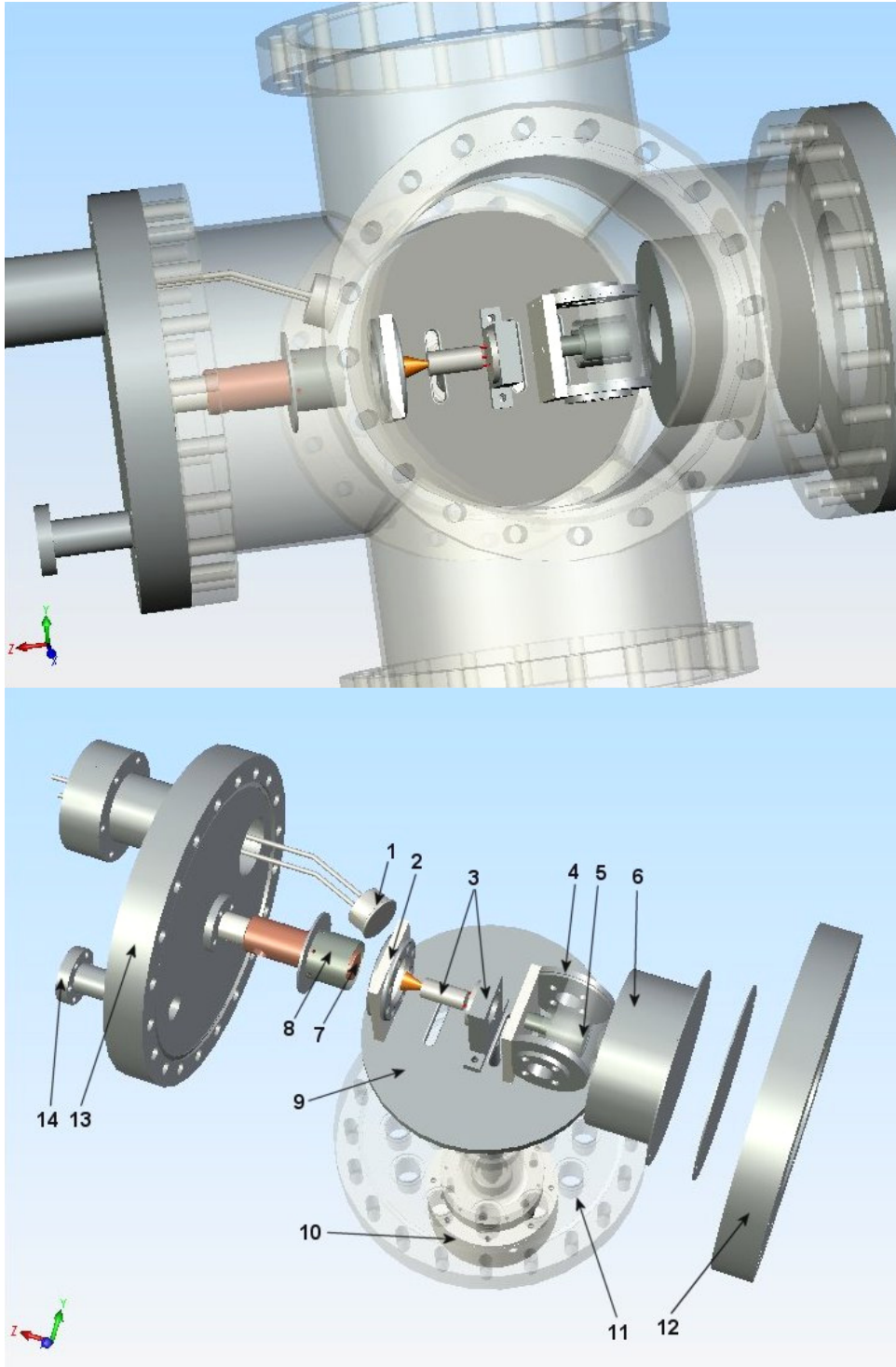


Figure 37: Top views of the magnesium photocathode test chamber. The various elements indicated are described in the text. 1) Microbalance. 2) Two wire grating meshes in a ceramic holder. 3) Channeltron and holder. 4) Screening for 5) container holding Mg powder heated by a heater coil. 6) Dump for evaporated magnesium. 7) Cathode. 8) Screening. 9) Rotating table connected to the 10) turning handle via a rod. 11) Flange containing the connectors. 12) Flange for the pump. 13) Flange to fasten the microbalance, cathode and the 14) connector for the cathode plug.

5.2.2. Evaporation source

The construction for the evaporation and deposition of magnesium is similar to the one that is used in the Cs₂Te preparation chamber so that it can be inserted in that system after tests have been performed successfully. Horizontal deposition will be performed with a heated container filled with Mg powder that is closed with a cover. A cylindrical Molybdenum container of 2 cm length and 1.8 cm radius is used to store the Mg powder. It is attached to a ceramic (Macor) support via a Mo rod. Two covers are available; one with 8 holes and one with a single hole in the middle.

Since a rather thick layer will be deposited and the minimum thickness deviation is obtained for r around 1 cm, the required container would be rather large. This means that a large heating coil is required. Consequently, the material inside the container may not be heated homogeneously. A smaller container will avoid these problems.

The laser spot that illuminates the photocathode will be a few mm², so a uniform area of 0.5 cm radius is sufficient. The outer area serves as an extra collector of evaporated material in order to prevent contamination of the vacuum chamber. Since it is impractical to put the source close to the substratum for diagnostic reasons, we have chosen a distance of 2 cm. In this way, direct heating of the substratum by radiation from the evaporation source is reduced and possible ellipsometry measurements can be performed. However, the advantage of a more uniform layer thickness is reduced. With the value of r set at 0.55 cm, the layer thickness deviation at 0.5 cm radius of the substratum is less than 7%, which is slightly smaller than a single point source. The main improvement by using this round configuration with 8 holes is that the deposition time will be decreased by roughly a factor of 7, or alternatively a lower evaporation temperature can be used.

A Thermocoax heater wire¹⁵ of 2 mm diameter and 70 cm length is wound to make a single heater coil around the Mo container. The total ohmic resistance would be 2.3 Ω, close to the optimal resistance¹⁶. The actual value is 2.18 Ω.

Around the heater wire a stainless steel shield is placed to confine radiation heat and to fix the cover to the container. Calculations on heat transfer have been made to estimate the electrical power needed to keep the container with Mg powder at a constant temperature of 500 °C. This temperature will be sufficient to obtain a reasonable vapour pressure and thus evaporation rate of magnesium. The available power is largely enough for this purpose.

The Mo container with heater wire and shield is placed in the second housing (similar to the construction for Cs₂Te photocathodes) to shield thermal radiation (half of the electrical power is required to maintain the container at a constant temperature). The screening contains two openings to direct the Mg deposition to the substratum with the intention that a smaller area of the chamber is contaminated with Mg, and at the same time the deposition rate can be monitored with a microbalance.

¹⁵ Thermocoax ZEZ I 20/10-70-10.

¹⁶ The connectors to the vacuum chamber can take a current up to 7 A. The maximum voltage that the power supplies can deliver is 18 V. That means that with a resistance of 2.57 Ω the maximum power of 126 W can be transferred.

A thermocouple of type K is used to measure the temperature of the container, which is assumed to be equal to the temperature of the Mg powder. The container is brought to its operating temperature away from the cathode and placed in front of it when the evaporation rate is stable.

5.2.3. *Cathode*

A copper or molybdenum cathode plug is used as substratum, which has the same shape as the existing Mo cathode used for Cs₂Te photocathodes, so that it is interchangeable with the one in the preparation chamber which is connected to the Linac.

For the cathode in the new setup, we have chosen to use the same connector that is used for the cathode in the Cs₂Te preparation chamber. It is connected to a power supply for the heater, to a thermocouple and to the battery that sets the cathode at a negative voltage of -90 V. A heater wire from Thermocoax¹⁷ is wound inside the cathode with a resistance of 3.7 Ω. A thermocouple is point welded to a Mo plate that is fixed inside the cathode.

A screening is fixed around the cathode to shield the microbalance that is placed next to the cathode.

5.2.4. *Thickness measurements*

The microbalance¹⁸ is used to monitor the deposition rate and layer thickness of the Mg layer. It contains a piezo-crystal that is driven by an oscillator. When matter is deposited onto this crystal, the oscillation frequency changes. The resonance frequency changes with mass, therefore the deposition rate can be retrieved when this resonance frequency is recorded with time. From this effect the evaporation rate and grown thickness can be calculated. To use the microbalance at high temperatures due to thermal radiation we have chosen a bakeable crystal sensor, which is cooled with water.

First, the evaporation rate of Mg at different temperatures has to be determined. The growth of evaporated Mg films depends on the evaporation rate [77]. A growth rate of 1–2 Å/s resulted in a uniform continuous film, whereas islands were formed at higher deposition rates of 5–15 Å/s. The strongest orientation was (001), which could be the orientation of the substratum. Therefore, the evaporation rate must not be too high.

The microbalance is positioned next to the cathode at the same distance from the source if it is turned towards the microbalance. A calibration of the deposition rate will be made to relate the measurement on deposition in the two orientations of the evaporation container: towards the cathode and towards the microbalance.

¹⁷ Thermocoax SEI 15/50.

¹⁸ DeMaCo CSH-275-1-W Bakeable crystal sensor 178 cm long and bend; CM-2 Deposition Monitor.

5.2.5. Laser system and electron detection

The third harmonic UV laser pulses from a Ti:Sapphire laser, which is also used for the LWFA project, is used to illuminate the photocathode at an angle of around 70 degrees. At one side of the chamber a fused silica viewport is mounted that transmits UV light. The other windows are normal glass windows.

The photoelectrons will be collected and measured by a small Channeltron¹⁹. This electron multiplier can detect single electrons or pulses as well as currents up to a few μA . Its maximum operating voltage is 3 kV. It is connected to the high voltage connector in the connector flange at the bottom of the cross. The front of the Channeltron is at zero voltage.

A double wire grating mesh²⁰ is used to accelerate the emitted electrons from the photocathode towards the Channeltron. They are mounted to an insulated ceramic holder. The transmission is 83.2 %. The first wire mesh is kept at -80 V, i.e. 10 V above the cathode voltage. The potential of the second mesh can be varied. If it is set at a higher potential, the normal current or charge can be measured. A density plot of the kinetic energy can be plotted when the potential is more negative than -80 V, because electrons of specific kinetic energy are filtered out. In this way, the kinetic energy can be measured roughly from extracted electrons at low and high intensity laser pulses (the linear and non-linear response respectively) and a distinction can be made in the non-linear regime between a thermally assisted single photon process and a multiphoton process.

5.2.6. Additional components

The Mg container and double wire mesh-channeltron combination are placed on a rotating table, which can be rotated by a handle below the bottom connector flange. Slits are milled out to lead the insulated electrical and thermocouple wires to the connectors.

A turbo pump²¹ is used to put the system to vacuum (around high 10^{-8} to 10^{-7} Torr) and is placed on the opposite flange of the cathode. The Mg source is heated up and cooled down in front of an evaporation dump. In this way the redundant evaporated Mg remains out of the vacuum system without directly getting in the pump.

In Figure 38 and Figure 39 the actual test chamber and the components inside are shown. The first test measurements will be performed in the near future. A number of additional recommendations for further experiments are made in Appendix 5.

¹⁹ Burle Industries CEM 4869 COA MTD on Flange PN 30135.

²⁰ RVS 304, 80 mesh per inch, wire diameter 0.028 mm, wire spacing 290 μm .

²¹ Balzers TPH 330; 300 l/s pump capacity.

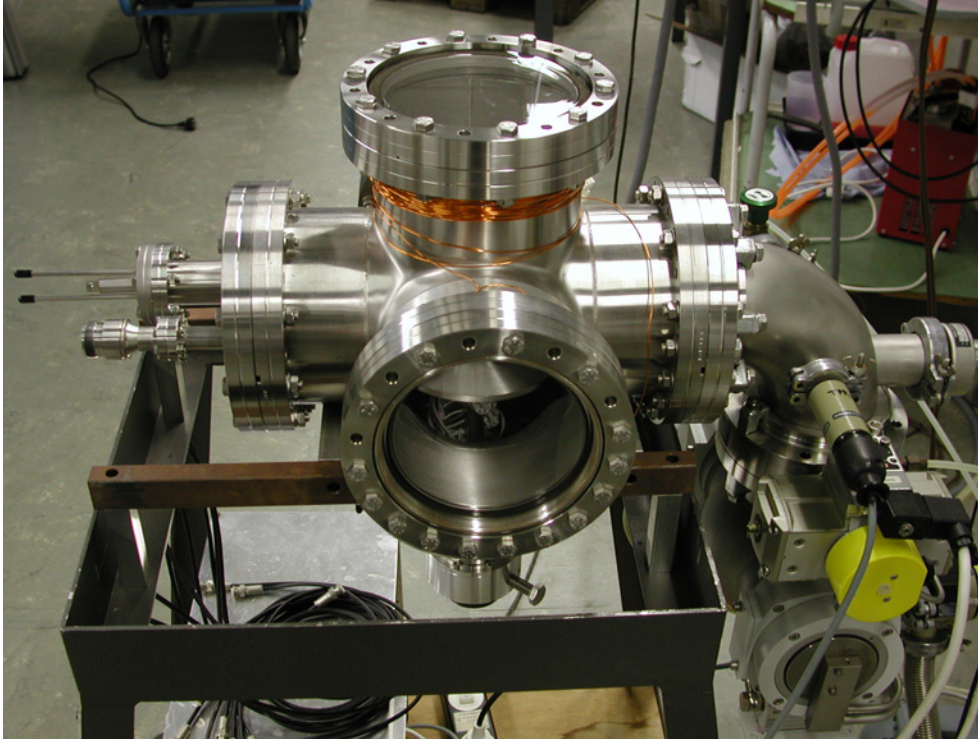


Figure 38: View of the actual Mg test preparation chamber.

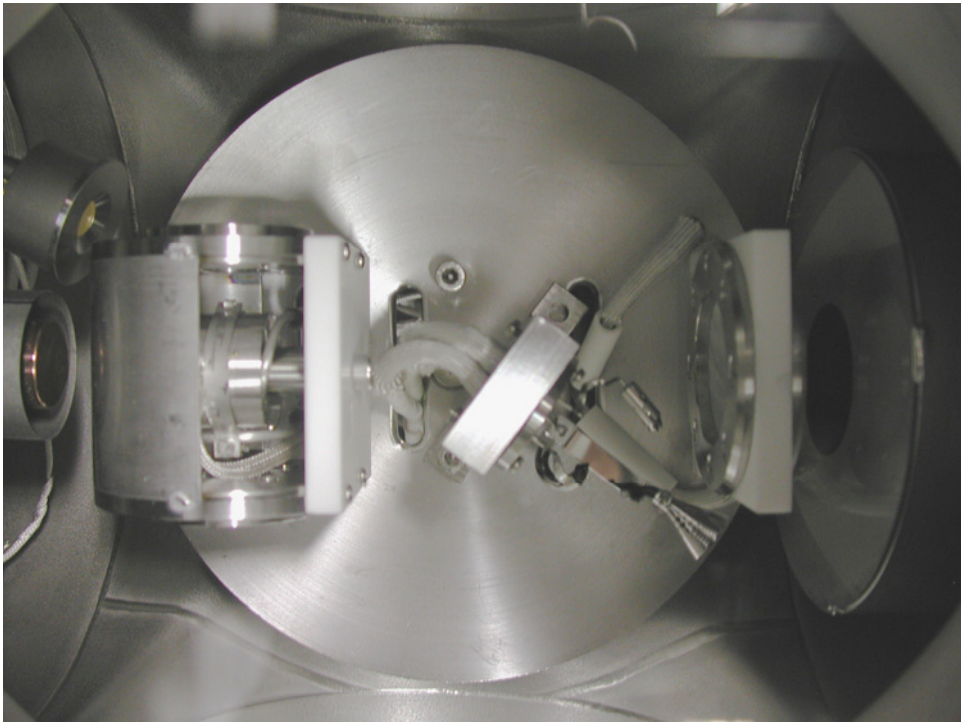


Figure 39: Inside views of the Mg test preparation chamber. On the left, the cathode and microbalance. In front of it, the container holding the Mg powder. The Channeltron in the middle is currently not yet mounted correctly.

6. Conclusions

We described the research performed on two most promising photocathode materials for two goals:

1. We investigated semiconductor Cesium-Telluride (Cs-Te) photocathodes for use in standard RF driven electron accelerators. Here, the objective is to provide high quantum efficiency (QE) photocathodes with a long lifetime under operational conditions of high average beam load, while moderate (ps) length of the generated electron bunches is sufficient. These investigations contribute to research within a large international program of the EU (PHIN-CARE) on photoinjectors for large-scale accelerators.
2. We investigated metallic magnesium photocathodes for use in novel types of accelerators, such as a laser driven plasma based accelerators (laser wakefield accelerators). Here, the objective is to provide ultra-short (femtosecond) electron bunches using a high QE photocathode having a long lifetime. These investigations contribute to a research within a national program of the Dutch Science Foundation (FOM, program 55 on laser wakefield accelerators).

Cesium-Telluride

By comparing the properties of Cs-Te (often termed Cs₂Te) photocathodes from various groups we conclude that the preparation process is the most critical and important parameter that affects the performance of these photocathodes. In particular, we conclude that such photocathodes can be improved with respect to lifetime and maximum beam load when the preparation time is longer. On the other hand, if a higher QE is required, the preparation time should be short, for example by increasing the Cs deposition rate. However, this would impose limits on lifetime and the maximum extractable charge per electron bunch.

We further conclude that the change of QE by alteration of the preparation conditions can be addressed to the formation of various stoichiometric compounds of Cs-Te. We implemented this conclusion in a model to explain the photocurrent behaviour during preparation and the spectral response. Specifically, we predict that the lifetime of Cs-Te photocathodes can be further improved if the preparation procedure is stopped before the maximum photocurrent measured during Cs deposition is reached, instead of stopping at the maximum.

Now the data of various groups that make Cs-Te photocathodes are successfully brought together in a model that describes the build up of these photocathodes. There is a need for good diagnostics to verify this model. Apart from a deposition rate monitor, we suggested two promising techniques: XPS and single wavelength ellipsometry (SWE). For a first experimental proof of these predictions, we performed a preliminary XPS measurement on a photocathode. The results confirm, qualitatively, the presence of different Cs-Te phases compared to what has been reported. To make the XPS technique applicable, preferably in situ, in order to draw quantitative conclusions, extra research is needed to obtain more data about the binding energies from XPS measurements and the relation with corresponding stoichiometric phases of Cs-Te.

For second experimental proof that should allow quantitative, much more detailed information, and in particular, the possibility of online monitoring during preparation, we designed and constructed a diagnostic monitoring device. This device was based on SWE and was successfully implemented inside our existing preparation chamber. Based on initial tests of the device, we expect in the near future to distinguish between various stoichiometric Cs-Te compounds and their growth sequence. In particular, we expect that this approach, which should be easily installable also in other existing preparation chambers of various research groups, would allow for the first time to monitor the influence of specific preparation conditions on the type of Cs-Te that are obtained. Finally, this will lead to a better understanding of the preparation process and an improved control during deposition of the Cs-Te photocathodes.

Magnesium

From our extensive literature research we conclude that magnesium has the best properties for laser wakefield accelerators. It has an ultra-short response time (in the order of fs) and has the highest QE of metallic photocathodes. The QE can be further increased effectively by one order of magnitude by applying laser cleaning. Because of the high QE, low intensity laser pulses are sufficient to produce the required charges for injection in a plasma channel. A preparation chamber is designed to test the preparation and performances of vapour deposited magnesium. The main advantages of vapour deposited magnesium are that it is an easy and low cost preparation process, new layers can easily be deposited after several laser-cleaning procedures without breaking the vacuum and the layer thickness can be easily varied to study non-linear thermally assisted photoemissive properties of magnesium. We expect that test measurements in the near future will prove that magnesium is a superior photocathode for laser driven plasma based accelerators.

References

- [1] S.H. Kong et al., Photocathodes for free electron lasers, *Nuclear Instruments and Methods in Physics Research A* 358, 272 (1995).
- [2] A.G. Khachatryan et al., Extremely short relativistic-electron-bunch generation in the laser wakefield via novel bunch injection scheme, *Physical Review Special Topics – Accelerators and Beams* 7, 121301 (2004).
- [3] R.A. Powell et al., Photoemission Studies of Cesium Telluride, *Physical Review B*, Vol.8, No.8, 3987 (1973).
- [4] A.H. Sommer, *Photoemissive materials. Preparation, Properties and Uses*, New York, John Wiley & Sons, Inc. (1968).
- [5] R.U. Martinelli and D.G. Fisher, The Application of Semiconductors with Negative Electron Affinity Surfaces to Electron Emission Devices, *Proceedings of the IEEE*, Vol. 62, No. 10, 1339 (1974).
- [6] W.E. Spicer, Negative Affinity 3-5 Photocathodes: Their Physics and Technology, *Applied Physics* 12, 115 (1977).
- [7] K.L. Jensen et al., Measurements and analysis of thermal photoemission from a dispenser cathode, *Physical Review Special Topics - Accelerators and Beams* 6, 083501 (2003).
- [8] I. Boscolo and P. Michelato, Photocathodes: the state of the art and some news, *Nuclear Instruments and Methods in Physics Research A* 445, 389 (2000).
- [9] I. Boscolo et al., Ferroelectric Ceramics - A Novel Efficient and Robust Photocathode, *LINAC'98 Conference Proceeding*, 180 (1998).
- [10] T. Srinivasan-Rao et al., Sputtered magnesium as a photocathode material for rf injectors, *Review of Scientific Instruments*, Vol 69, No. 6, 2292 (1998).
- [11] J.P. Girardeau-Montaut et al., Ultrafast photoelectric emission from new solid materials, *Applied Surface Science* 106, 451 (1996).
- [12] M. Afif et al., Ultrashort electron emission improved by alkali ions implantation into metallic photocathodes, *Applied Surface Science* 111, 241 (1997).
- [13] K. Zhao et al., Researches on new photocathode for RF electron gun, *Nuclear Instruments and Methods in Physics Research A* 445, 394 (2000).
- [14] C.D. Gelatt Jr and H. Ehrenreich, Charge transfer in alloys: AgAu, *Physical Review B*, Vol 10, No. 2, 398 (1974).
- [15] R. Ishii et al., Work function of binary alloys, *Applied Surface Science* 169-170, 658 (2001).
- [16] V.G. Tkachenko et al., Photoemissive properties of binary magnesium-barium and aluminium-lithium metallic alloys, *Applied Physics A* 62, 285 (1996).
- [17] S.H. Kong et al., Performance of cesium telluride photocathodes as an electron source for the Los Alamos Advanced FEL, *Nuclear Instruments and Methods in Physics Research A* 358, 284 (1995).

- [18] D. Sertore et al., First operation of cesium telluride photocathodes in the TTF injector RF gun, *Nuclear Instruments and Methods in Physics Research A* 445, 422 (2000).
- [19] P. Michelato, Photocathodes for RF photoinjectors, *Nuclear Instruments and Methods in Physics Research A* 393, 455 (1997).
- [20] D. Bisero et al., High efficiency photoemission from Cs-K-Te, *Applied Physics Letters* 70 (12), 1491 (1997).
- [21] S.H. Kong et al., Fabrication and characterization of cesium telluride photocathodes: A promising electron source for the Los Alamos Advanced FEL, *Nuclear Instruments and Methods in Physics Research A* 358, 276 (1995).
- [22] A. Fry et al., Experience at Fermilab with high quantum efficiency photocathodes for RF electron guns, *LINAC'98 Conference Proceeding*, 642 (1998).
- [23] J. Teichert et al., Report on photocathodes (2004).
- [24] D. Bisero et al., K₂Te photocathode growth: A photoemission study, *Journal of Applied Physics*, Vol. 87 (1), 543 (2000).
- [25] D. Bisero et al., K-Te photocathodes: A new electron source for photoinjectors, *Journal of Applied Physics*, Vol. 82, No. 3, 1384 (1997).
- [26] D. Bisero et al., Photoemission from K-Te photocathodes, *Applied Physics Letters* 69 (24), 3641 (1996).
- [27] E. Chevallay et al., Photo-cathodes for the CERN CLIC test facility, CLIC Notes 1998.
- [28] D. Bisero et al., Cs-K-Te photo cathodes: a promising electron source for free-electron lasers, *Nuclear Instruments and Methods in Physics Research A* 407, 311 (1998).
- [29] J.W.J. Verschuur et al., Aspects of accelerator-based photoemission, *Nuclear Instruments and Methods in Physics Research B* 139, 541 (1998).
- [30] A. Buzulutskov et al., The protection of K-Cs-Sb photocathodes with CsBr films, *Nuclear Instruments and Methods in Physics Research A* 400, 173 (1997).
- [31] A.R.H.F. Ettema, Li₂CsSb: A highly-efficient photocathode material, *Applied Physics Letters*, Vol. 82, No. 22, 3988 (2003).
- [32] D. Vouagner and J.P. Girardeau-Montaut, Picosecond laser-induced ultrashort electron emission from carbon-based photocathodes, *Thin Solid Films* 453-454, 22 (2004).
- [33] I. Boscolo et al., Photoemission from diamond films illuminated by intense Nd: YAG laser harmonics, *Applied Physics A* 77, 805 (2003).
- [34] Q.F. Zhang et al., A new internal field-assisted photocathode based on Ag-O-Cs composite thin films, *Solid State Communications* 122, 515 (2002).
- [35] A. Buzulutskov et al., Protection of cesium-antimony photocathodes, *Nuclear Instruments and Methods in Physics Research A* 387, 176 (1997).
- [36] A. Breskin et al., Removable organic protective coating for alkali-antimonide photocathodes, *Nuclear Instruments and Methods in Physics Research A* 413, 275 (1998).
- [37] E. Shefer et al., Coated photocathodes for visible photon imaging with gaseous photomultipliers, *Nuclear Instruments and Methods in Physics Research Section A* 433, 502 (1999).

- [38] D.C. Nguyen et al., First lasing of the regenerative amplifier FEL, *Nuclear Instruments and Methods in Physics Research A* 429, 125 (1999).
- [39] E. Chevallay et al., Production and studies of photocathodes for high intensity electron beams, *LINAC'00 Conference Proceeding*, 110 (2000).
- [40] I. Boscolo et al., Photoemission from metals covered with a nanostructured carbon film, *Journal of Applied Physics*, Vol.87, No.8, 4005 (2000).
- [41] R. Brogle et al., Studies of Linear and Nonlinear Photoelectric Emission for Advanced Accelerator Applications, *Proceedings of the 1995 Particle Accelerator Applications* (1995).
- [42] I. Ben-Zvi, *Secondary Emission Enhanced Photoinjector* (2004).
- [43] G.B. Fischer et al., A Standard for Ultraviolet Radiation, *Applied Optics*, Vol. 12, No. 4, 799 (1973).
- [44] S.H. Kong et al., Cesium telluride photocathodes, *of Applied Physics*, Vol. 77, No. 11, 6031 (1995).
- [45] A. di Bona et al., Auger and x-ray photoemission spectroscopy study on Cs₂Te photocathodes, *Journal of Applied Physics*, Vol. 80, No. 5, 3024 (1996).
- [46] P. Michelato et al., Characterization of Cs₂Te photoemissive film: formation, spectral responses and pollution, *Nuclear Instruments and Methods in Physics Research A* 393, 464 (1997).
- [47] G. Ferrini, P. Michelato and F. Parmigiani, A Monte Carlo simulation of low energy photoelectron scattering in Cs₂Te, *Solid State Communications*, Vol. 106, No. 1, 21 (1998).
- [48] H. Trautner, *Spectral Response Cesium Telluride* (2000)
- [49] P. Michelato, D. Sertore and S. Betonni, Optical Properties of Cesium Telluride, *Proceedings of EPAC 2002*, 1810 (2002).
- [50] S.M. Johnson, Jr., Ultraviolet angular response of cesium-telluride photocathodes, *Applied Optics*, Vol. 31, No. 13, 2332 (1992).
- [51] B. van Oerle, *A High Brightness Electron Beam for Free Electron Lasers* (1997).
- [52] E. Chevallay, G. Suberlucq and H. Trautner, Production of a high average current electron beam with Cs-Te photocathodes, *CTF3 Note 020* (2001).
- [53] S. Valeri et al., Growth and morphology of Te films on Mo, *Thin Solid Films* 352, 114 (1999).
- [54] P. Michelato et al., Cs₂Te photocathode for the TTF Injector II, *Proceedings of the European Particle Accelerator Conference 1996*, 1510 (1996).
- [55] I.V. Volokhine, *Design and Numerical Analysis of TEU-FEL II* (2003).
- [56] G. Suberlucq, Technological Challenges For High Brightness Photo-Injectors, *Proceedings of EPAC 2004*, 64 (2004).
- [57] M. Ohring, *Materials Science of Thin Films*, Second Edition, San Diego, Academic Press (2002).
- [58] Karakterisatie van Oppervlakken en Dunne Films, *Lecture Notes* (2001).
- [59] H.G. Tompkins, *A User's Guide to Ellipsometry*, Boston, Academic Press, Inc. (1993). H.G. Tompkins and W.A. McGahan, *Spectroscopic Ellipsometry and Reflectometry*, New York, John Wiley & Sons, Inc. (1999).
- [60] E. Hecht, *Optics*, Third Edition, Reading, Addison Wesley Longman, Inc. (1998).

- [61] F.L. McCrackin, A Fortran Program for Analysis of Ellipsometer Measurements, *National Bureau of Standards Technical Note 479* (1969).
- [62] T. Srinivasan-Rao et al., Photoemission studies on metals using picosecond ultraviolet laser pulses, *Journal of Applied Physics*, Vol. 69 (5), 3291 (1997).
- [63] L. Serafini, R. Zhang and C. Pellgrini, Generation of sub-picosecond electron bunches from RF photoinjectors, *Nuclear Instruments and Methods in Physics Research A* 387, 305 (1997).
- [64] A. Endo et al., Photoelectron generation by femtosecond UV laser, *EPAC'96 Conference Proceedings* (1996).
- [65] J. Fischer et al., Photoemission from magnesium and from diamond film using high intensity laser beams (abstract), *Nuclear Instruments and Methods in Physics Research A* 340, 190 (2002).
- [66] Z.M. Yusof, Schottky-enabled photoemission in a rf accelerator photoinjector: Possible generation of ultralow transverse thermal-emittance electron beam, *Physical Review Letters*, Vol. 93 No. 11, 114801 (2004).
- [67] X.J. Wang et al., Measurements on photoelectrons from a magnesium cathode in a microwave electron gun, *Nuclear Instruments and Methods in Physics Research A* 356, 159 (1995).
- [68] T. Srinivasan-Rao et al., Photoemission from Mg irradiated by short pulse ultraviolet and visible lasers, *Journal of Applied Physics*, Vol 77 (3), 1275 (1995).
- [69] T. Srinivasan-Rao et al., Performance of magnesium cathode in the S-Band RF Gun, *1997 Particle Accelerator Conference IEEE*, 2790 (1998).
- [70] X.J. Wang et al., S-Band High Duty Photo-injection System, *Proceedings of EPAC 2002*, 1822 (2002).
- [71] X.J. Wang et al., Mg cathode and its thermal emittance, *LINAC'02 Conference Proceedings*, 142 (2002).
- [72] H. Iijima et al., High charge Mg photocathode RF Gun in S-Band Linac, *Proceedings of EPAC 2002*, 1771 (2002).
- [73] R. Kuroda et al., Characterization of electron beam from a Mg photocathode RF Gun system, *Proceedings of EPAC 2002*, 1783 (2002).
- [74] J.F. Schmerge et al., Emittance and Quantum Efficiency Measurements from a 1.6 Cell S-Band Photocathode RF Gun with Mg Cathode, *Proceedings of the 2004 FEL Conference*, 205 (2004).
- [75] D.T. Palmer, A Review of Metallic Photocathode Research (2002).
- [76] T. Nakajyo et al., Quantum Efficiencies of Mg Photocathode under Illumination with 3rd and 4th Harmonics, *Japanese Journal of Applied Physics*, Vol. 42, 1470 (2003).
- [77] Q. Yuan et al., Effect of oxygen adsorption on the efficiency of magnesium photocathodes, *Journal of Vacuum Science Technology B*, Vol. 21 (6), 2830 (2003).
- [78] L. Cultrera et al., PLD of Mg Thin Films on Cu Substrates for Photocathode Application (abstract), *The 4th International Conference on Photo-Excited Processes and Applications* (2004).
- [79] J.A. Nation et al., Advances in Cold Cathode Physics and Technology, *Proceedings of the IEEE*, Vol. 87, No. 5, 874 (1999).

- [80] W.S. Graves et al., Measurement of Thermal Emittance for a Copper Photocathode, *Proceedings of the 2001 Particle Accelerator Conference*, 2227 (2001).
- [81] T. Kobayashi et al., High-Charge S-Band Photocathode RF-Gun and Linac System for Radiation Research, *Journal of Nuclear Science and Technology*, Vol. 39, No. 1, 6 (2002).
- [82] P. Schoessow et al., The Argonne Wakefield Accelerator High Current Photocathode Gun And Drive Linac
- [83] T. Hertel et al., Ultrafast Electron Dynamics at Cu(111): Response of an Electron Gas to Optical Excitation, *Physical Review Letters*, Vol. 76 No. 3, 535 (1996).
- [84] W.S. Fann et al., Electron thermalization in gold, *Physical Review B*, Vol. 46, No. 20, 13592 (1992).
- [85] N.A. Papadogiannis et al., Electron relaxation phenomena on a copper surface via nonlinear ultrashort single-photon photoelectric emission, *Journal of Physics D: Applied Physics*, Vol. 30, 2389 (1997).
- [86] R. Keyling, W.D. Schone and W. Ekardt, Comparison of the lifetime of excited electrons in noble metals, *Physical Review B*, Vol. 61, No. 3, 1670 (2000).
- [87] I. Campillo et al., First-principles calculations of hot-electron lifetimes in metals, *Physical Review B*, Vol. 61, No. 20, 13484 (2000).
- [88] N.A. Papadogiannis, S.D. Moustazis, Ultrashort laser-induced electron photoemission: a method to characterize metallic photocathodes, *Journal of Physics D: Applied Physics*, Vol. 34, 499 (2001).
- [89] C. Girardeau-Montaut and J.P. Girardeau-Montaut, Space charge effect on the energy spectrum of photoelectrons produced by high-intensity short-duration laser pulses on a metal, *Physical Review A*, Vol. 44, No. 2, 1409 (1991).
- [90] G. Farkas and C. Toth, Energy spectrum of photoelectrons produced by picosecond laser-induced surface multiphoton photoeffect *Physical Review A*, Vol. 41, No. 7, 4123 (1990).
- [91] W.S. Fann et al., Direct measurement of Nonequilibrium Electron-Energy Distributions in Subpicosecond Laser-Heated Gold Films, *Physical Review Letters*, Vol. 68, No. 18, 2834 (1992).
- [92] A. Braem et al., Technology of photocathode production, *Nuclear Instruments and Methods in Physics Research A* 502, 205 (2003).
- [93] T. Siggins et al., Performance of a DC GaAs photocathode gun for the Jefferson lab FEL, *Nuclear Instruments and Methods in Physics Research A* 475, 549 (2001).
- [94] F. Machuca et al., Role of oxygen in semiconductor negative electron affinity photocathodes, *Journal of Vacuum Science Technology B* 20 (6), 2721 (2002).
- [95] F. Machuca et al., Oxygen species in Cs/O activated gallium nitride (GaN) negative electron affinity photocathodes, *Journal of Vacuum Science Technology B* 21 (4), 1863 (2003).
- [96] F.S. Shahedipour et al., Efficient GaN Photocathodes for Low-Level Ultraviolet Signal Detection, *IEEE Journal of Quantum Electronics*, Vol. 38, No. 4, 333 (2002).

- [97] K. Batchelor et al., A high current, high gradient, laser excited, pulsed electron gun, *Proceedings of EPAC 1998*, 791 (1998).
- [98] M. Uesaka et al., Generation of femtosecond electron single pulse using laser photocathode RF gun, *Proceedings of APAC 1998* (1998).
- [99] M. Uesaka et al., Experimental Verification of Laser Photocathode RF Gun as an Injector for a Laser Plasma Accelerator, *IEEE Transactions on Plasma Science*, Vol. 28, No. 4, 1084 (2000).
- [100] T. Kobayashi et al., Performance Study of High Current Photo-Cathode RF-Gun with New Laser System, *Proceedings of EPAC 2000*, 1663 (2000).

Appendix 1: Overview of photocathodes

Photocathode material		Work function/ E _{photon} (eV)	QE	λ (nm)	Operational lifetime	Vacuum (Torr)	Response time	Reference	
<i>Metallic</i>									
	Cu	4,3 - 4,7	0,014 %	266	Very long	10 ⁻⁷	< ps	[1]	
	Mg	3,66	0,06 %	266	> 5000 h	10 ⁻⁷	< ps	[1]	
			0,027 %	266				[b*]	
	Mg (laser-cleaned)		0,20 %	266	Long	10 ⁻⁹ - 10 ⁻⁸		[10]	
	Y	2,9	0,05 %	266	Long	< 10 ⁻⁷	< ps	[1]	
	Sm	2,7	0,07 %	266	Long	< 10 ⁻⁷	< ps	[1]	
	Ba	2,5	0,10 %	337	Short-long	< 10 ⁻⁷	< ps	[1]	
	Nb	4	0,01 %	266				[23]	
	Ca	2,9	0,05 %	248				[b*]	
Mg-Ba	low	0,10 %	266				[16]		
<i>Semiconductor</i>									
Alkali-telluride	Cs ₂ Te	3,5	4 - 20 %	251 – 266	Few hours - months	10 ⁻¹⁰ - 10 ⁻⁹	~ ps		
	CsTe +CsBr	4,1	5 - 6 %		> 2 months			[38]	
			1,2 %	266	No difference	10 ⁻⁸		[39]	
	CsKTe	4,0 - 4,5	22,5 % 2 % at saturation	259	T1/2 = 1+12 h Tsat= 20 h Tstor = 100 h	10 ⁻⁹		[20],[28], [29]	
	K ₂ Te	4,5	1,6 %	266					[b*]
			1 - 3%	262					[27]
			2,6 %	254			10 ⁻¹¹		[24]
			4,75 %	259	Long		10 ⁻¹⁰ - 10 ⁻⁹		[25]
			8,3 %						[26]
8,9 %						[20]			
Rb ₂ Te	4,1	4,5 %	266					[b*]	
RbCsTe		7,7 %	266					[b*]	

Photocathode material		Work function/ E_{photons} (eV)	QE	λ (nm)	Operational lifetime	Vacuum (Torr)	Response time	Reference
Alkali-antimonide	K ₂ CsSb	~2	8 %	527	T1/2 < 4 h	10 ⁻¹⁰ - 10 ⁻⁹	~ ps	[1]
			3 %	532	T1/e > 1 h	10 ⁻¹⁰		[19]
			4 %	534	T1/2 < 2 h	10 ⁻⁹		[19], [29]
			6 %	543		10 ⁻¹¹ - 10 ⁻¹⁰		[19]
	KCsSb + CsBr		5 % 10%	312		150 0,1		[30],[37]
	Cs ₃ Sb	2	4 %	527	T1/2 < 4 h	10 ⁻¹⁰ - 10 ⁻⁹	~ ps	[1],[19]
			2 %	266	Very short			[b*]
			0,38 %	532	1 to few hours	10 ⁻⁹		[19]
			1,3 %	532		10 ⁻¹⁰		[19]
			1 - 2%	527				[29]
			9 %	543		10 ⁻¹⁰ - 10 ⁻⁹		[19]
	Cs ₃ Sb + NaI/CsI/HTC		1 %	312				[35],[36]
	K ₃ Sb	2,3	1,6 %	266	Very short			[b*]
			0,023%	523	1 to few hours			
		< 1%	527	Short			[29]	
Na ₂ KSb	2	6,1 %	266	Very short			[b*]	
		0,02 %	532	1 to few hours				
Li ₂ CsSb			100 %	all colors			[31]	
Alkali-halide	CsI	6,3	2 %	209	T1/2 > 150 h	10 ⁻¹⁰ - 10 ⁻⁹	> ps	[1],[b*]
			0,007%	262				
			20 %	180				[92]
	CsI-Ge	5	0,73 % 0,13 %	213 262	T1/e > 1 y (storage)			[27]

Photocathode material		Work function/ E_{photons} (eV)	QE	λ (nm)	Operational lifetime	Vacuum (Torr)	Response time	Reference
NEA	DC GaAs		5 %	527	T1/e = 58 h	$\sim 5 \cdot 10^{-11}$		[93]
	GaAs (Cs)		1.5 - 6%	750	Short	10^{-11}	< ns	[1]
	GaN (CsO)	3,4	20 %	300	10h + T1/2 = 8h	10^{-10}		[94],[95]
	GaN (Cs)	<3.4	30 %	200				[96]
	Diamond	Large	> 1%	< 210	Very long		> ps	[1]
	Polycrystalline diamond		10^{-6}	266	Long			[33]
	Hydrogenated diamond		0,08 %	213		10^{-8}		[32]
	Nanostructured fullerene		0,002%	213		10^{-8}		[32]
Internal field-assisted	Ag-O-Cs, Ag-BaO Cu-O-Cs	Lowered by external bias	15,7% enhanced	510				[34]
<i>Thermionic</i>								
	LaB ₆		0,1 %	355	~ 1 d	$< 10^{-7}$		[1]
	Thermionic dispenser		0,23 %	266	T1/2 = 12 h	$3 \cdot 10^{-10}$	< 380 ps	[1],[7]
	Trioxide thermionic		0,035%	266	T1/2 = 10 h	$3 \cdot 10^{-10}$	< 400 ps	[1]
<i>Ferroelectric</i>								
	Ferroelectric		0,06 %	355	Very long	$10^{(-7)}$	< ns	[1],[8],[9]
	Ferroelectric ceramic		10^{-6}					[8],[9]

Appendix 2: Model diagnostic setup

Determination of the change in delta

Consider again the configuration as in Figure 23. We define the phases and phase differences: $\varphi_{ref}^s, \varphi_{ref}^p, \varphi_i^s, \varphi_i^p, \varphi_{r,Mo}^s, \varphi_{r,Mo}^p, \varphi_{r,f}^s, \varphi_{r,f}^p$ and $\delta_1, \delta_{2,f}, \delta_{2,Mo}$. They are related by:

$$\begin{aligned}\Delta^0 &= \delta_1 - \delta_{2,Mo} \text{ and } \delta_{2,f} = \delta_{2,Mo} + d\Delta \\ \delta_{2,Mo} &= \varphi_{r,Mo}^p - \varphi_{r,Mo}^s \text{ and } \delta_{2,f} = \varphi_{r,f}^p - \varphi_{r,f}^s \\ \Delta &= \delta_1 - \delta_{2,f} = \delta_1 - \delta_{2,Mo} - d\Delta = \Delta^0 - d\Delta \\ \Delta &= \delta_1 - (\varphi_{r,f}^p - \varphi_{r,f}^s) = \delta_1 - (\varphi_{r,Mo}^p - \varphi_{r,Mo}^s) - d\Delta\end{aligned}$$

From this follows that the change in delta:

$$d\Delta = (\varphi_{r,f}^p - \varphi_{r,f}^s) - (\varphi_{r,Mo}^p - \varphi_{r,Mo}^s) = (\varphi_{r,Mo}^s - \varphi_{r,f}^s) - (\varphi_{r,Mo}^p - \varphi_{r,f}^p)$$

Now we define:

$$d\varphi_r^p = \varphi_{r,Mo}^p - \varphi_{r,f}^p \text{ and } d\varphi_r^s = \varphi_{r,Mo}^s - \varphi_{r,f}^s$$

$$\text{So: } d\Delta = d\varphi_r^s - d\varphi_r^p$$

To determine the exact phases is difficult. One has to know the phase of the reference wave. However, we can use only the phase change occurring during the growth of the layer medium 2. The detection of the phase change is done by measuring the resultant intensity of the interfering reflected wave from the film (or Mo substratum) and the reference wave, both for the p and the s wave. In the following, only the equations for the s wave are written out. The same goes for the p wave.

We have a reference beam and a wave coming from the sample with a film of a certain thickness that interfere with each other. For two interfering linearly polarized waves of the form

$$\mathbf{E}_{ref}^s(r, t) = E_{ref0}^s \cos(k_{ref} \cdot r_{ref} - \omega t + \varphi_{ref}^s)$$

$$\mathbf{E}_{r,f}^s(r, t) = E_{r,f0}^s \cos(k_{r,f} \cdot r_{r,f} - \omega t + \varphi_{r,f}^s),$$

the resultant wave is $\mathbf{E}_{ref}^s(r, t) + \mathbf{E}_{r,f}^s(r, t)$ and the intensity can be written as [60]

$$I_f^s = \langle E_{ref}^s \rangle_T^2 + \langle E_{r,f}^s \rangle_T^2 + 2 \langle E_{ref}^s \cdot E_{r,f}^s \rangle_T$$

With the measurable quantities

$$\langle E_{ref}^s \rangle_T^2 = I_{ref}^s, \quad \langle E_{r,f}^s \rangle_T^2 = I_{r,f}^s \text{ and the interference term}$$

$$\langle E_{ref}^s E_{r,f}^s \rangle_T = \frac{1}{2} E_{ref0}^s E_{r,f0}^s \cos(k_{ref} \cdot r_{ref} + \varphi_{ref}^s - k_{r,f} \cdot r_{r,f} - \varphi_{r,f}^s) = \frac{1}{2} E_{ref0}^s E_{r,f0}^s \cos \delta_f^s$$

Since both waves have the same polarisation and traverse in the same direction, k_{ref} and k_r are the same and the distances r are fixed, and we can write

$$\delta_f^s = k(x_{ref} - x_{r,f}) + (\varphi_{ref}^s - \varphi_{r,f}^s) = \delta^0 + (\varphi_{ref}^s - \varphi_{r,f}^s)$$

$$I_f^s = I_{ref}^s + I_{r,f}^s + 2\sqrt{I_{ref}^s I_{r,f}^s} \cos \delta_f^s$$

$$\delta_f^s = \arccos\left(\frac{I_f^s - I_{ref}^s - I_{r,f}^s}{2\sqrt{I_{ref}^s I_{r,f}^s}}\right)$$

The same goes for the initial Mo signal

$$I_{Mo}^s = I_{ref}^s + I_{r,Mo}^s + 2\sqrt{I_{ref}^s I_{r,Mo}^s} \cos \delta_{Mo}^s$$

The change in phase is

$$d\delta^s = \delta_f^s - \delta_{Mo}^s = \delta^0 + (\varphi_{ref}^s - \varphi_{r,f}^s) - \delta^0 - (\varphi_{ref}^s - \varphi_{r,Mo}^s) = \varphi_{r,Mo}^s - \varphi_{r,f}^s = d\varphi_r^s$$

Since $d\Delta = d\varphi_r^s - d\varphi_r^p$ this results in $d\Delta = d\delta^s - d\delta^p$

We cannot determine Δ^0 directly. But there is a manner to determine a single value for Δ and \tilde{N}_3 , with only having the values for the reflectances (calculated from the intensities). By inserting these values in the equation

$$\tilde{N}_3 = \tilde{N}_1 \tan \theta_1 \sqrt{1 - \frac{4\rho \sin^2 \theta_1}{(\rho + 1)^2}}$$

and solving the function graphically with the help of the written Maple file ReflectanceMofinal.mw. This results in a value for Δ^0 and n_3 and k_3 . The roughness is taken directly into account in this value.

Alternatively, we can assume the tabled value for \tilde{N}_3 , which is about $n = 3.72$ and $\kappa = 3.55$ for 632 nm radiation²², from which the theoretical values of Ψ and Δ can be calculated directly to be $\Psi = 24.0160$ degrees and $\Delta^0 = 117.2326$ degrees.

In order to do so, the Fresnel coefficients for reflection in this Maple file, which contain θ_2 , are rewritten.

Rewriting the Fresnel coefficients for reflection

The reflection coefficients are given by:

$$r_{12}^s = \frac{\tilde{N}_1 \cos \theta_1 - \tilde{N}_2 \cos \theta_2}{\tilde{N}_1 \cos \theta_1 + \tilde{N}_2 \cos \theta_2}$$

²² Handbook of Chemistry and Physics, page 12-141

$$r_{12}^p = \frac{\tilde{N}_2 \cos \theta_1 - \tilde{N}_1 \cos \theta_2}{\tilde{N}_2 \cos \theta_1 + \tilde{N}_1 \cos \theta_2}$$

In the formulas for the reflection coefficients $\cos \theta_2$ and $\cos \theta_3$ terms are present. However, these (complex) numbers are unknown. To calculate the reflectances and to fit Del/Psi trajectories, these angles must be converted to θ_1 with Snell's law and the result is

$$\cos \theta_2 = \frac{\tilde{N}_1}{\tilde{N}_2} \sqrt{\left(\frac{\tilde{N}_2}{\tilde{N}_1}\right)^2 - \sin^2 \theta_1} \text{ and } \cos \theta_3 = \frac{\tilde{N}_1}{\tilde{N}_3} \sqrt{\left(\frac{\tilde{N}_3}{\tilde{N}_1}\right)^2 - \sin^2 \theta_1}$$

Inserting these in the reflection coefficients results in:

$$r_{12}^s = \frac{\tilde{N}_1 \cos \theta_1 - \tilde{N}_2 \frac{\tilde{N}_1}{\tilde{N}_2} \sqrt{\left(\frac{\tilde{N}_2}{\tilde{N}_1}\right)^2 - \sin^2 \theta_1}}{\tilde{N}_1 \cos \theta_1 + \tilde{N}_2 \frac{\tilde{N}_1}{\tilde{N}_2} \sqrt{\left(\frac{\tilde{N}_2}{\tilde{N}_1}\right)^2 - \sin^2 \theta_1}} = \frac{\cos \theta_1 - \sqrt{\left(\frac{\tilde{N}_2}{\tilde{N}_1}\right)^2 - \sin^2 \theta_1}}{\cos \theta_1 + \sqrt{\left(\frac{\tilde{N}_2}{\tilde{N}_1}\right)^2 - \sin^2 \theta_1}}$$

$$r_{12}^p = \frac{\tilde{N}_2 \cos \theta_1 - \tilde{N}_1 \frac{\tilde{N}_1}{\tilde{N}_2} \sqrt{\left(\frac{\tilde{N}_2}{\tilde{N}_1}\right)^2 - \sin^2 \theta_1}}{\tilde{N}_2 \cos \theta_1 + \tilde{N}_1 \frac{\tilde{N}_1}{\tilde{N}_2} \sqrt{\left(\frac{\tilde{N}_2}{\tilde{N}_1}\right)^2 - \sin^2 \theta_1}} = \frac{\tilde{N}_2^2 \cos \theta_1 - \tilde{N}_1^2 \sqrt{\left(\frac{\tilde{N}_2}{\tilde{N}_1}\right)^2 - \sin^2 \theta_1}}{\tilde{N}_2^2 \cos \theta_1 + \tilde{N}_1^2 \sqrt{\left(\frac{\tilde{N}_2}{\tilde{N}_1}\right)^2 - \sin^2 \theta_1}}$$

and

$$r_{23}^s = \frac{\tilde{N}_2 \cos \theta_2 - \tilde{N}_3 \cos \theta_3}{\tilde{N}_2 \cos \theta_2 + \tilde{N}_3 \cos \theta_3} = \frac{\tilde{N}_2 \frac{\tilde{N}_1}{\tilde{N}_2} \sqrt{\left(\frac{\tilde{N}_2}{\tilde{N}_1}\right)^2 - \sin^2 \theta_1} - \tilde{N}_3 \frac{\tilde{N}_1}{\tilde{N}_3} \sqrt{\left(\frac{\tilde{N}_3}{\tilde{N}_1}\right)^2 - \sin^2 \theta_1}}{\tilde{N}_2 \frac{\tilde{N}_1}{\tilde{N}_2} \sqrt{\left(\frac{\tilde{N}_2}{\tilde{N}_1}\right)^2 - \sin^2 \theta_1} + \tilde{N}_3 \frac{\tilde{N}_1}{\tilde{N}_3} \sqrt{\left(\frac{\tilde{N}_3}{\tilde{N}_1}\right)^2 - \sin^2 \theta_1}} =$$

$$= \frac{\sqrt{\left(\frac{\tilde{N}_2}{\tilde{N}_1}\right)^2 - \sin^2 \theta_1} - \sqrt{\left(\frac{\tilde{N}_3}{\tilde{N}_1}\right)^2 - \sin^2 \theta_1}}{\sqrt{\left(\frac{\tilde{N}_2}{\tilde{N}_1}\right)^2 - \sin^2 \theta_1} + \sqrt{\left(\frac{\tilde{N}_3}{\tilde{N}_1}\right)^2 - \sin^2 \theta_1}}$$

$$\begin{aligned}
r_{23}^p &= \frac{\tilde{N}_3 \cos \theta_2 - \tilde{N}_2 \cos \theta_3}{\tilde{N}_3 \cos \theta_2 + \tilde{N}_2 \cos \theta_3} = \frac{\tilde{N}_3 \frac{\tilde{N}_1}{\tilde{N}_2} \sqrt{\left(\frac{\tilde{N}_2}{\tilde{N}_1}\right)^2 - \sin^2 \theta_1} - \tilde{N}_2 \frac{\tilde{N}_1}{\tilde{N}_3} \sqrt{\left(\frac{\tilde{N}_3}{\tilde{N}_1}\right)^2 - \sin^2 \theta_1}}{\tilde{N}_3 \frac{\tilde{N}_1}{\tilde{N}_2} \sqrt{\left(\frac{\tilde{N}_2}{\tilde{N}_1}\right)^2 - \sin^2 \theta_1} + \tilde{N}_2 \frac{\tilde{N}_1}{\tilde{N}_3} \sqrt{\left(\frac{\tilde{N}_3}{\tilde{N}_1}\right)^2 - \sin^2 \theta_1}} \cdot \frac{\tilde{N}_2 \tilde{N}_3}{\tilde{N}_2 \tilde{N}_3} = \\
&= \frac{\tilde{N}_1 \tilde{N}_3^2 \sqrt{\left(\frac{\tilde{N}_2}{\tilde{N}_1}\right)^2 - \sin^2 \theta_1} - \tilde{N}_1 \tilde{N}_2^2 \sqrt{\left(\frac{\tilde{N}_3}{\tilde{N}_1}\right)^2 - \sin^2 \theta_1}}{\tilde{N}_1 \tilde{N}_3^2 \sqrt{\left(\frac{\tilde{N}_2}{\tilde{N}_1}\right)^2 - \sin^2 \theta_1} + \tilde{N}_1 \tilde{N}_2^2 \sqrt{\left(\frac{\tilde{N}_3}{\tilde{N}_1}\right)^2 - \sin^2 \theta_1}}
\end{aligned}$$

These expressions can now be inserted into the equation for the total reflection coefficients and subsequently into the equations for the reflectance, with

$$\beta = 4\pi \left(\frac{d}{\lambda}\right) \tilde{N}_2 \cos \theta_2 = 4\pi \left(\frac{d}{\lambda}\right) \tilde{N}_2 \frac{\tilde{N}_1}{\tilde{N}_2} \sqrt{\left(\frac{\tilde{N}_2}{\tilde{N}_1}\right)^2 - \sin^2 \theta_1} = 4\pi \left(\frac{d}{\lambda}\right) \tilde{N}_1 \sqrt{\left(\frac{\tilde{N}_2}{\tilde{N}_1}\right)^2 - \sin^2 \theta_1}$$

Now the only unknown variable in the total reflection coefficients is \tilde{N}_2 , since \tilde{N}_3 has been determined before.

\tilde{N}_2 can be determined by filling in values for n_2 and κ_2 in the Maple file Reflectance-Psi-Deltatest.mw, and plot Delta/Psi trajectories. By changing these values, the best fit to the Delta/Psi trajectory obtained from the measured data, can be made.

Appendix 3: Overview of Mg photocathodes

	Group	Reference	Mg Cathode		
			Preparation technique	Size	
1	Brookhaven National Laboratory	[62]	Sheet disks soldered on Cu substratum	12,5 mm diameter, 5 mm thick	
2		[68]	Disk pressed on Cu plug		
3		[68]			
4		[67]	Disk pressed on Cu plug		6 mm diameter
5		[10]	Ion-sputtered on Cu substratum		20 μm thick
6		[69]	Disk press fitted on Cu back plate		2 cm diameter
7		[70],[71]	Friction welded disk		
8		[65]			
9	University of Tokyo	[72]	Friction welded disk from BNL		
10		[73]	Friction welded disk from BNL		
11	R&D SHI Tokyo	[64]	Bulk and crystal		
12		[76]	Hot Isostatic Pressing bulk Mg on Cu	12 mm diameter, 9 mm thick	
13	University California	[41]	Disk	2,54 cm diameter	
14	Italy	[78]	PLD Mg on Cu substratum	200 nm thick + 20 nm oxide layer	
15	Argonne National Laboratory	[82]	Mg deposited on Cu substratum		
16		[82]	Solid Mg		
17		[66]	Solid Mg rod	2,8 cm diameter	
18	Stanford Linear Accelerator Center	[75]	Friction welded disk		
19		[74]	Friction welded disk	2 cm diameter	
20	INFN Milan	[63]			
21	Stanford University	[77]	Evaporation on gold-quartz and fused silica substratum	0,5 cm^2	
22	CERN	[²³]			

²³ <http://ucq.home.cern.ch/ucq/Photocathodes.htm>

Mg Cathode		Lifetime	
<i>Preparation</i>	<i>Laser cleaning</i>		
1	1 μm diamond compound, washed, baked at 150 °C	2-5 mJ/cm^2 for 5-10 min	Months > 5000 h > 3 months > 3 years > months between laser cleaning
2	Diamond turned	-	
3			
4	Polished with 1 μm diamond paste	-	
5	Baked at 100 °C for 48 h, irradiated with UV lamp	300 μm spot; 90 min 300 $\mu\text{J}/\text{mm}^2$; 70 angle; 36000 shots/ mm^2	
6	Polished and baked at 200 °C for 2 weeks	Two steps; last scanning with 160 $\mu\text{J}/\text{mm}^2$ with 67 MV/m	
7	Polished, baked at 150 °C for 1 week	Increase intensity 0,4 diameter spot	
8		-	
9	Polished, baked at 150 °C for 1 week	-	
10			
11			
12	Polished, cleaned, baked	0,17 mJ/mm^2 , 0,6mm diameter; RF off; 7000 shots/ mm^2	3 days
13	Polished to 1 μm	Above-damage threshold	
14		9 J/cm^2 ; wavelength 308 nm; 30 ns pulses	
15			
16			
17	Polished with 3 μm diamond powder	-	
18		-	
19		800 $\mu\text{J}/\text{mm}^2$; 68 μm spot; RF off; no effect!	
20			
21	Baked at 90 °C for 15 h.	-	< 1% QE decrease after 24 h.
22			

	Damage threshold	Conditions		Laser system			
		Pressure (Torr)	RF Field (MV/m)	Type	Wavelength (nm)	Pulse energy	Pulse length
1	100 $\mu\text{J}/\text{mm}^2$ RF breakdown	$10^{-8} - 10^{-9}$	10	Nd:YAG	266	1,5 mJ	10 ps
2		$< 10^{-8}$		Nd:YAG	266		12 ps
3					632	10 μJ	100 - 300 fs
4		$5 \cdot 10^{-7}$	50-70	Nd:YAG	266	200 μJ	$\sim 10 - 15$ ps
5		$10^{-8} - 10^{-9}$		Nd:YAG	266	1 mJ	12 ps
6			120		266	100 μJ	
7		$10^{-9} - 10^{-10}$	100	Yb:glass		1 mJ	5 - 15 ps
8					632		300 fs
9		$< 5 \cdot 10^{-10}$		Ti:Sapphire	265	few 100 μJ	\sim ps
10				Nd:YLF	262		~ 10 ps
11				Ti:Sapphire	260		100 fs
12		$< 2,2 \cdot 10^{-8}$	57	Nd:YLF	262 and 349	0,2 and 0,5 mJ	10 ps
13		10^{-6}	DC 1,6	Nd:YAG	266		50 ps
14		$7 \cdot 10^{-9}$	1	Nd:YAG	266		30 ps
15			75		248	5 mJ	3 ps
16							
17		$8 \cdot 10^{-10}$			372	1 mJ	6 - 8 ps
18		$10^{-8} - 10^{-9}$	80-90				
19		$5 \cdot 10^{-10}$	95				2 ps
20			100				166 fs
21		$2 \cdot 10^{-10}$		-	320	170 μW	
22			5-10 and 100		266		

Laser system			Electron beam		
Repetition rate (Hz)	Spot size	Angle of incidence	QE	Charge (max)	At laser energy
1	0,05-6 mm ²	Normal	6,2E-04	330 pC	3,12 μJ
2	1 mm diameter		3,0E-04		
3	10 Hz or 80 MHz				
4	0,4 mm diameter (=0,5 mm ²)	Normal	5,0E-04	80 pC or 4 nC	20 μJ or 70 μJ
5			2,0E-03	250 nC/mm ²	
6		72	2,0E-03	< 1 nC	
7	0,4 mm diameter or 1-3 mm diameter			1 nC	2,5 or 30 μJ
8		70-75	3rd order nonlinear		
9	3 mm diameter		1,3E-04	4 nC	210 μJ
10	4 mm diameter			0,75 nC	
11		35			
12	10	68	1E-03 and 2,2E-05	< 2 nC	~ 10 μJ and 100 μJ
13	3 mm		Factor 65-220 increase		
14			1 order increase		
15				> 110 nC	> 10 mJ/cm ²
16			1,3E-04	> 40 nC	> 2 mJ
17	1 and 2 cm diameter	Normal			
18		Normal	2,5E-05	< 0,5 nC	
19	2 mm diameter	Normal	8,0E-05	15 pC	
20				15 pC	
21	2 - 4 mm diameter	Normal	2E-03, increased by monolayer O		
22			5,1E-05 and 2,7E-04		

Electron beam				
	<i>At intensity</i>	<i>Bunch length</i>	<i>Bunch energy</i>	<i>Emittance</i>
1	620 MW/cm ²	11 ps	45 MeV	2,5 mm-mrad (rms normalized)
2	< 20 MW/cm ²			
3	< 100 GW/cm ²			
4				
5				
6				
7				
8	100 GW/cm ²			
9		0,7 ps	22 MeV	40 and 80 πmm-mrad (vertical and horizontal)
10		20 ps		9 - 15 mm-mrad (vertical)
11	< 80 GW/cm ²		3 MeV	
12				
13				
14				
15	> 3 GW/cm ²			
16				
17				
18				
19		0,4 ps		1,1 μm (transverse)
20		sub-ps		
21				
22				

Overview of Cu cathodes at the same research groups

	Group	Reference	Cu Cathode	
			Preparation technique	Size
1	Brookhaven National Laboratory	[62]	Sheet disks soldered on Cu substratum	
2		[97]		
3		[80]		
4	University of Tokyo	[98]	Hot Isostatic Pressing	
5		[99]		
6		[81],[100]		
7	University California	[41]	Disk	2,54 cm diameter
8	Argonne National Laboratory	[82]		2 cm diameter
9	Stanford Linear Accelerator Center	[74]	Brazed disk	1 cm diameter
10	CERN	[²⁰]		

	Cu Cathode		Lifetime
	Preparation	Laser cleaning	
1	1 μm diamond compound, washed, baked at 150 °C	2-5 mJ/cm^2 for 5-10 min	
2			
3			
4		Above-damage threshold	> 3 years
5			
6			
7	Polished to 1 μm	Above-damage threshold	
8			
9	Polished with 0,25 μm diamond paste	-	
10			

	Damage threshold	Conditions		Laser system			
		Pressure (Torr)	RF Field (MV/m)	Type	Wavelength (nm)	Pulse energy	Pulse length
1	100 mJ/cm ²	10 ⁻⁸ – 10 ⁻⁹	10	Nd:YAG	266	1,5 mJ	10 ps
2			1000	Nd:YAG	632	8 - 30 μJ	300 fs - 100 ps
3			95		266		> ps
4			100	Nd:YLF	264	100 μJ	10 ps
5							
6		< 10 ⁻⁹	85	Ti:Sapphire	265	< 250 μJ	4 - 11 ps
7		10 ⁻⁶	DC 1,6	Nd:YAG	266		50 ps
8			75		248	5 mJ	3 ps
9		2·10 ⁻⁹	110				2 ps
10			5 – 10		266		

	Laser system			Electron beam		
	Repetition rate (Hz)	Spot size	Angle of incidence	QE	Charge (max)	At laser energy
1		0,05-6 mm ²	Normal	1,4E-04		
2						
3		0,3 – 1,1 mm diameter	Normal		10 pC	
4	10-50 Hz	3 mm	40	5,8E-05	1 nC	
5					350 pC	
6	10	3 mm	68	1,4E-04	7 nC	250 μJ
7		3 mm		1E-05, cleaning increased QE factor 2		
8				4,0E-05	30 nC	
9		2 mm diameter	Normal	3,0E-05	15 pC	
10				2,2E-06		

Electron beam			
<i>At intensity</i>	<i>Bunch length</i>	<i>Bunch energy</i>	<i>Emittance</i>
1			
2	1 - 100 ps	< 5 MeV	< 0,1 πmm-mrad
3	1 - 5 ps		~ 0,6 mm-mrad (rms)
4	10 ps	4,7 MeV	1 and 7-14 πmm-mrad (horizontal and vertical)
5	240 fs	16 MeV	6 πmm-mrad
6	7 - 30 ps	20 MeV	20-30 πmm-mrad
7			
8	27 ps		17 πmm-mrad (rms emittance)
9	0,4 ps		0,6 μm (transverse)
10			

Appendix 4: Inventory of risks and protocol of handling

Risicoinventarisatie Magnesium

- I Magnesium poeder (korrelgrootte < 0.1 mm) synthese kwaliteit
CAS-No: 7439-95-4
- II Risico's:
- Vormt zeer licht ontvlambaar gas in contact met water. Spontaan ontvlambaar in lucht.
 - Symptomen van irritatie in de ademhalingswegen na inademen van stof
 - Wonden helen slecht na contaminatie met de stof
 - Lichte irritaties aan ogen na oogcontact
 - Mogelijke maagdarmlachten en verlies van eetlust na inslikken
- III Aard van de verrichte werkzaamheden: Het proces verloopt via een half gesloten systeem (zuurkast) en er is sprake van stoffen die bij 20 °C verdampen, die stof vormen of die door de intacte huid kunnen worden opgenomen: De blootstellingskans is matig.
- IV Blootstelling indien geen beschermende maatregelen zijn getroffen:
- Makkelijke verspreiding mogelijk van poeder.
 - Inademing van stof indien stofvorming plaatsvindt
 - Inademing van gas nadat de stof in aanraking is geweest met water
 - Opname via de huid of mond
 - Gevaar bij vochtige en/of warme werkomgeving
- Gevaren tijdens werkproces:
- Openen van bus (in een zuurkast) kan leiden tot stofvorming en verspreiding van poeder.
 - Uitnemen van een geringe hoeveelheid poeder dat vervolgens in een kleine container wordt geplaatst en aangedrukt, kan leiden tot verspreiding van poeder en stofvorming.
 - Het plaatsen van de container in de vacuumkamer kan leiden tot verspreiding van poeder.
 - Openen van de vacuumkamer kan leiden tot verbranding van overig magnesium als de stof niet voldoende is afgekoeld of als de kamer niet gespoeld wordt met stikstof.
- V Een bus met 500 gram magnesiumpoeder wordt **droog** bewaard in een **gesloten** verpakking in een **geventileerde brandwerende** chemicaliënkast verwijderd van ontstekingsbronnen en hitte; bij +15 °C to +25 °C. Voor gebruik met opdampen worden enkele grammen gebruikt.
Student en begeleider zijn op de hoogte van de risico's.
- VI Bij niet/onvoldoende schoonmaken van de zuurkast bestaat er risico voor de gebruikers van de zuurkast, namelijk restanten van magnesiumpoeder die in

contact komen met water kunnen gassen veroorzaken. Het is dus noodzakelijk na gebruik van magnesiumpoeder de zuurkast schoon achter te laten!

VII Plan van aanpak:

- Tijd van handelen minimaliseren
- Beschermmiddelen (handschoenen, jas, bril) verkrijgen
- Afvalton verkrijgen
- Blusmiddel (droog zand, zeker geen water of schuim) bij de hand

Protocol voor het werken met magnesiumpoeder

Risico's m.b.t. ademhalingswegen, huid, ogen en maag-darmen. Zie de Material Safety Data Sheet.

De bus met magnesiumpoeder wordt ALTIJD bewaard in de brandwerende chemicaliënkast. Dus na gebruik wordt het daar ook onmiddellijk weer in teruggezet.

Het magnesiumpoeder wordt verwerkt in de zuurkast. Verdere benodigdheden zijn een lepeltje, stampertje, bak en schoonmaakpapier. Afval wordt droog opgenomen en in een aparte afvalton bewaard en ter afvalverwerking aangeboden. Dit zijn minimale hoeveelheden.

Werkprocedure:

1. Veiligheidsbril opzetten en handschoenen en laboratoriumjas aantrekken.
2. Zuurkast volledig droog maken.
3. Bak met daarin papier als ondergrond, de container, lepeltje en stamper in zuurkast zetten.
4. Magnesiumpoeder uit chemicaliënkast halen en in bak plaatsen.
5. Container vullen met kleine hoeveelheid poeder (aantal gram) met behulp van het lepeltje, en aandrukken met stamper. Herhalen tot container vol is.
6. Bus dichtdraaien en in chemicaliënkast plaatsen.
7. Container dicht en plaatsen in verhittingsspiraal en afscherming.
8. Container in plastic zak inpakken.
9. Bak, lepel en stamper droog afnemen met papier. Papier wordt vervolgens in de afvalton weggegooid.
10. Container verplaatsen naar opstelling.
11. Container plaatsen in opstelling.
12. Handschoenen poeder afnemen, wassen, uitdoen en in afvalbak gooien. Laboratoriumjas uitdoen en bril afdoen.

Appendix 5: Recommendations

Recommendations for further research are:

- Improve the interfering signals from the diagnostic setup by reducing vibrations in the system. Alternatively, find a method to extract the correct value out of the present signal.
- Make a program in LabVIEW and/or Matlab to plot the Delta/Psi trajectories real time during deposition.
- Test operational performances of Cs-Te photocathodes made by different preparation conditions to investigate the robustness.
- Install a microbalance in the current preparation chamber for easy monitoring the deposition rate and have more control during deposition.
- Improve temperature monitoring of evaporation sources. Try to find a correlation for the inconsistent pressure and the role of contaminants after opening the vacuum chamber. After several times of heating the sources, the background pressure drops.
- Perform feasibility study on XPS data for Cs-Te photocathodes.

- Measure the deposition rate of Mg as a function of temperature.
- Investigate the non-linear response of Mg at high laser intensities, and determine the maximum extractable charge. Also as a function of pulse duration, especially for fs pulses.
- Study the relation between the layer thickness of Mg and the non-linear response.
- Measure the change in kinetic energy distribution of the extracted electrons to discriminate between the linear and non-linear response regime.
- Investigate the production of high charge electron bunches from Mg with high intensity IR laser pulses.
- Investigate the production of high charge electron bunches from Mg by initially heating the Mg photocathode with IR laser pulses before illuminating with UV fs laser pulses and the influence on QE and response time.
- Investigate the influence of oxygen adsorption on QE before and after laser cleaning.